TÉCNICO LISBOA

Dynamic analysis and design of impact attenuator structures for a Formula Student prototype

André Miguel Almeida Santos

Thesis to obtain the Master of Science Degree in

Mechanical Engineering

Supervisors: Prof. Aurélio Lima Araújo
Prof. José Firmino Aguilar Madeira

Examination Committee

Chairperson: Prof. Luís Alberto Gonçalves de Sousa
Supervisor: Prof. Aurélio Lima Araújo
Member of the Committee: Prof. João Orlando Marques Gameiro Folgado

June 2017

Dedicated to my family, for the relentless support over these 24 years.

Acknowledgments

I would like to give a special thank you to all those without whom this work would not have been possible:

First of all, to my family, for all the support and patience they've shown me through this long journey.

To Laura, for all the love, unceasing strength and permanent encouragement.

To a dear friend, Pedro Costa, for the absolutely monumental criticism and pressure to pursue nothing but the very best.

To Vitor Santos, Gonçalo Pereira, Daniel Pinho, Rui Miranda, João Sarrico and Tiago Rocha for the immense help with the crash site, the tests and, most importantly, the friendship shown.

To the old, the current and the next Chassis' team: Miguel Duarte, Bogdan Sandu, João Dias, Miguel Fechado, Nuno Leitão, Francisco Agostinho, Pedro Mendonça, Miguel Lino and Stefan Sochirca for the interest, enthusiasm and huge help during manufacturing and testing.

To Cláudio Duarte and Miguel Machado for the review of this work and long-lasting friendship.

To Luís Abreu, João Paulo Monteiro, Beatriz Lopes and João Antunes for the effortless integration of this work with the team's schedule and help with the home-made autoclave.

To professor Aurélio Araújo, professor José Aguilar, professor Hernâni Lopes, professor Virginia Infante and professor Pedro Amaral for the extensive technical support and permanent availability shown.

To Pedro Teixeira and João Vicente from the LTO for the precious help with manufacturing and testing.

Finally, but not least important, to the IEFP of Évora for allowing the use of their facilities.

Resumo

Este trabalho começa por retratar o estado actual da utilização de compósitos em aplicações de absorção de energia. É realizada uma breve explicação do processo numérico adequado ao caso em estudo, o critério de falha usado, é definida uma optimização multi-objectivo e o respectivo algoritmo, são exploradas as regras impostas pela competição de Formula Student, o filtro permitido e o procedimento experimental seguido.

A solução actual utilizada pela equipa é analisada e um modelo numérico desenvolvido. São realizados testes preliminares com tubos em alumínio e fibra de carbono, onde o processo de absorção de energia é analisado e um importante parâmetro (Crush Stress) ajustado. Foi desenvolvido um conjunto de testes de compressão quasi-estáticos, que possibilitem a determinação do Crush Stress, para diferentes empilhamentos.

São exploradas várias soluções através de novos modelos numéricos e processos de optimização, que só são possíveis depois da implementação de varias estratégias que visam diminuir o tempo de computação. As diferentes opções obtidas são ponderadas e, depois de seleccionadas, manufacturadas e testadas. Os resultados experimentais são apresentados e explicados, sendo apresentada uma solução final que cumpre com os requisitos.

Por fim, são retiradas conclusões e é proposto trabalho futuro de maneira a continuar o que foi desenvolvido neste trabalho.

Palavras-chave: Compósitos, Análise Explícita, Formula Student

Abstract

This works starts by portraying the state of the art of composites crashworthiness. A brief explanation regarding the most suitable numerical analysis, the used failure criteria, the multi-objective optimization definition and the respective algorithm, the rules imposed by the Formula Student competition, the low-pass filter used and the general experimental procedure is presented.

The current energy-absorbing structure solution is analysed and a numerical model is developed. Preliminary tests with aluminium and carbon fibre tubes follow, where the energy absorbing process is better understood and an important numerical parameter (Crush Stress) is fine-tuned. A set of quasi-static tests that are able to predict the Crush Stress of different lay-ups is developed and used subsequently.

Several solutions are explored through a series of developed numerical models and optimization processes, which are only possible after several time-reducing techniques and algorithms are applied. The different obtained options are later weighted, selected, manufactured and tested after which the experimental results are presented and explained. A final lighter solution is presented, manufactured and successfully tested.

At last, several conclusions are made and future work is proposed in order to achieve an even better solution.

Keywords: Composites, Crashworthiness, Explicit analysis, Formula Student

Contents

List of Tables

List of Figures

Nomenclature

Greek symbols

μ	Friction coefficient.
ν	Poisson coefficient.
ω	Angular frequency.
ω_c	Cut-off frequency.
ρ	Density.
σ	Normal stress.
τ	Shear stress.

Roman symbols

c	Speed of sound.
E	Young's modulus.
n	Order of Butterworth filter.
G	Transfer function gain.
G_0	Transfer function DC gain.

Subscripts

i, j, k	Computational indexes.
u	Ultimate.
uc	Ultimate compression.
ut	Ultimate tensile.
x, y, z	Cartesian components.
y	Yield.

Glossary

AIP Anti-Intrusion Plate.

CAD Computer Aided Design.

CFRP Carbon Fibre Reinforced Polymer.

CG Centre of Gravity.

DMS Direct MultiSearch.

FBH Front BulkHead.

fps Frames per second.

FSAE Formula Society of Automotive Engineers.

FST05e, FST06e, FST07e The previous, the current and the next car of the Formula Student team from the University of Lisbon - Projecto FST Novabase.

IA Impact Attenuator.

IAA Impact Attenuator Assembly.

MOO Multi-Objective Optimization.

PWR Permutations with repetitions.

SEA Specific Energy Absorption.

Chapter 1

Introduction

1.1 Motivation

During the last few decades, there has been an overall increase in the use of composite materials in several industries, which is mainly due to the decrease of material and manufacturing costs while allowing for lighter, yet more complex, designs. In the automotive industry, safety is a major concern which, along with several commodities, has increased the weight of cars and, as a consequence, the fuel consumption has also increased, which goes against an important goal (fuel efficiency) for costumers and companies alike. Replacing aluminium or steel Impact Attenuators (IA) with composites can reduce the weight while maintaining, or even increasing, the occupants safety, due to higher Specific Energy Absorption (SEA), Jones and Wierzbicki [1], a.G Mamalis et al. [2]. However, the design of composite impact attenuators may be very complex due to the intricate crush mechanisms and lack of accurate and computationally cheap, numerical or analytical models.

In the Formula Student competition, students are challenged to design, build and test a race car according to a specific set of rules by Formula Society of Automotive Engineers (FSAE). Formula Student has become a perfect testing ground for new concepts and ideas allowing the students to assess real-world problems in an academic environment.

Aligning the ever-lasting need of reducing the weight of a race car with the automotive industry goal of achieving lighter impact attenuator solutions, an opportunity to better understand this kind of energy-absorbing systems emerged.

1.2 Objectives

This thesis aims at assessing the performance of the current Impact Attenuator Assembly (IAA), used by the Formula Student team from the University of Lisbon - Projecto FST Novabase, by analysing the experimental data retrieved during the mandatory tests.

Furthermore, an analysis regarding the weight-saving potential of each part will be made and different, lighter, solutions will be proposed, thoroughly analysed, manufactured and tested when possible.

Mechanical tests regarding material characterization will also be performed and essential time-saving algorithms will be employed allowing several optimization problems to be defined.

1.3 Thesis Outline

The present work is divided into eight chapters. The first chapter presents the motivation of the author and its objectives. The second chapter regards the preliminary research on the topic, presenting what has been accomplished so far and the difficulties encountered by different authors.

The current Impact Attenuator Assembly (IAA) solution is presented and analysed in the third chapter. The aerodynamic related rules are also explained in this chapter and the current solution is proved to work on the new car.

On chapter four some preliminary simulations and testing regarding the design of a new crashbox are made. Aluminium and Carbon Fibre Reinforce Polymer (CFRP) tubes are simulated and tested.

Chapter five starts by experimentally determining the crush stress, an important parameter in CZone [3], and continues by analysing a structural nose solution and different crashbox configurations. Optimization problems are defined and the results discussed.

The sixth chapter presents the experimental results of the tested solutions.

The seventh chapter proposes a change to the Anti-Intrusion Plate (AIP) material. After a successful numerical analysis this solution is manufactured and tested.

The eight, and final, chapter provides an achievements summary and proposes future work to further enhance the solutions proposed.

Chapter 2

Background

2.1 Composites crashworthiness

While the steel and aluminium crashworthiness have been extensively studied in the past, such as Reid [4], Yoshida et al. [5] or Mohr and Wierzbicki [6], only recently have composites received similar attention.

In the past few years there have been different approaches to simulate the crush behaviour of composite materials such as Bogomolov et al. [7], which compared two commercially available finite-element softwares - Abaqus [8] CZone and LS-DYNA [9] - using different failure criteria, to model experimental setups of composite tubes. Deleo and Feraboli [10] studied the crashworthiness of carbon-fibre using different geometries and evaluated LS-DYNA [9]. Hesse et al. [11] presented a method to reduce design complexity, and thus time, of automotive composite parts subjected to crash loads. Furthermore, Ramos and Melo [12] compared Abaqus [8] CZone and Hypercrash [13] in the modelling of both a corrugated coupon and two lateral energy absorber tubes.

In the Formula Student competition, students are challenged to design, build and test a race car according to a specific set of rules by Formula Society of Automotive Engineers (FSAE), FSAE [14]. Regarding the mandatory frontal impact attenuator there have been many different approaches. Obradovic et al. [15] successfully simulated and tested carbon fibre tubes and a composite impact attenuator for the University of Torino's Formula Student team. The designed IA was a truncated pyramidal structure with an almost rectangular section and was able to comply with the FSAE rules through a quasi-static test. Boria and Belingardi [16] also analysed the crush behaviour of carbon fibre tubes with a similar aim to the present work, in order to establish a foundation of a design methodology for more complex geometries. Hussein et al. [17] studied the crush behaviour of empty and honeycomb-filled squared carbon fibre tubes, concluding that the latter absorb more energy but lose weight efficiency, meaning a lower Specific Energy Absorption (SEA) was attained. Similar but more complex analysis have been performed in Formula 1 cars, where Heimbs and Strobl [18] performed a crash analysis on the front impact structure using LS-DYNA [9]. Many teams still decide on an aluminium impact attenuator, Kumar et al. [19] presents a solution with a cone shaped aluminium crashbox, while Munusamy and Barton [20] studies the behaviour of aluminium tubes with similar purpose. Browne [21] presented a series of

experimental tests and analytical calculations in order to design a structural nose capable of absorbing the required energy.

Lukaszewicz [22] also analysed the benefits of composite materials in crash applications. Ko et al. [23] applied a sandwich composite to the low-floor of a bus and due to weight-limiting regulations and concluded that a similar level of safety for the driver and the passengers could be achieved.

Projecto FST Novabase, the Formula Student team from the University of Lisbon, currently uses an aluminium honeycomb crash box to absorb the required energy in case of a frontal impact.

2.2 Implicit vs Explicit analysis

Non-linear dynamic problems may be solved either with an implicit or an explicit solver. The two are fundamentally different approaches and may present very different outcomes.

In an implicit analysis, the propagation of dynamic effects is controlled by the structure's inertia, equivalent to having an infinite speed of sound. The user defines a time-step which is incremented every iteration. The equilibrium is enforced by using a Newton-Raphson algorithm, Verbeke and Cools [24], (or similar) until an user-defined tolerance is reached. The main drawback is that, for every iteration, the stiffness matrix must be updated and inverted, which can be very computationally demanding and may require considerable amounts of memory. However, the time-step used in an implicit analysis is usually much higher than used in an explicit analysis. The implicit analysis is suitable to solve relatively long duration or cyclic events with small deformations.

In an explicit analysis, a central-difference method is used. To ensure stability, the time-step is computed as the minimum time required to track the information (in this case stress) wave travelling through the material at the speed of sound, meaning that the time-step must be lower than the length of the smaller element divided by the speed of sound (equation (2.1)) in the material. Thus, the smaller the mesh element size the smaller the time-step which means that for the same run-time the computational effort increases exponentially with the mesh refinement due not only to the higher number of degrees of freedom, but also to the mandatory smaller time-step. In an explicit analysis, the mass matrix is inverted, as opposed to the stiffness matrix in an implicit analysis, which is considerably faster. Explicit analysis is suitable to solve high deformation, short duration, events.

$$c = \sqrt{\frac{E}{\rho}} \tag{2.1}$$

The crash analysis presented on this thesis involves very high deformations and non-linearities (such as material stiffness degradation) that take place in about 50 ms. Such conditions require an explicit analysis.

2.3 Failure Criteria

An accurate failure criteria is essential to correctly design any mechanical component. In applications where isotropic and ductile materials are used, it is common to use an yield criteria such as Von Misses (critical distortional energy - equation (2.2)).

$$\frac{1}{2}[(\sigma_{11}-\sigma_{22})^2+(\sigma_{22}-\sigma_{33})^2+(\sigma_{33}-\sigma_{11})^2+6(\sigma_{23}^2+\sigma_{31}^2+\sigma_{12}^2)]=\sigma_y^2 \tag{2.2}$$

However, by definition, this criteria cannot predict failure in composite materials. This criteria was further developed by Hill and later by Tsai-Hill, de Moura et al. [25]. The Tsai-Hill failure criteria is based on a series of experimental uniaxial tests and predicts composite layer failure when equation (2.3) is equal to, or greater than, one.

$$\frac{\sigma_1^2}{\sigma_{u1}^2}-\frac{\sigma_1\sigma_2}{\sigma_{u1}^2}+\frac{\sigma_2^2}{\sigma_{u2}^2}+\frac{\tau_{12}^2}{\tau_{u12}^2}=1 \tag{2.3}$$

This criteria has been widely used, such as Jiang and Zhang [26] and Suhairil and Husain [27] for instance, however it presents inconsistencies with experimental results. Hoffman [28] proposed a different criteria with linear terms to account for the possibility of failure under hydrostatic stress, equation (2.4), where F_i and F_{ij} are constant parameters related to the mechanical properties of the composite material.

$$F_i\sigma_i+F_{ij}\sigma_i\sigma_j=1, \quad i,j=1,...,6 \tag{2.4}$$

Considering a plane stress state the Tsai and Wu [29] (Tsai-Wu) criteria is obtained, equation (2.5).

$$F_{11}\sigma_1^2+F_{22}\sigma_2^2+F_{66}\tau_{12}^2+F_1\sigma_1+F_2\sigma_2+2F_{12}\sigma_1\sigma_2=1 \tag{2.5}$$

Considering uniaxial tests it is possible to achieve all the missing parameters (equations (2.6)), except for F_{12} which requires biaxial tests. Due to the complexity and data dispersion of such a test, F_{12} is typically assumed to be $-1/2$ for carbon fibre composites, de Moura et al. [25].

$$\begin{aligned} F_{11}&=\tfrac{1}{\sigma_{ut1}\sigma_{uc1}}; \qquad F_{22}=\tfrac{1}{\sigma_{ut2}\sigma_{uc2}}; \quad F_{66}=\tfrac{1}{\tau_{u12}^2} \\ F_1&=\tfrac{1}{\sigma_{ut1}}-\tfrac{1}{\sigma_{uc1}}; \quad F_2=\tfrac{1}{\sigma_{ut2}}-\tfrac{1}{\sigma_{uc2}}; \end{aligned} \tag{2.6}$$

The Tsai-Wu criteria is an interactive criteria, meaning it accounts for the effect of all the stress components. However, it also means it can't identify the failure mechanism. But it was, nonetheless, the criteria chosen in the following chapters due to the good compromise between complexity, accuracy and the mechanical properties available.

2.4 Optimization

In a Multi-Objective Optimization (MOO) problem, two or more objective functions are simultaneously optimized. The MOO problem can be mathematically formulated as (2.7), see Miettinem [30].

$$\begin{aligned} min \quad & F(\boldsymbol{x}) \equiv (f_1(\boldsymbol{x}), f_2(\boldsymbol{x}), ..., f_m(\boldsymbol{x})) \\ s.t. \quad & \boldsymbol{x} \in \Omega \end{aligned} \tag{2.7}$$

Where m ($\geqslant 2$) is the number of objective functions $f_j : \Omega \subseteq \mathbb{R}^n \rightarrow \mathbb{R} \cup \{+\infty\}, j = 1, ...m$, and Ω ($\emptyset \neq \Omega \subseteq \mathbb{R}^n$). Note that maximizing f_j is equivalent to minimizing $-f_j$. The feasible region, Ω, represents the set of points that satisfy the problem constraints. Constraints can either be defined by mathematical expressions or be regarded as an oracle (in the case of black box optimization).

MOO constrained problems, the situation in which two (or even more) conflicting performances are to be optimized, are becoming more and more frequent and, more particularly, black-box type, are almost ubiquitous in real-world applications and very well studied in the literature, such as Franco Correia et al. [31], Madeira et al. [32] or Franco Correia et al. [33].

MOO example

Consider an optimization problem with two objective functions ($m = 2$) and a feasible region $\Omega \subseteq \mathbb{R}^3$ ($n = 3$) (2.8).

$$\begin{aligned} min \quad & F(\boldsymbol{x}) \quad \equiv (f_1(\boldsymbol{x}), f_2(\boldsymbol{x})) \\ s.t. \quad & 0 \leq x_1 \leq 15 \\ & 0 \leq x_2 \leq 16 \\ & 0 \leq x_3 \leq 12 \end{aligned} \tag{2.8}$$

In figure 2.1 the variables space and the objective function space for such a problem are represented, note that every point in the variable space has a corresponding image in the objective function space.

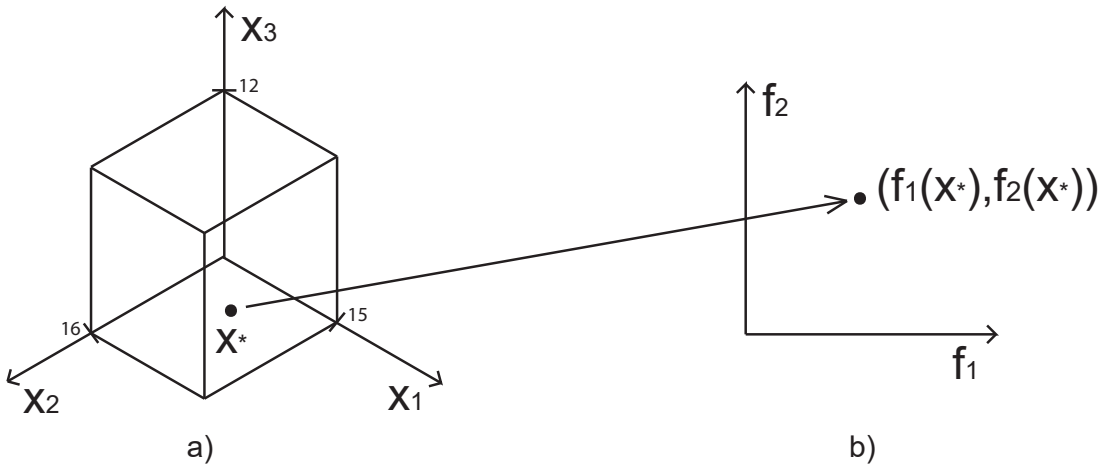

Figure 2.1: Variable space (a) and objective function space (b).

In the presence of several objective functions, the set of design variables, which minimize one function, are not necessarily the same, which minimize another function. In such situations, the classical optimality definition for single-objective problems must be replaced by the well-known Pareto optimality definition.

Given two points $\boldsymbol{x}, \boldsymbol{y} \in \Omega$ then, $\boldsymbol{x}$ dominates $\boldsymbol{y}$ ($\boldsymbol{x} \prec \boldsymbol{y}$) if and only if $f_j(\boldsymbol{x}) \leqslant f_j(\boldsymbol{y})$ for all $j \in \{1, ..., m\}$ and $f_i(\boldsymbol{x}) < f_i(\boldsymbol{y})$ for at least one index $i \in \{1, ..., m\}$. $\boldsymbol{x} \not\prec \boldsymbol{y}$ means that $\boldsymbol{x}$ does not dominate $\boldsymbol{y}$.

A set of points in Ω is nondominated when no point in the set is dominated by another one in the set. Thus, the Pareto optimizers are the nondominated points which are used to characterize optimality in MOO. Mathematically, a point $\boldsymbol{x} \in \Omega$ is a global Pareto optimizer of F in Ω if there is no $\boldsymbol{y} \in \Omega$ such that $\boldsymbol{y} \prec \boldsymbol{x}$.

Example of Pareto dominance

Considering the points in figure 2.2:

- $\mathbf{1} \prec \mathbf{4}$ because $f_1(\mathbf{1}) < f_1(\mathbf{4})$ and $f_2(\mathbf{1}) < f_2(\mathbf{4})$
- $\mathbf{2} \prec \mathbf{3}$ because $f_2(\mathbf{2}) < f_2(\mathbf{3})$ and $f_1(\mathbf{2}) \leqslant f_1(\mathbf{3})$
- $\{\mathbf{1}, \mathbf{2}\}$ are nondominated because $\mathbf{1} \not\prec \mathbf{2}$ and $\mathbf{2} \not\prec \mathbf{1}$

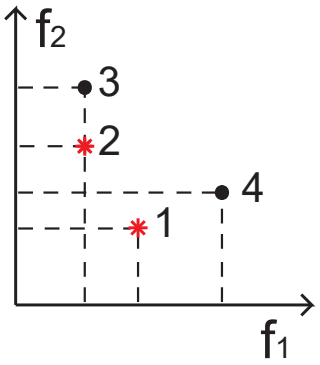

Objective Function Space

Figure 2.2: The nondominated solutions are represented by the red stars.

2.4.1 Direct Multisearch method

The Direct Multisearch (DMS), Custódio et al. [34], is the optimization algorithm used in the following chapters and is a derivative free optimization method, which does not aggregate or define priorities for the several objectives involved. Each iteration of DMS is composed of a search step and a poll step. The algorithm maintains a list of the feasible, nondominated points, which represent the most recent approximation to the Pareto front and from which poll centers will be chosen. New feasible evaluated points are added to this list every iteration and the dominated ones are removed. The iteration is considered to be successful if the list changes, meaning that a new feasible nondominated point was found. Otherwise, the iteration is considered unsuccessful.

The algorithm performs a local search around a poll center by testing directions belonging to a positive basis, or a positive spanning set, scaled by a step size parameter. The new feasible nondominated points are added to the iterate list and the dominated points are removed.

If an iteration is considered to be unsuccessful then the corresponding step size parameter is decreased. In case of a successful iteration, the step size is kept constant, or even increased.

In this method, the constraints are handled using an extreme barrier function, as in equation (2.9).

$$F_\Omega(a) = \begin{cases} F(a) & \text{if } a \in \Omega, \\ (+\infty, ..., +\infty) & \text{otherwise} \end{cases} \tag{2.9}$$

This means that if a point is infeasible then the objective functions $f_i, i = 1, ..., m$ are set to $+\infty$.

The algorithm used presented several options regarding the initialization such as line sampling, random sampling, Latin hypercube sampling, among others. It was verified that, for the kind of problems solved in this work, a line sampling was the most efficient sampling method.

Details are omitted in the present work and the reader is reffered to Custódio et al. [34] for a more complete description of this method.

2.5 Aerodynamic Devices

The rule T2.20.3 of the FSAE rules (FSAE [35]) is transcripted below:

Vehicles with aerodynamic devices and/or environment perception sensors in front of the IA must not exceed the peak deceleration of T2.20.1 for the combination of their IAA and the non-crushable object(s). Any of the following three methods may be used to prove the design does not exceed 120 kN:

- *Physical testing of the IAA including any attached non-crushable object(s) in front of the AIP*
- *Combining the peak force from the physical testing of the IAA with the failure load for the mounting of the non-crushable object(s), calculated from the fastener shear and/or link buckling.*
- *Combining the "standard" IA peak load of 95 kN with the failure load for the mounting of the non-crushable object(s), calculated from fastener shear and/or link buckling.*

It clearly states that teams must take into account the presence of aerodynamic devices forward of the impact attenuator (in case they exist). Three different methods may be used to combine the loads from the crushing of the impact attenuator with the loads required to cause failure of the aerodynamic devices. The combination of these loads must remain lower than 120 KN.

The first method is the most accurate, as the aerodynamic devices are directly crash-tested with the impact attenuator. However, this is not feasible for the team due to the high costs involved in manufacturing an entire front wing assembly.

The second method retrieves the maximum load from the experimental crash test of the impact attenuator and combines it with fastener shear and/or link buckling. The way teams achieve this value may be through analytic calculations, finite element analysis and/or physical testing.

The third method only applies to teams using the standard impact attenuator, which is not the case due to its excessive weight (700 grams).

With the three options stated and analysed it's trivial that the second method must be followed.

2.6 Butterworth Filter

When using accelerometers to capture such a short duration impact event (about 50 ms), and thus high sampling rates, it is expected to register accelerations related to both the rigid-body motion of the decelerating weight and to the high-frequency vibrations.

As this is a safety crash test, the former accelerations are the ones that may cause damage to the driver. The rule T2.20.4 of the FSAE rules covers this issue by allowing a low-pass Butterworth filter to be applied in case the 40 *g* limit is violated. The rule T2.20.4 is transcripted below:

Dynamic testing (sled, pendulum, drop tower, etc) of the IA may only be conducted at a dedicated test facility. This facility may be part of the university, but must be supervised by professional staff. Teams are not allowed to design their own dynamic test apparatus.

When using acceleration data from the dynamic test, the average deceleration must be calculated based on the raw unfiltered data.

If peaks above the 40 g limit are present in the data, a 100 Hz, 3^{rd} order, low pass Butterworth (-3 dB at 100 Hz) filter may be applied.

The Butterworth filter is commonly used in signal processing due to its ease of hardware implementation and the nominally flat response within its pass-band.

A low pass, n order, Butterworth filter is given by equation (2.10). Where $G(\omega)$ is the magnitude of the frequency response, G_0 the DC gain and ω_c the cut-off frequency. A third order filter has a descent slope of 60 dB/dec and will be used in several chapters of this work.

$$G^2(\omega) = \frac{G_0^2}{1 + \frac{j\omega}{j\omega_c}^{2n}} \tag{2.10}$$

2.7 Experimental Setup

The test setup was slightly changed throughout the development of this work. This section presents its main characteristics and later, at the beginning of every experimental section, a brief description regarding specific changes is presented.

As already stated in section 2.6, rule T2.20.4 of the FSAE rules allows several test methods to be used in order to determine if the team's IAA is rules compliant. The test facility available throughout this work is a drop tower (figure 2.3(a)), built by the team several years ago (before the official prohibition on self-designed test apparatus). The weight cart carries several steel beams, allowing the weight to be adjusted, and is connected to the green vertical beam by bearings which allow it to slide through with little friction. The cart is suspended by steel cables which connect it to a manual hoist. In order to safely separate the cart from the hoist a release mechanism was built (figure 2.3(b)), where an asymmetrical tube ensures the cart doesn't drop until the manual trigger system is activated. Until the experimental tests performed for this work, the barrier was composed of a 25 mm thick steel plate with several layers of Medium Density Fiberboard (MDF), cork and stone.

Throughout this work two independent systems were used, a set of three *Bruel & Kjaer 4371* piezoelectric accelerometers (Kjaer [36]), connected to three *Bruel & Kjaer 2635* charge amplifiers (Kjaer [36]) and sampled by a *National Instruments PXI* equipment (figure 2.4(a), Instruments [37]), and a *Photron SA4* high speed camera (figure 2.4(b)).

(a) Drop tower.

(b) Release mechanism detail.

Figure 2.3: Drop tower setup and release mechanism detail.

(a) Accelerometer data acquisition system.

(b) *Photron SA4* high speed camera.

Figure 2.4: Impact recording systems used.

2.7.1 Barrier Improvements

Tests from previous years showed that the barrier wasn't rigid enough and acted as a spring (figure 2.5), which compromised results.

It was clear that a better solution would have to be implemented before the tests for this work were carried out. Otherwise, the rigid barrier approximation implemented on the numerical model would be far from reality.

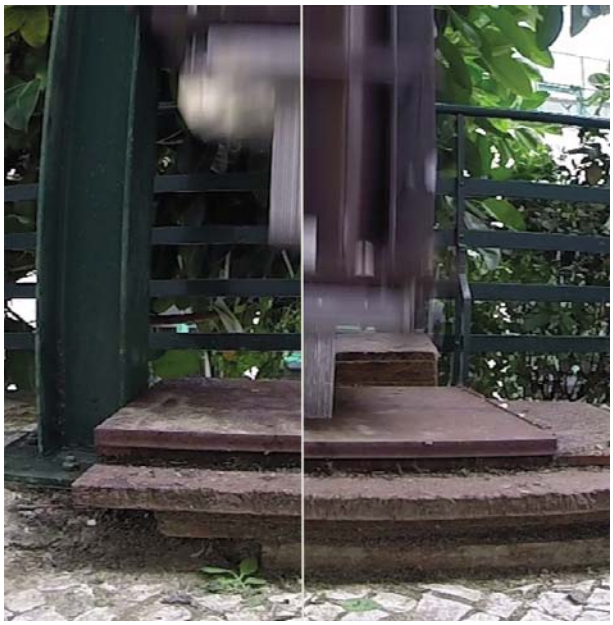

Figure 2.5: Barrier deformation observed during an impact.

Due to the high forces generated during an impact, up to several hundreds of kilonewtons, the barrier would need a high superficial strength and to be much stiffer. A reinforced concrete block of 1 m long, 0.8 m wide and 0.5 m deep (figure 2.6) with a bolted steel plate on top was built in place.

(a) Steel cage.

(b) Finished reinforced concrete block.

Figure 2.6: New barrier construction.

Later it was verified, with the high-speed camera, that the new barrier effectively eliminated the displacement to unperceivable values.

2.7.2 Release Mechanism Improvements

The release mechanism is a critical device used in the test to drop the weight cart. It was verified that the current solution used by the team wasn't reliable enough and didn't ensure the safety that a test like this requires, due to the excessive deformation of the trigger tube (already shown in figure 2.3(b)).

A new release system was designed and manufactured taking into consideration the required safety features. Even though the maximum dropped weight in this work is 300 kg, the hoist is not directly above

the weight cart causing the actual force applied on the release mechanism to be substantially higher. The maximum angle between the vertical direction and a line connecting the hoist to the weight cart was estimated to be $45°$, so the actual force supported by the release mechanism is the equivalent to 423 kg (plus possible peak forces during the weight ascension).

Due to the importance of this device, the assembly was designed to withstand a load of 1000 kg, with an added safety coefficient for the parts manufactured in-house (the bought steel shackles, cables and cotter pin already have the required load rating).

Using Solidworks [38], a Computer Aided Design (CAD) model was developed, as seen in figure 2.7.

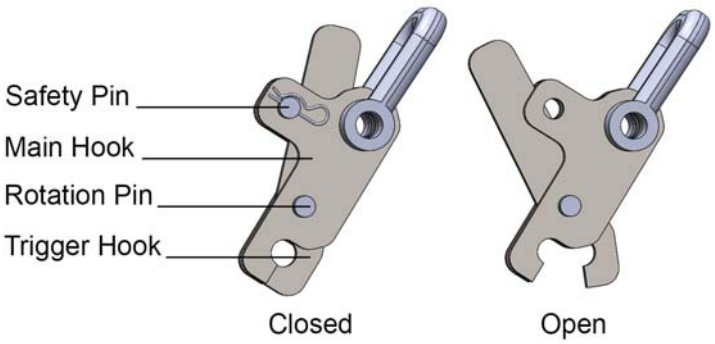

Figure 2.7: Release mechanism CAD model. Open and closed position.

Three main safety features are illustrated in figure 2.7:

- A cotter pin ensures the safety pin stays in place, thus keeping the claw-shaped mechanism closed.
- Due to the safety pin position, relatively to the ground, and friction between the pin and the main hook, it stays in place even when the cotter pin is removed. A longitudinal force is required to remove the safety pin.
- Even with the cotter pin and safety pin removed, the claw-shaped mechanism remains firmly closed. By design, the shackles aren't aligned with the rotation pin, meaning that a closing torque is generated when force is applied to the shackles. Only when sufficient force is applied to the lower claw does the mechanism open, releasing the weight cart.

Using the finite element analysis capabilities of Solidworks [38], a static analysis was performed on the claw-shaped mechanism. An high strength steel (EN S700MC) was used on all parts.

On the main hook, 22685 linear tetrahedral elements with a maximum aspect ratio of 4 were created, figure 2.9(a). A fixed boundary condition was imposed on the hole where the shackle connects and the translation degrees of freedom were locked on the rotation pin hole. A force of 3300 N (1000 kg divided by 3 parts) was applied on the frontal quarter of circle, where the weight cart shackle connects.

In figure 2.8(a), the Von Misses stress results for the main hook parts are presented. The maximum stress obtained was 430 MPa, which results in a yield safety coefficient of 1.65, and its location was, as expected, on the smallest cross-section directly above the load application point.

The displacement results are shown in figure 2.8(b), where the maximum displacement obtained was 0.072 mm, which is enough to keep the system closed even when the maximum projected load is

applied.

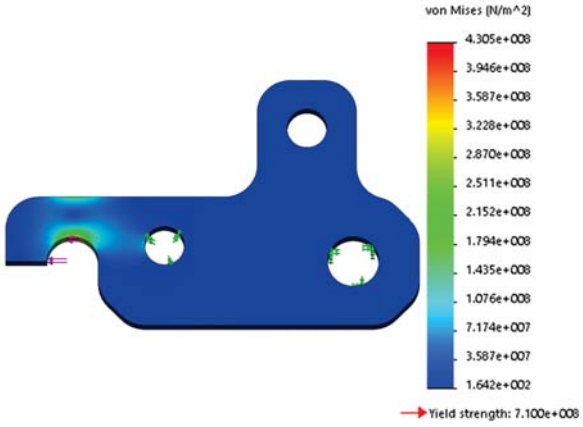

(a) Von Misses stress results of the main hook part.

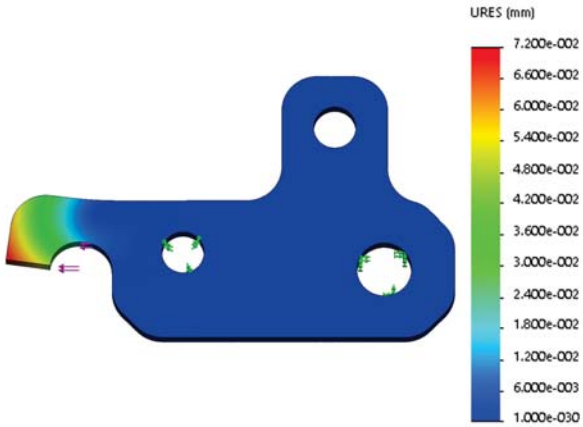

(b) Displacement results of the main hook part.

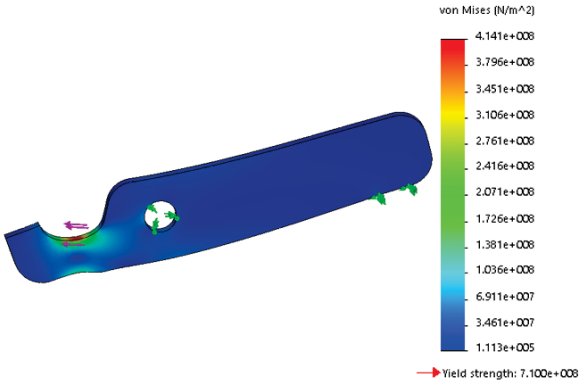

(c) Von Misses stress results of the trigger hook.

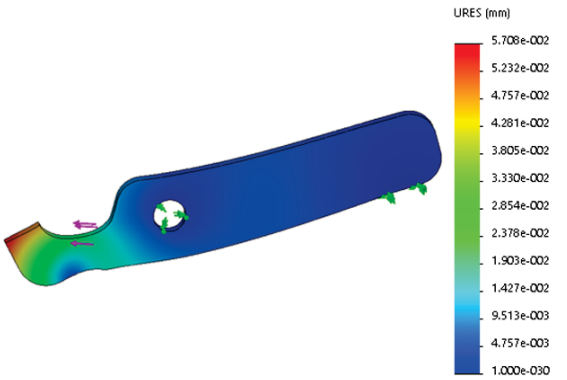

(d) Displacement results of the trigger hook.

Figure 2.8: Static analysis results (Plot scale: x200).

A similar approach was applied to the trigger hook part, where 19753 tetrahedral elements, with a maximum aspect ratio of 4, were generated, figure 2.9(b). The translation degrees of freedom were once again constrained on the hole of the rotation pin and a fixed boundary condition was applied on the lower side to simulate the contact with the shackle. A similar force of 3300 N was applied on the front section.

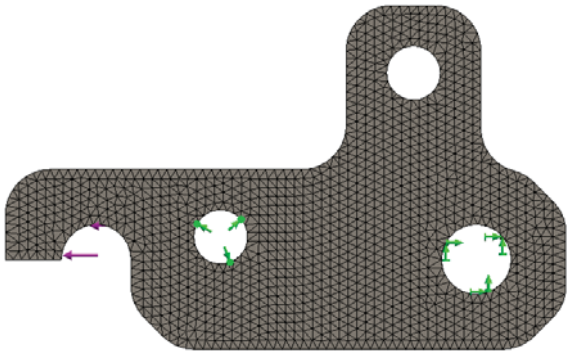

(a) Main hook.

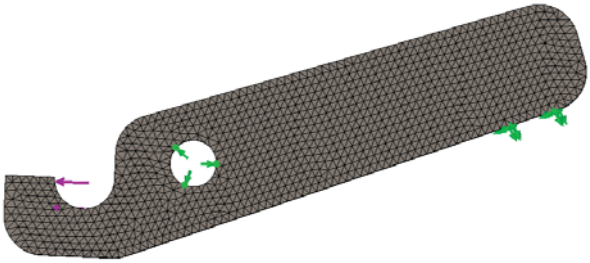

(b) Trigger hook.

Figure 2.9: Meshes and boundary conditions applied on both hooks.

The Von Misses stress results are shown in figure 2.8(c), where a maximum stress of 414 MPa was obtained, resulting in a yield safety coefficient of 1.71.

Regarding the maximum displacement, a value of 0.057 mm was obtained which was also considered to be enough to ensure the assembly stays closed when loaded.

The rotation pin was also verified using simple analytical calculations. The pin connects the three steel parts studied above, thus it is in double shear and it was assumed that it would need to withstand a 10000 N load.

Following the calculations performed in table 2.1 a safety coefficient of 12.55 is obtained.

Table 2.1: Rotation pin analytical calculations.

Rotation Pin Radius $[mm]$ (a)	Force Applied $[N]$ (b)	Area $(2\pi a^2)$ $[mm^2]$ (c)	Stress $(\frac{b}{c})$ $[Mpa]$ (d)	Shear Yield Stress $[MPa]$ (e)	Safety Coefficient $(\frac{e}{d})$
7.5	10000	353.42	28.29	355	12.55

The load case of the safety pin isn't as trivial as the rotation pit because, theoretically, it wouldn't need to support any loads, as the trigger hook part tends to close the opposite way. The only function of the safety pin is to ensure the weight cart doesn't fall even when the trigger rope, that connects to the trigger hook part, is accidentally pulled. Taking this into consideration a radical load case was imposed. The pin would need to withstand an average person's entire weight (75 kg) on the trigger rope without failing.

A schematic of the force balance is presented on figure 2.10, where the a and b distances are presented on table 2.2. By performing a torque balance around the rotation pin one gets (2.11) and thus obtains the reaction force on the safety pin according to release force imposed. Similarly to the rotation pin, the safety pin is also in double shear and simple analytical calculations were performed on table 2.2 achieving a safety coefficient of 11.52.

$$\sum M_{RotationPin} = 0 \Leftrightarrow F_{SafetyPin}a - F_{Release}b = 0 \Leftrightarrow F_{SafetyPin} = \frac{b}{a}F_{Release} \tag{2.11}$$

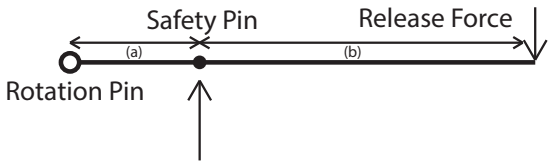

Figure 2.10: Force balance.

Safety Pin Radius $[mm]$ (c)		Mass considered $[kg]$ (d)	Safety Pin Force $(9.81d\frac{b}{a})$ $[N]$ (e)	Area $(2\pi c^2)$ $[mm^2]$ (f)
6.5		75	8175	132.73
(a) $[mm]$	(b) $[mm]$	Stress $(\frac{e}{f})$ $[MPa]$ (g)	Shear Strength $[MPa]$ (h)	Safety Coefficient $(\frac{h}{g})$
45	500	30.80	355	11.52

Table 2.2: Safety pin analytical calculations.

In figure 2.11(a), the final manufactured release mechanism is presented. An extension tube was welded to the trigger hook part to lower the force required to open the mechanism (already accounted for in the previous calculations). In figure 2.11(b) the device is shown in the actual position and ready to drop the weight cart. Progressively higher drop tests were first conducted to ensure the system safety and these were then repeated several times to guarantee reliability. No failure was observed nor did the release mechanism ever unleash the weight cart in unexpected circumstances throughout the course of this work proving that the developed concept works.

(a) Manufactured release mechanism.

(b) Release mechanism being use.

Figure 2.11: New release mechanism.

Chapter 3

Current Solution of the IAA

3.1 FST06e

In the previous car, the FST06e, the IAA was composed of an aluminium AIP, an aluminium honeycomb block as an IA and a non-structural carbon fibre nose (figure 3.1).

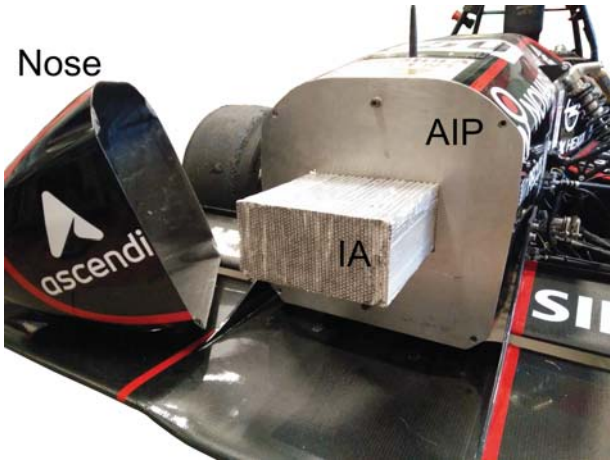

Figure 3.1: IAA of the previous car.

Even though the team has used this assembly since the FST05e, it was never actually thoroughly analysed, but was instead used as an out-of-shelf solution that complied with the regulations. The problem with blindingly trusting a solution like this is that the cars are never exactly the same and what complies for one might not comply for another. The first AIP and IA tested by the FST06e team was only attached to the Front BulkHead (FBH) by four bolts, similarly to the FST05e. However the AIP was larger, which caused it to deform more than allowed and wasn't approved, this error costed the team both time and resources. A numerical model capable of predicting the behaviour of such a system is of great importance. Besides, as a Formula Student team gets increasingly better, each component of the car must get higher levels of attention to ensure the best solutions are used.

The team provided the author of this work with the experimental data of the mandatory test from the previous year. The IAA was attached to the bottom of the steel weight (figure 3.2(a)) while an

accelerometer, glued to the structure, registered the impact (figure 3.2(b)). The 320 kg were then lifted and dropped from an height of 2.5 m.

(a) Experimental testing of the FST06e solution.

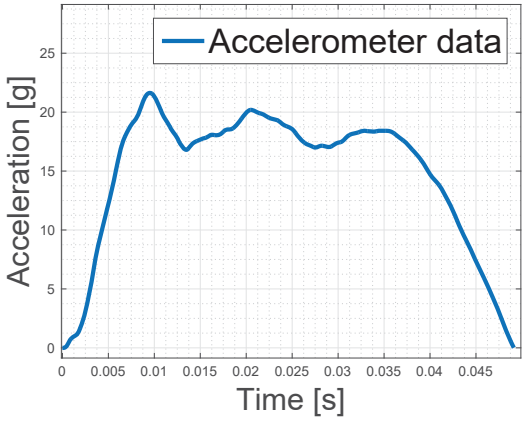

(b) Accelerometer data.

Figure 3.2: FST06e experimental setup and accelerometer data.

In order to predict if this solution would be acceptable for the next car, the FST07e, a numerical model was developed using Hypermesh [39] to model the IA assembly of the FST06e and later solved by Radioss [40] to check if a good correlation to the experimental test was attained. The geometry was thus imported into Hypermesh [39], where a mesh was defined for each component. Then the model was imported into Hypercrash [13] where material properties, boundary conditions and initial conditions were defined. At last the simulation was run using the explicit solver Radioss [40].

Figure 3.3 shows the mesh created in Hypermesh [39]. The barrier, the AIP and the FBH were meshed with shell elements. While the barrier was meshed with an element size of 19 mm, the AIP was meshed with an element size of 6 mm and the FBH with an element size of 10 mm. The IA was meshed with solid elements and an element size of 10 mm. A total of 4000 solid elements with an unitary aspect ratio were used. As for shell elements a total of 5489 were used with a maximum aspect ratio of 2.74.

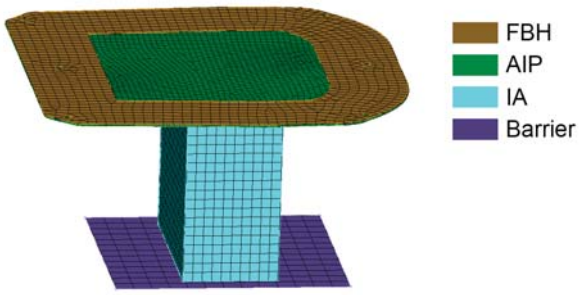

Figure 3.3: Model meshed in Hypermesh [39].

The material properties were based on a tutorial made available online by Altair (a software company responsible for developing computer-aided engineering products) where they use the same kind

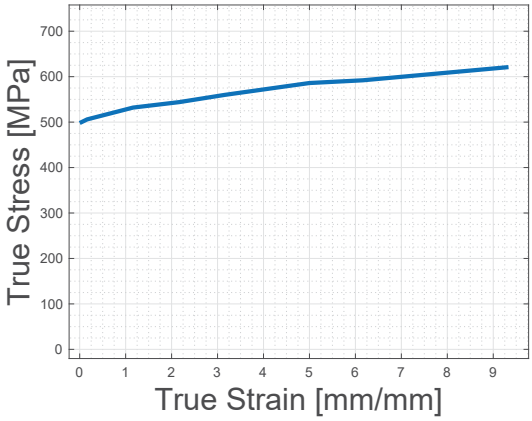

Figure 3.4: Aluminium true stress versus true strain curve.

ρ [kg/m^3]	E [GPa]	ν
2800	69.6	0.334

Table 3.1: Further mechanical properties used.

of aluminium honeycomb (Plascore internal reference PACL-XR1-5.7-3/16-P-5052) and aluminium AIP material (EN AW 7075) as the team.

The aluminium was defined using a piecewise linear material model with the true stress versus true strain curve of figure 3.4 and the material properties of table 3.1.

As for the IA an honeycomb material model was used (Material 28 in Hypercrash [13]). The stress versus strain curves used were supplied by Altair and are based on experimental testing. The stress versus strain curves presented in figures 3.5(a) and 3.5(b) were obtained through compression tests. Note that for very low strains, the stress curve rises steeply caused by the compaction of the honeycomb structure. Figures 3.5(c) and 3.5(d) refer to the shear strength on in-plane and out-plane directions. In a small range, around the origin, the honeycomb presents relatively high shear stress strength, which justifies its importance in sandwich laminates. However, outside that gap, the stress drops to almost zero.

Table 3.2: Honeycomb material properties used.

E_{11} [GPa]	E_{22} [GPa]	E_{33} [GPa]	G_{12} [GPa]	G_{23} [GPa]	G_{31} [GPa]	ρ [kg/m^3]
0.2256	0.002	0.002	0.2	0.2	0.2	91.3

Contact, with self-impact, conditions were imposed between the barrier and the IA, between the AIP and the FBH and between the IA and the AIP. A type 7 contact was specified for the first two and a type 2 contact for the third.

Both the FBH and the barrier were considered to be rigid bodies. The Barrier's motion was constrained in all directions, except for the vertical displacement, and an associated mass of 320 kg was associated with it. The FBH on the other hand had all its degrees of freedom constrained.

A mesh sensitivity analysis of the aluminium honeycomb was performed in order to understand its influence on the acceleration and displacement results. In figures 3.6(a) and 3.6(b), the results for three different mesh element sizes are presented and compared with the experimental data. The difference between the 10 mm mesh and 5 mm mesh is of 6.2% on the point of maximum deviation on the acceleration curves. The displacement differences between meshes are much smaller and have a

better correlation to the experimental data.

The friction coefficient between the FBH and the AIP and between the IA and the Barrier is unknown. However, in figures 3.7(a) and 3.7(b), a friction sensitivity analysis was performed in order to understand its importance. It was concluded that friction has a very small effect on the acceleration and displacement results and thus a coefficient of 0.3 was defined.

Considering a 10 mm mesh and a friction coefficient of 0.3, the numerical and experimental curves were compared. The experimental impact duration is 11% smaller than the numerical model prediction. The experimental data also presents an higher degree of variability, as opposed to the almost constant acceleration curve predicted by the numerical model. Except for the peak near the end of the impact, which may be explained by the honeycomb compaction. The maximum acceleration measured was 212m/s^2 and the mean acceleration was 146m/s^2, while the numerical model resulted in a maximum acceleration of 191m/s^2 and a mean acceleration of 142m/s^2. Thus, an error of 10%, regarding the maximum acceleration, and an error of 3%, regarding the mean acceleration, was obtained.

In figure 3.8 frame results from the numerical simulation are compared with the tested crashbox. A similar progressive aluminium honeycomb folding mechanism was achieved.

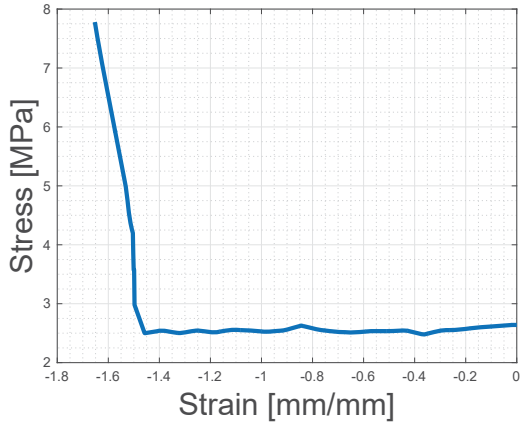

(a) Stress versus strain curve in the 11 direction.

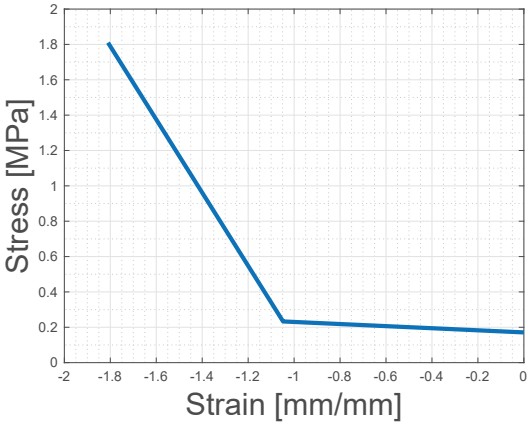

(b) Stress versus strain curve in the 22 and 33 directions.

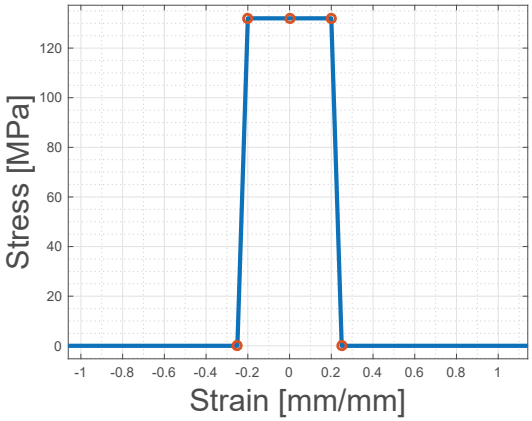

(c) Stress versus strain curve in the 12 and 31 directions.

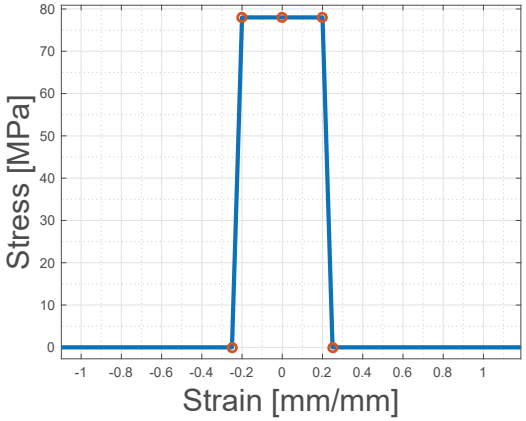

(d) Stress versus strain curve in the 23 direction.

Figure 3.5: Honeycomb material curves used.

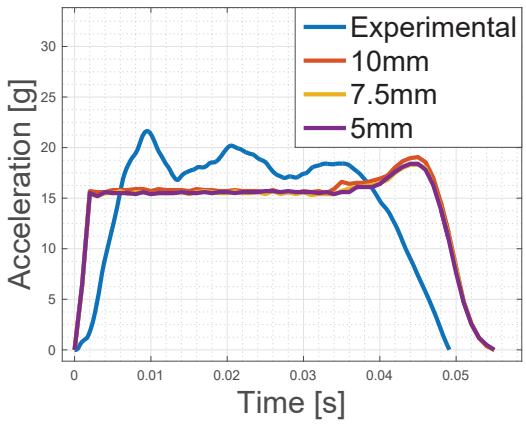

(a) Acceleration versus time.

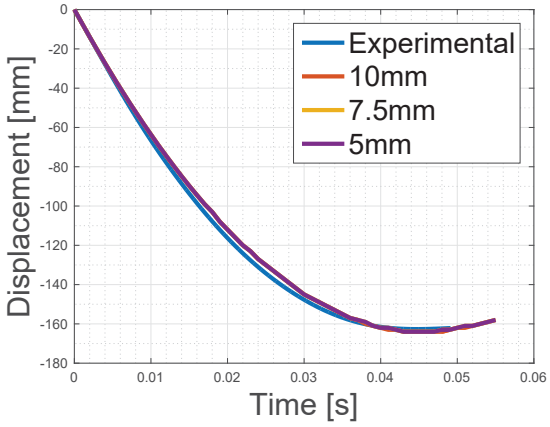

(b) Displacement versus time.

Figure 3.6: Mesh sensitivity analysis.

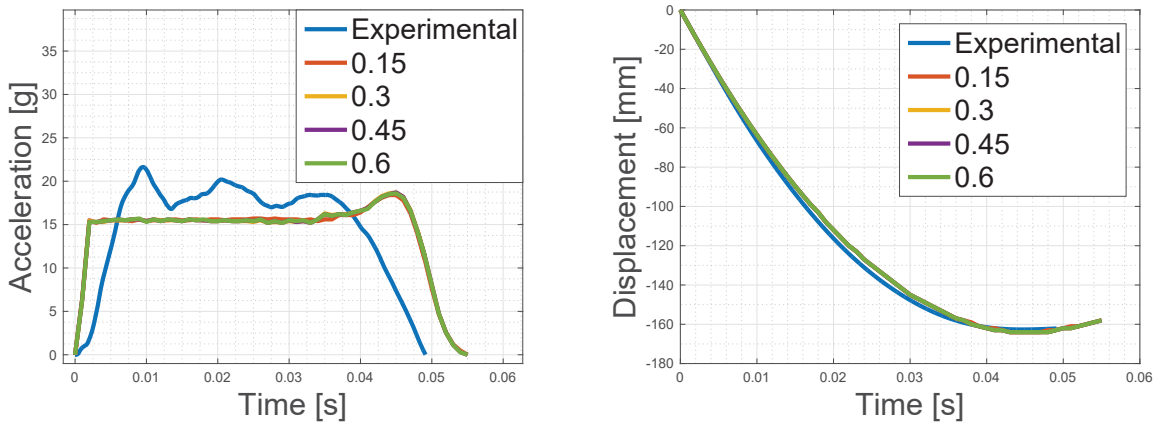

(a) Acceleration versus time.

(b) Displacement versus time.

Figure 3.7: Friction sensitivity analysis.

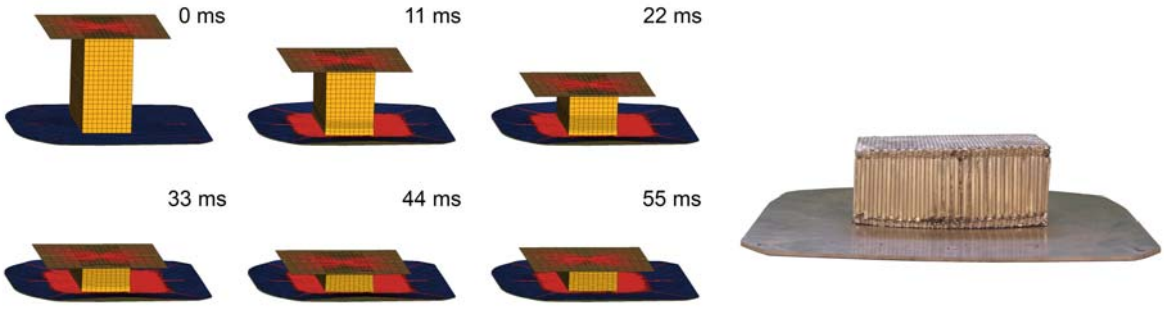

(a) Numerical deformation pattern.

(b) Tested crashbox.

Figure 3.8: Numerical and experimental deformation comparison.

3.2 FST07e

In section 3.1 a numerical model capable of predicting the behaviour of the current IAA solution was developed and validated. By updating the AIP and FBH geometry to the new car, the FST07e, it's possible to use the model to predict if a similar solution complies with the imposed rules.

A very similar mesh was used (figure 3.9(a)) and the resulting acceleration may be seen in figure 3.9(b). To model the IA 4000 solid elements were used with an unitary aspect ratio. 4895 shell elements were used to model the Barrier, the AIP and the FBH with a maximum aspect ratio of 2.55.

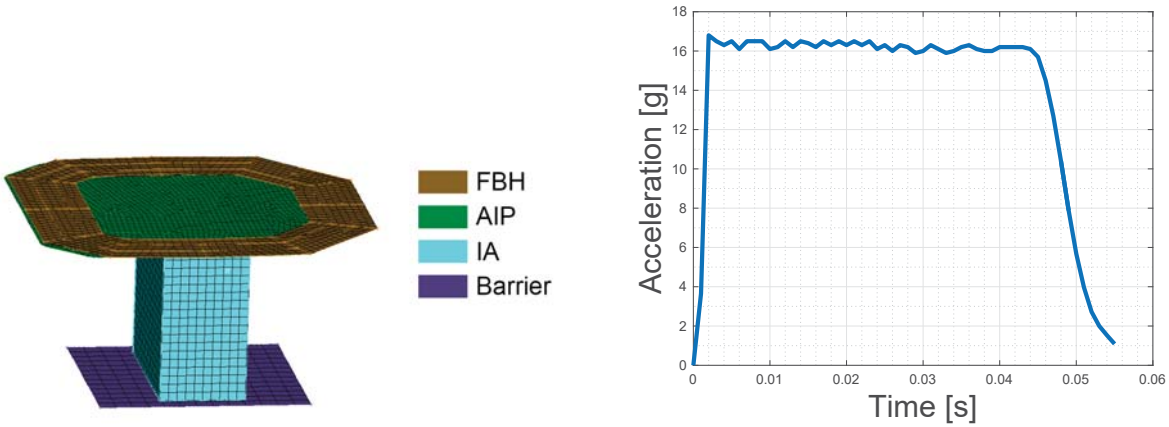

(a) Hypermesh [39] model.

(b) Acceleration results.

Figure 3.9: Hypermesh [39] model and acceleration results.

The maximum acceleration obtained was 168m/s^2 and the mean acceleration was 139m/s^2. Assuming a similar error to what was obtained in section 3.1, these values remain lower than the 40 *g* (maximum acceleration) and 20 *g* (mean acceleration) limit.

Thus, this is a valid solution for the IAA and will serve as the basis for this work. In table 3.3, a comparison between the IAA solution of the FST06e and the base solution presented on this chapter is made. Just by adapting the current solution to the FST07e, a 19.6% weight reduction is achieved due to the team's effort on attaining a lighter car:

- A smaller chassis reduced the AIP dimension and thus the weight.
- A new nose lay-up was also able to cut its weight by 57.1%.

Table 3.3: FST06e and FST07e IAA weight comparison.

	AIP [g]	IA [g]	Nose [g]	Total [g]
FST06e	1711	430	700	2841
FST07e	1554	430	300	2284
Change	**-9.2%**	**0%**	**-57.1%**	**-19.6%**

It is the aim of this work to not only analyse different solutions but also to design, manufacture and test a lighter IAA. Considering the different weights presented on table 3.3, it's clear that the AIP is the part with the most weight-saving potential, since it represents 68% of the total weight. However, an

optimized design of the AIP is strongly related to the IA. Different IA geometries and materials generate distinct loads, both in magnitude and direction. Besides, a structural nose may also be a possibility, which completely changes the design process of the AIP, since the loads short-cut straight to the FBH.

Taking this into consideration, the following chapters focus on achieving a better IA which is then studied with the AIP.

Chapter 4

IA Preliminary Simulations and Testing

4.1 Aluminium Tubes

4.1.1 Aluminium tubes - Experimental Analysis

Due to its simplicity, an aluminium tube was chosen as a first concept for a self-developed IA. In reality, this geometry couldn't be accepted by the FSAE rules, but it's a starting point for more complex geometries and a basis for the use of composite materials. A circular cross-section was chosen, due to its axisymmetry, with 90 millimetres of diameter, 300 millimetres of length and two millimetres of thickness.

The aluminium is an isotropic material, so the difficulty of the numerical analysis was reduced, as intended. The tubes used are represented in figure 4.1, where transversal black lines were drawn in order to better access the deformation pattern.

Figure 4.1: Aluminium tubes before test.

Regarding the experimental setup, the tubes were glued, with a two-component epoxy glue (*3M DP409*), to a 25 millimetres thick steel plate, which was then bolted to a 277 kg steel structure, as

represented in figure 4.2. The total weight of the assembly was of 300 kg, as required.

Figure 4.2: Aluminium tubes setup. The blue circles show the accelerometers position.

Two independent systems were used to record the event. Three *Bruel & Kjaer 4371* (Kjaer [36]) piezoelectric accelerometers, connected to three *Bruel & Kjaer 2635* charge amplifiers (Kjaer [36]), were glued to the bottom steel plate (figure 4.2) and one *Photron SA4* high speed camera was placed in front of the expected impact location.

Three accelerometers were used to account for possible small off-axis impacts, due to the gaps between the vertical beam structure and the steel mass. By using similar distances to the CG, one can average the three obtained curves to get the acceleration at the Centre of Gravity (CG). The accelerometers' sampling frequency was set at 51200 Hz.

The high speed camera served two purposes. Firstly, it was the only way to observe the failure mechanisms that take place locally in such a short time frame and, secondly, by using a tracker software, one can compute the displacement versus time plot, instead of having to compute a double integral over the acceleration data. The camera's frame rate was set to 8000 frames per second (fps). At this frame rate the resolution obtained was of 384 px wide and 1024 px high.

Regarding the data acquisition, a *National Instruments PXI* equipment (Instruments [37]) was used to sample the three accelerations.

The frames obtained from the high speed camera can be observed in figure 4.3. As one can see, a concertina mode of failure was obtained. While the first tube folded eight full times, the second only folded seven times and began the eighth.

During post-processing, the frames obtained were cropped, the brightness was changed and the images were converted to grayscale. After this transformation, a tracking algorithm was implemented in order to retrieve the displacement versus time plot of the steel mass during the impact. The diagram presented in figure 4.4 shows the algorithm used.

By using the algorithm on the image data from the first and second tests, the displacement versus time plot was achieved, as shown in figure 4.5. The difference observed on the maximum displacement between the first and second tests was probably due to a small difference on the initial velocity. Besides,

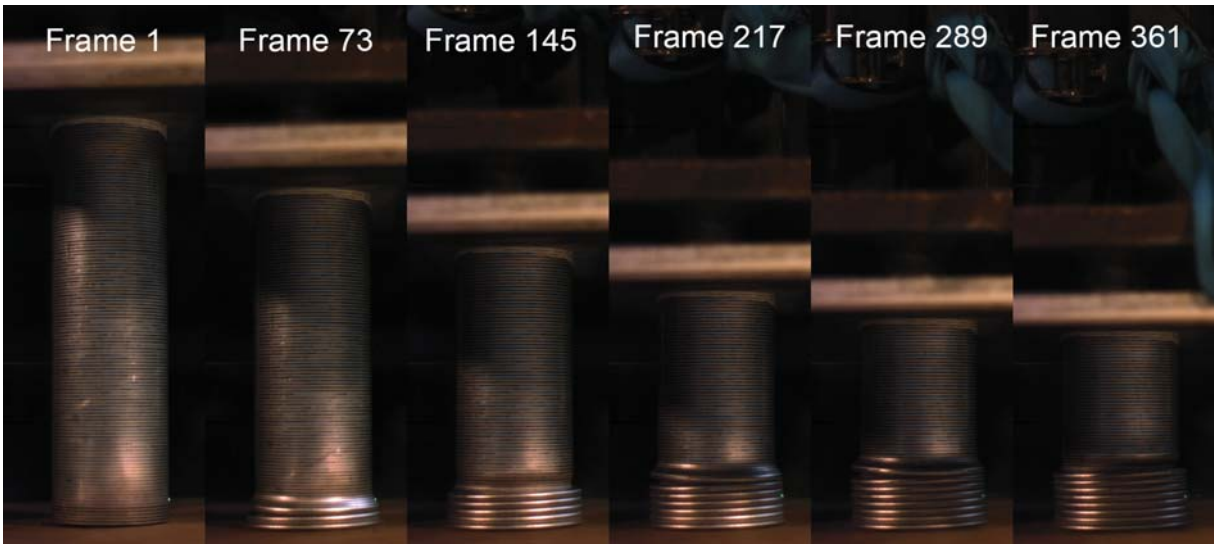

(a) First test.

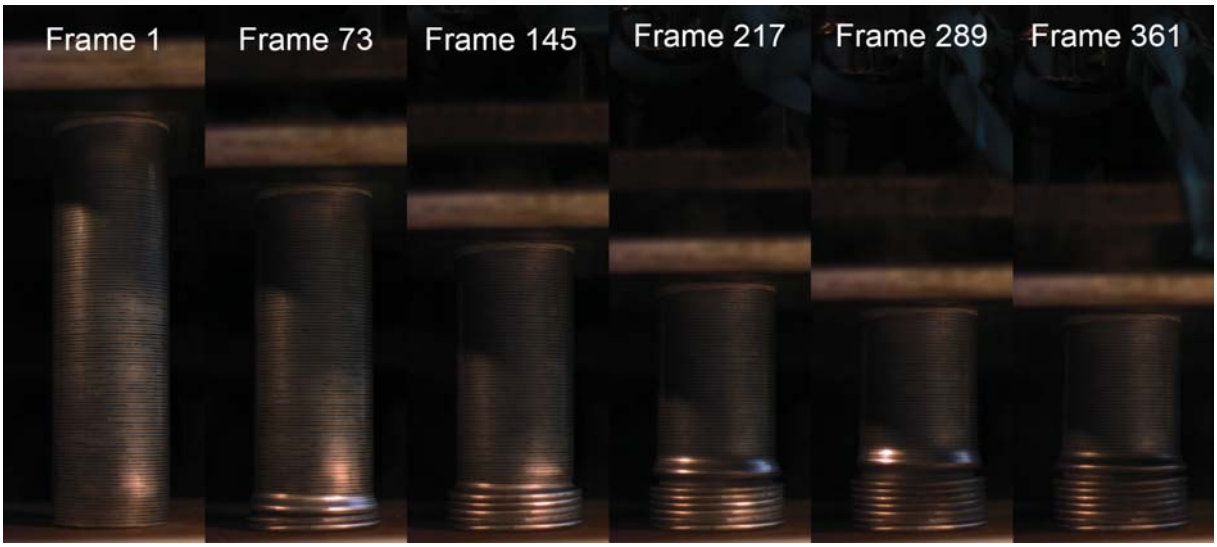

(b) Second test.

Figure 4.3: Frames from the high speed camera.

as already observed, the second test didn't fully folded the eighth time.

Regarding the accelerometers, the raw data from the first test can be observed on figure 4.6(a). The third accelerometer was not considered due to a problem on the attachment to the steel base. The raw data presents a chaotic evolution with acceleration peaks above 1600m/s^2. A low-pass filter had to be employed in order to eliminate undesired frequencies. The FSAE rules state that, if an acceleration peak above 40 *g* is present on the data, a third order Butterworth filter with a cut-off frequency of 100 Hz may be applied. In figure 4.6(b) this filter was applied, however a DC component can clearly be seen. In figure 4.6(c), a Butterworth high-pass filter was applied in order to remove this component. Finally, in figure 4.6(d), an average between the two accelerometers was performed.

The raw data from the second test can be observed in figure 4.7(a) and it has a similar chaotic behaviour to the raw data from the first test. The accelerometer number one was not considered due to a similar attachment problem to the first test. After the same low-pass filter was applied (figure

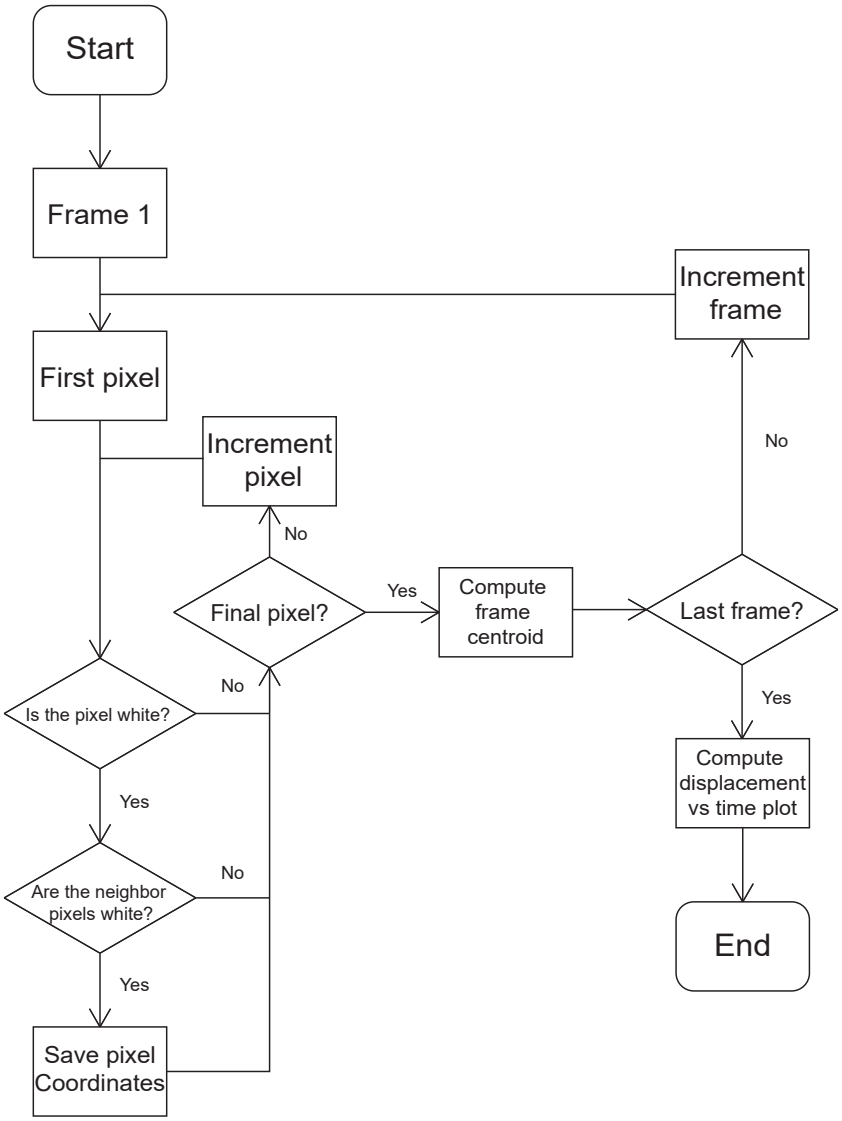

Figure 4.4: Tracking algorithm implemented.

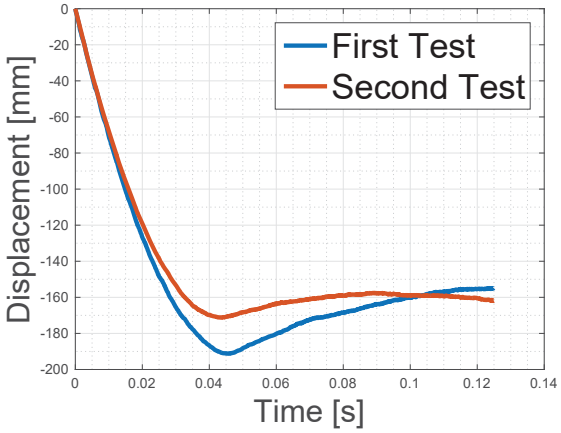

Figure 4.5: Displacement versus time plot of the aluminium tubes.

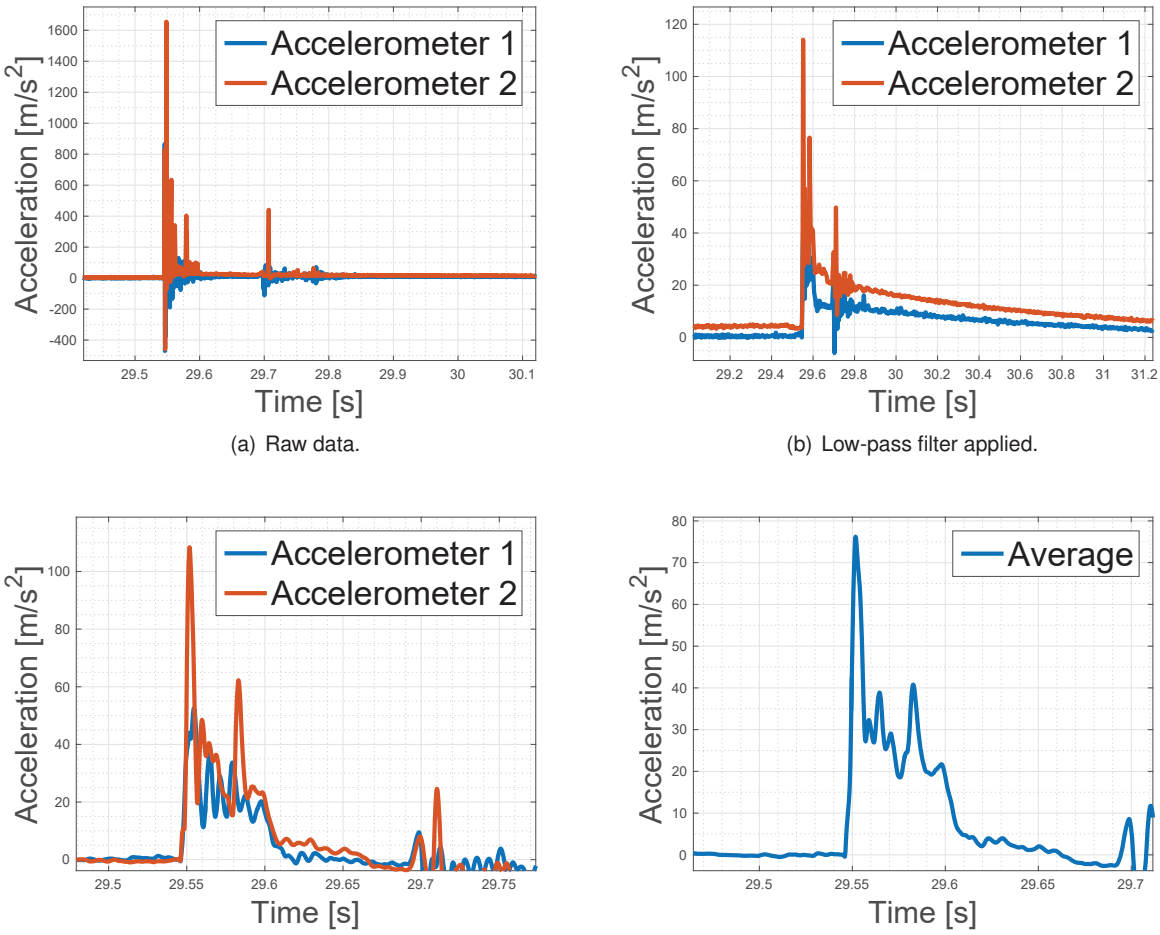

(a) Raw data.

(b) Low-pass filter applied.

(c) High-pass filter applied.

(d) Accelerometers average.

Figure 4.6: Post-processing of the accelerometer data from the first test.

4.7(b)) lower accelerations were obtained. However, higher accelerations are present, when compared to the first test. Performing the accelerometers average (figure 4.7(c)), a peak of almost 100m/s^2 was obtained. The lack of the third accelerometer may explain the differences between the two tests, as one of the degrees of freedom was not accounted for.

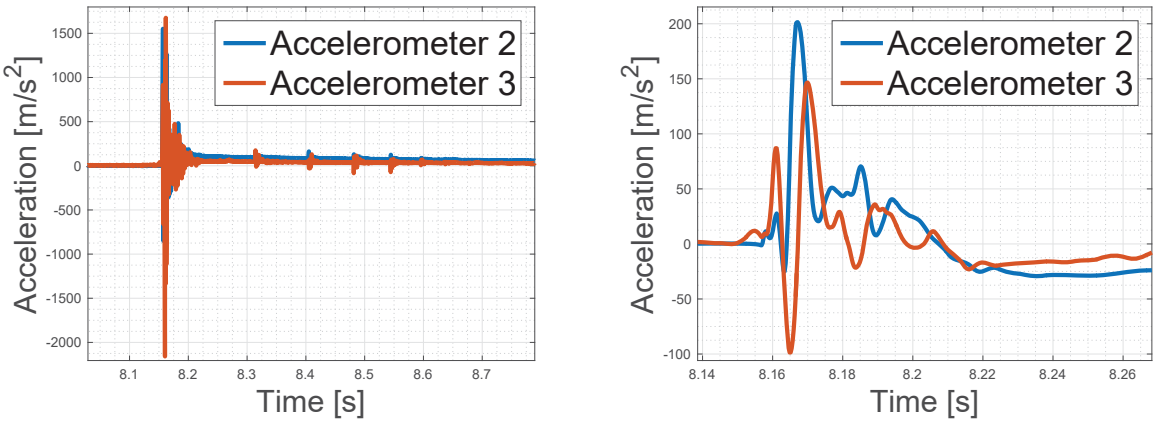

(a) Raw data.

(b) Low-pass filter applied.

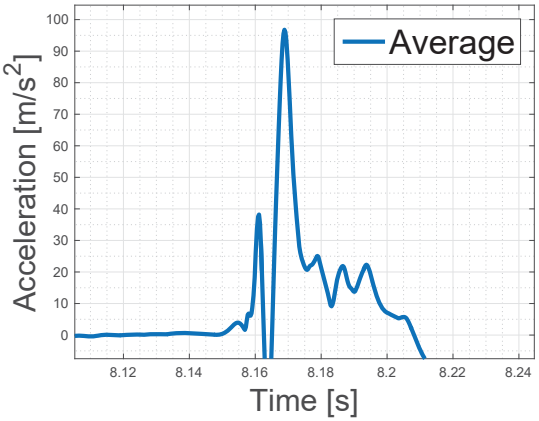

(c) Accelerometers average.

Figure 4.7: Post-processing of the accelerometer data from the second test.

4.1.2 Aluminium tubes - Numerical Model

After the experimental tests with the aluminium tubes, a numerical model was developed. A good characterization of the material used is a must when performing a finite element analysis. In this case, quasi-static tension tests were performed to aluminium rods (figure 4.8(a)). It was certified by the supplier that the aluminium of the rods was the same as the one of the tested tubes (EN AW 6060). A mechanical strain gauge was used to determine the displacement over time (figure 4.8(b)).

From the experimental tests, the data was fit by a bi-linear curve. A Young's modulus of 70 GPa and a tangent modulus of 200 MPa was considered (figure 4.9).

With the material fully characterized, the numerical model could be developed in Abaqus [8] Explicit. The tube was modelled using four node explicit shell elements, element R3D4 in Abaqus [8] (4.10), using reduced integration with default hourglass control. The material was considered to follow an isotropic hardening rule. A supporting plate and an impacting plate were also modelled using rigid elements, element S4R in Abaqus [8]. A mass of 300 kg was associated with the impacting plate. A general contact (with self-contact) rule was used between the tube and the impacting plate, and between the tube and the supporting plate. Due to the simple geometry, a structured mesh was used. An encastre

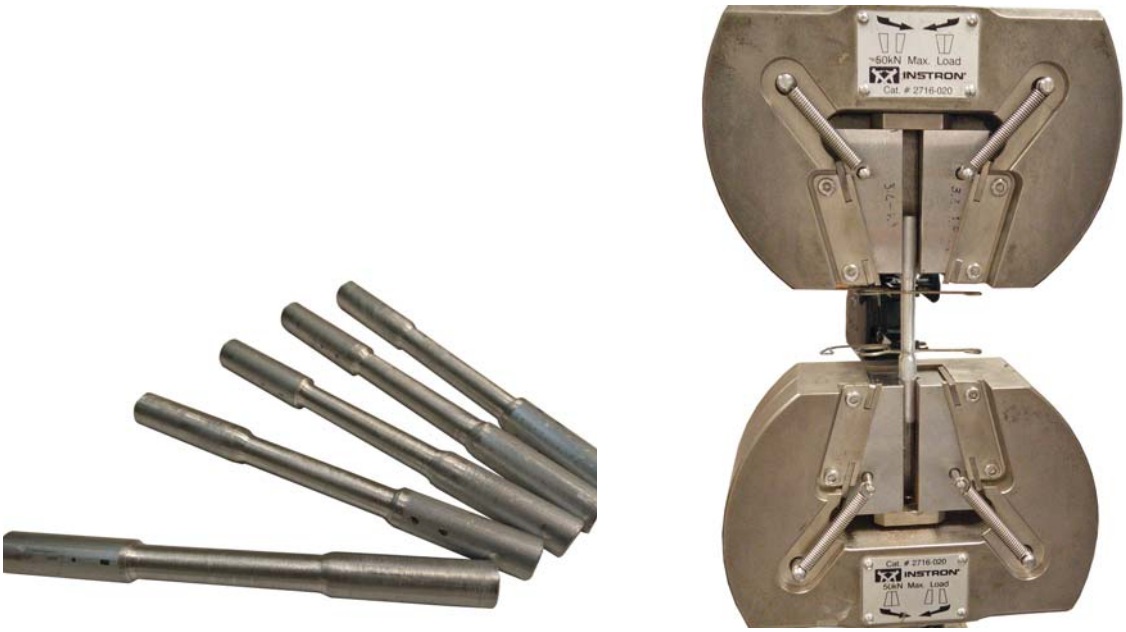

(a) Aluminium rods before test.

(b) Aluminium rods during the tension test. Notice the mechanical strain gauge.

Figure 4.8: Material characterization tests.

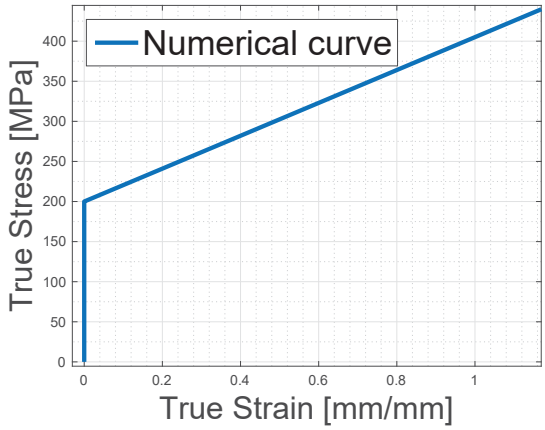

Figure 4.9: Numerical True Stress versus True Strain curve implemented.

boundary condition was imposed on the supporting plate and the impacting plate had its transversal directions and rotations locked. An initial condition of $7m/s$ was also imposed on the impacting plate.

In figure 4.11, a mesh sensitivity analysis was performed with meshes ranging from 1.5 mm to 10 mm. The increase in maximum displacement with the decrease of element size was expected due to the increase of degrees of freedom and thus the softening of the structure. Comparing the displacement versus time plot for every mesh element size, it was concluded that the 3 mm mesh converged due to the similarity between the 3 mm, 2 mm and 1.5 mm curves. Using a 3 mm mesh results in 11578 elements with an aspect ratio of 1.

The failure mode is also affected by the mesh element size. In figure 4.12 one can see the final frames for each mesh size. The 10 mm mesh is the only one that predicts a diamond shape mode. The 7.5 mm mesh only predicts five folds, the 5 mm mesh predicts seven folds while the 3 mm, 2 mm and

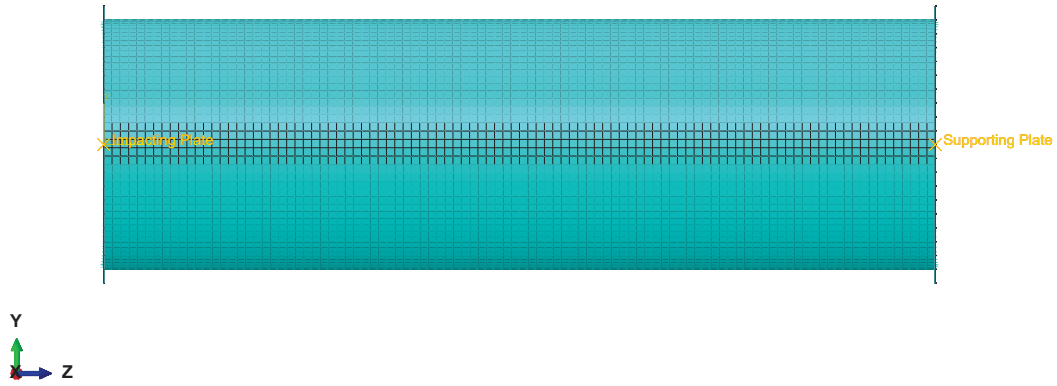

Figure 4.10: Abaqus aluminium tube model.

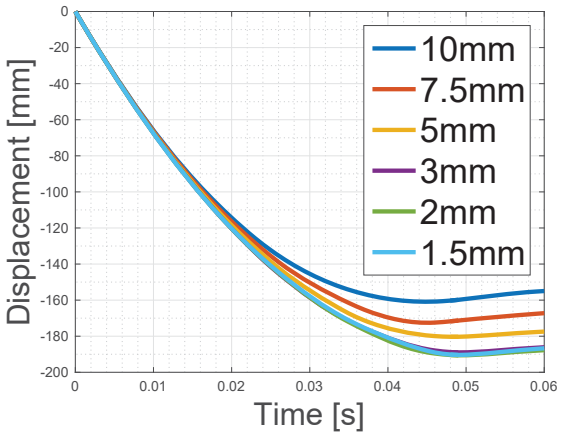

Figure 4.11: Aluminium tubes mesh sensitivity analysis.

1.5 mm predict eight folds.

Similarly to section 3.1 the friction coefficient must be analysed. First, a friction sensitivity analysis is performed, in order to access its importance during the impact, then the failure mode is again analysed. In figure 4.13, the displacement versus time for different values of friction coefficient is presented. The maximum variation between the curves is only 3 %, which points to a very low influence on the simulation outcome. However, in figure 4.14, the last frame from each simulation is presented and, even though the change in the displacement through time is small, there are changes to the failure mode.

With a null coefficient of friction, an inversion failure mode is obtained initially and then it shifts to a diamond shape mode. Increasing the friction coefficient to 0.3, a concertina mode of failure is first obtained followed by a diamond shape mode. Only at 0.4 and 0.5 a full concertina mode of failure is reached. If the friction continues to increase, at 0.6, the diamond shape mode is obtained again. According to Ramsdale [41] the sliding friction coefficient between steel and aluminium is 0.47, which is consistent with the numerical results.

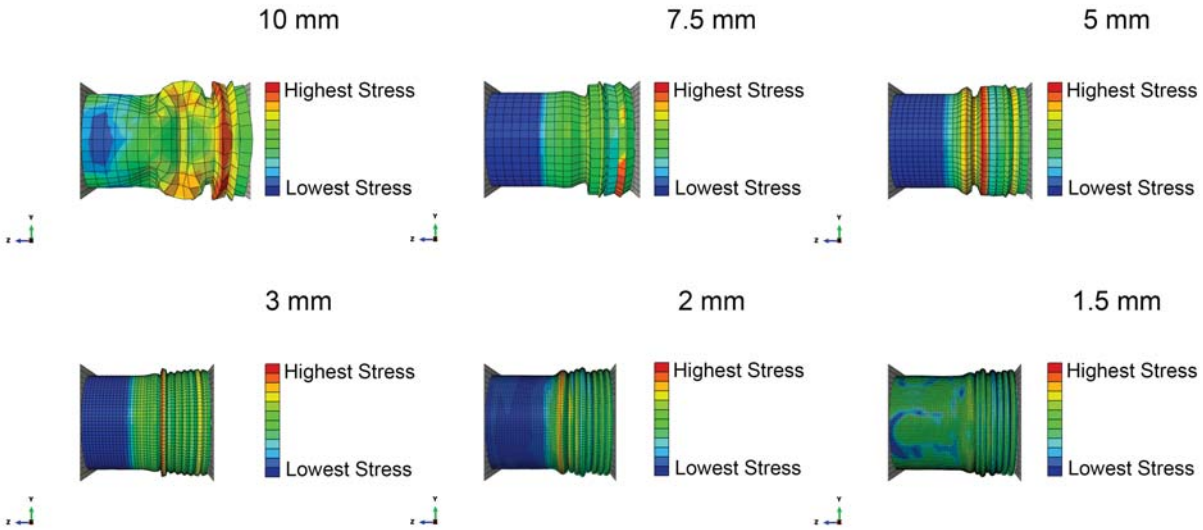

Figure 4.12: Failure mode according to mesh element size.

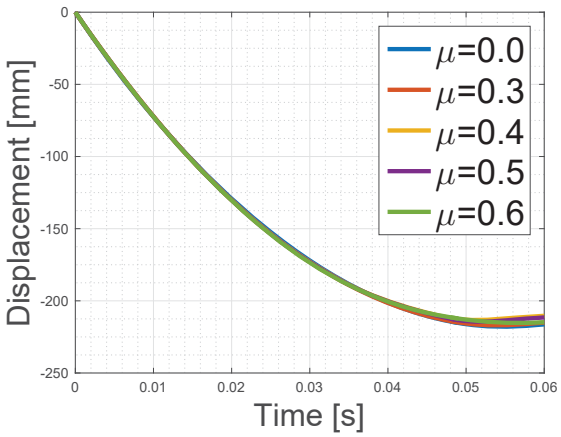

Figure 4.13: Aluminium tubes friction sensitivity analysis.

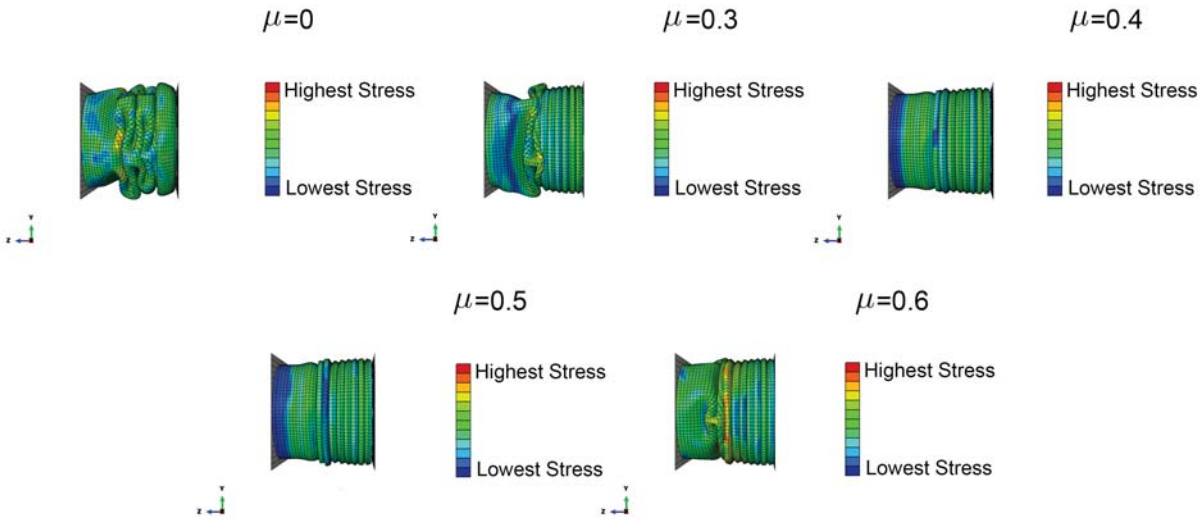

Figure 4.14: Failure mode according to the friction coefficient.

Finally, the initial velocity was changed in order to better access the influence of this parameter. With the mesh element size and coefficient of friction determined it is also possible to compare the outcome with the experimental results, see figure 4.15. This plot, in combination with the number of folds, already discussed in section 4.1.1, supports the theory that the first test had an higher initial velocity, approximately 0.5m/s higher. In figure 4.16 an overview of the final deformation shape results is provided.

A maximum error of 3.5% was thus obtained between the first test and the numerical model prediction. As for the second test, a maximum error of 5.5% was achieved.

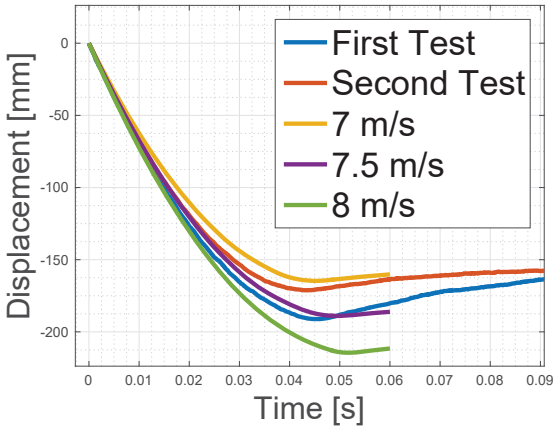

Figure 4.15: Initial velocity variation.

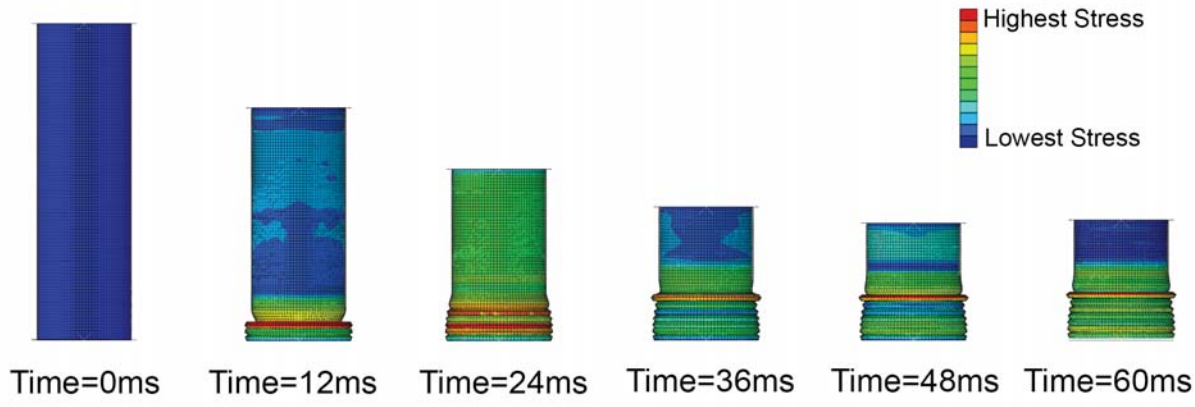

Figure 4.16: Final results from the aluminium tubes simulation.

4.2 Carbon Fibre tubes

4.2.1 Carbon Fibre tubes - Experimental Analysis

After having successfully tested and modelled the aluminium tubes, the next step was to model an orthotropic material such as carbon fibre, while maintaining a simple tube geometry. The material used was pre-impregnated, uni-directional tape, carbon fibre. The mechanical properties used are presented

Table 4.1: Carbon fibre mechanical properties used.

E_x [GPa]	234.17	ν_{xy}	0.32
E_y [GPa]	6.02	Thickness [mm]	0.27
G_{xy} [GPa]	6.20		

on table 4.1. These properties were obtained using tension specimens, cured using similar conditions to the tubes tested, equipped with strain gauges. Each ply has a thickness of 0.27 mm, which accounts to 2.16 mm, as the tube was laminated with a total of eight layers.

Taking into account the purpose of this work, the lay-up was defined as $[(0^\circ/90^\circ)_2]_s$ simply due to manufacturing easiness, as virtually any given lay-up would be a good starting point. The manufacturing of the tubes is shown in figure 4.17, where one can see the 0° and 90° plies being applied. Each tube has a similar geometry, with 90 millimetres of inner diameter and 290 millimetres of length.

Figure 4.17: Manufactured carbon fibre tubes.

A very similar setup to the aluminium tubes was used. The accelerometers' sampling frequency was set at 51200 Hz and the camera's frame rate was set at 7500 fps. At this frame rate, the resolution obtained was of 448 px wide and 976 px high.

Three carbon fibre tubes were tested. However, the first test was considered invalid due to a setup problem.

Looking at the frames retrieved from the high speed camera during the second test (figure 4.18(a)), one can conclude that a stable crush front was achieved and that the tube was able to absorb the required energy without collapsing completely.

Figure 4.18(b) contains six frames taken from the third test. A similar stable crush front was obtained and the tube was once again able to absorb the required energy.

Due to the amount of flying debris it wasn't possible to use the algorithm developed in section 4.1.1. However, using the entire set of frames and the open-source program Tracker [42], the vertical position of the weight was tracked, after which a conversion from pixels to millimetres was needed. By using previously known distances, such as the tube diameter and length, one is capable of performing such conversion with fairly good accuracy. Finally, a plot of the displacement versus time can be obtained using only the camera's information (figure 4.19).

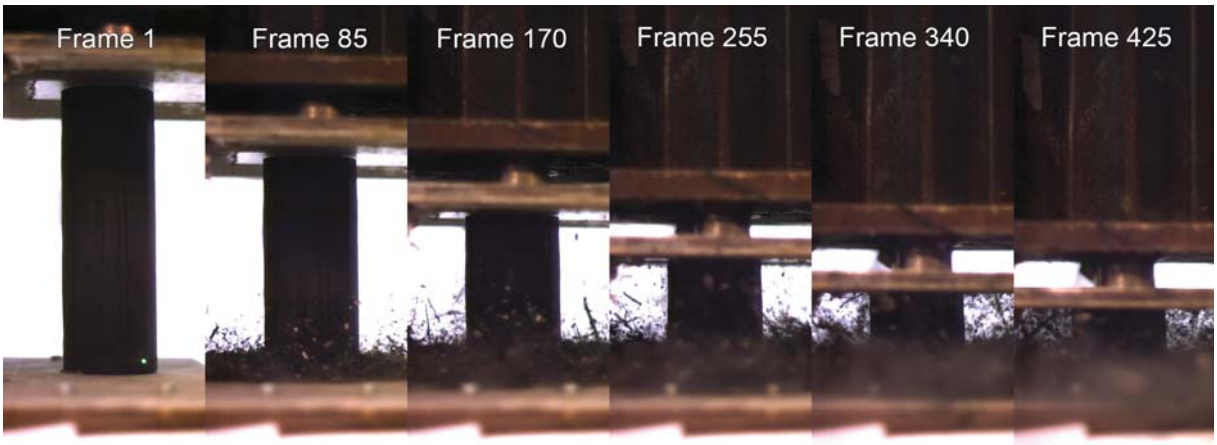

(a) Second test.

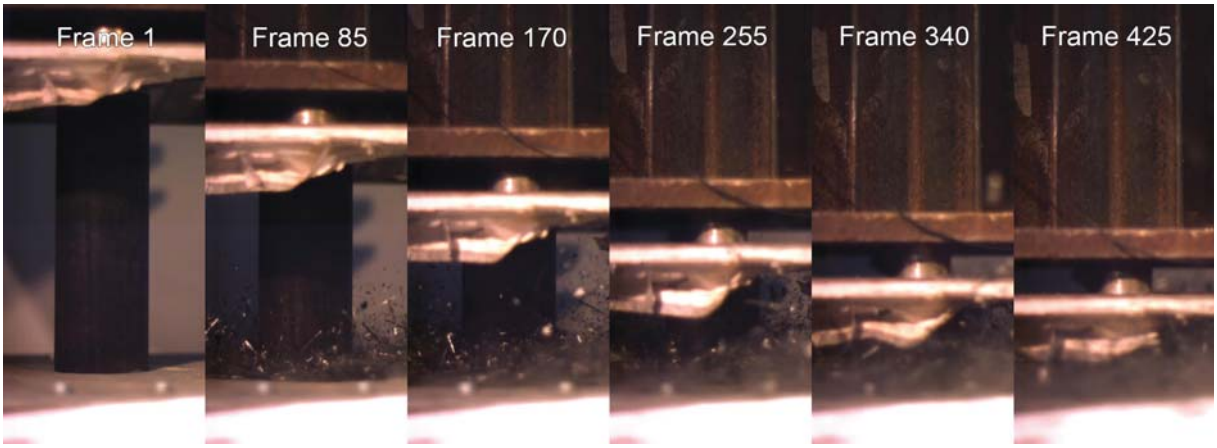

(b) Third test.

Figure 4.18: Frames recorded by the high speed camera during the carbon fibre tube's test.

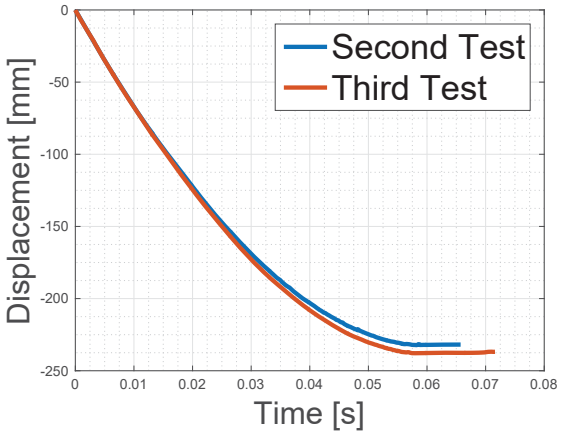

Figure 4.19: Displacement versus time plot computed using the high speed camera data for the carbon fibre tubes.

Analysing the plot of figure 4.19, one can conclude that both tests were fairly similar, with a maximum difference of 2.4 % between them.

Regarding the accelerometers, the raw data presented a seemingly chaotic evolution (figure 4.20(a)). A low-pass filter had to be employed to eliminate undesired high frequencies. A third order low-pass Butterworth filter with a cut-off frequency of 100 Hz was used. This is the filter recommended by the

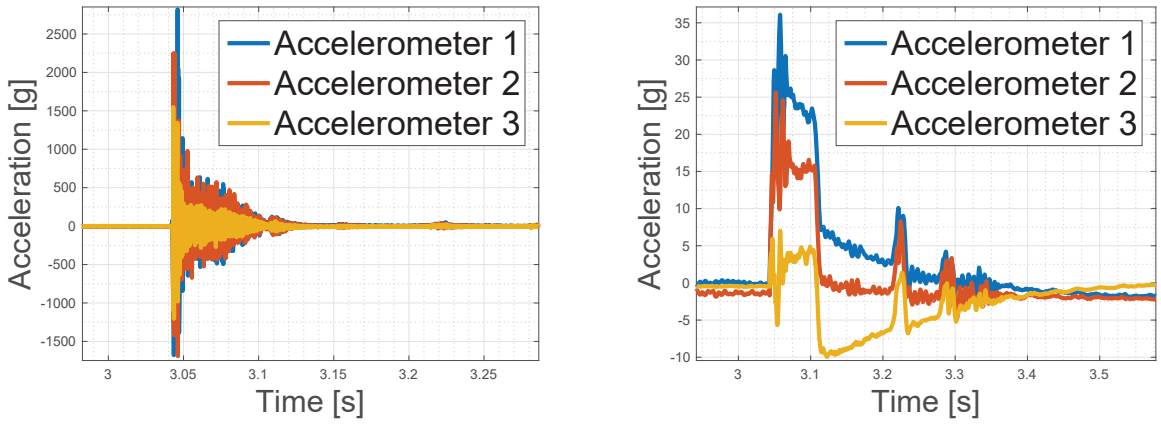

(a) Raw data.

(b) Low-pass filter applied.

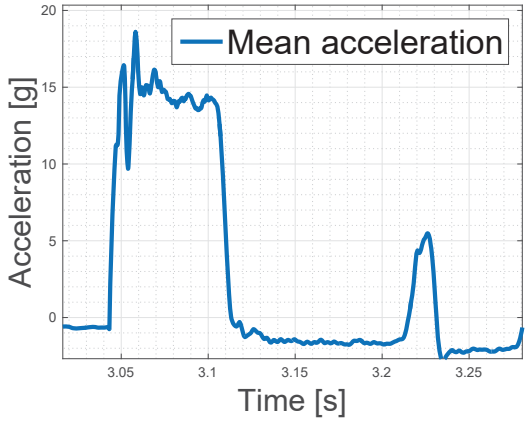

(c) Accelerometers average.

Figure 4.20: Post-processing of the accelerometer data from the second test of the carbon fibre tubes.

FSAE rules, when accelerations higher than 40g are present on the raw data, as explained in section 2.6.

Considering the filtered data from the second test (figure 4.20(b)), one can see the three accelerometers present a very similar behaviour with an offset between them. This was expected and it is the reason why three accelerometers were used. By averaging the three curves, the acceleration curve at the CG was obtained (figure 4.20(c)).

The third test presented a very similar chaotic data (figure 4.21(a)). Following the same procedure as used for the second test a low-pass filter was applied (figure 4.21(b)). However, on the third test, a DC component can be clearly seen. Due to this effect, a high-pass filter was also applied. A second order high pass Butterworth filter, with a cut-off frequency of 0.5 Hz, was used to attenuate this behaviour. Figure 4.21(c) presents the result with the additional average of the three accelerometers.

In figure 4.22, a comparison between the two peaks obtained is performed. Both curves are similar for the first 10 ms but, afterwards, the acceleration curve from the third test is substantially lower than the second test. Taking into account that the tests were performed under the same conditions, and analysing the results obtained from the camera, it was expected that the second test would have reached an higher acceleration, due to the smaller displacement observed in figure 4.19, but the difference here may also

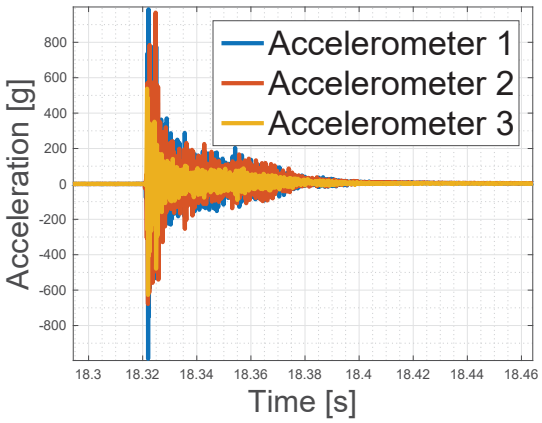

(a) Raw data.

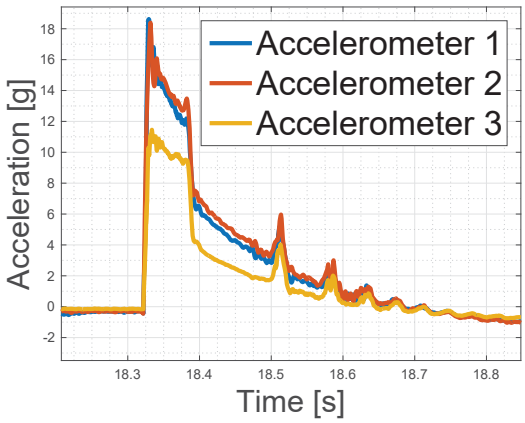

(b) Low-pass filter applied.

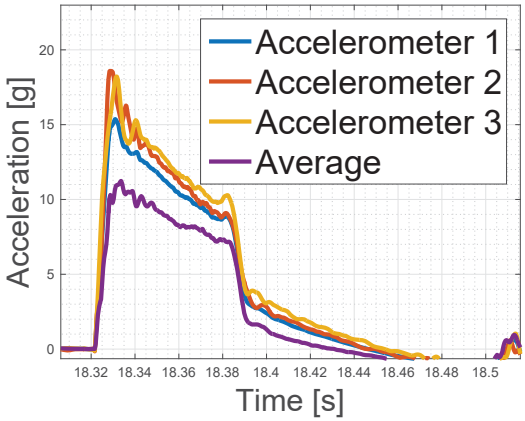

(c) High pass filter applied and accelerometers average.

Figure 4.21: Post-processing of the accelerometer data from the third test of the carbon fibre tubes.

be explained by the DC component not being fully removed. However, if an higher cut-off frequency is used, in the high-pass filter, significant components of frequencies start to be removed.

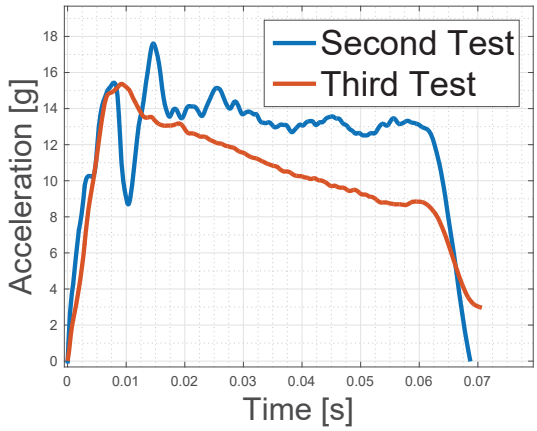

Figure 4.22: Acceleration plots, high-pass filter with average and impact peak comparison.

4.2.2 Carbon Fibre tubes - Numerical Model

Regarding the numerical model, a commercial finite-element software - Abaqus [8] Explicit with the CZone [3] algorithm - was used in order to simulate the full impact. The CZone [3] add-on provides a relatively new methodology to simulate composite structures under impact. It simplifies all the complex physics that take place at the crush front including, for instance, delamination, localised fibre buckling, matrix failure, among other failure modes, by a constant property called Crush Stress. This property is, by definition, the stress required to maintain a stable crush front. Besides, Abaqus [8] Explicit with CZone [3] can also predict catastrophic failure outside the crush front. This approach is much simpler than a full model analysis and can save substantial amounts of time, which may become critical during a lay-up optimization of a complex structure. The main difficulty of the use of this method is now related to the accurate measurement of this property, which can also change with the number of layers and their orientation.

With this in mind, an isotropic Crush Stress was considered and, as it was the only unknown variable, it was iterated until a good fit to the experimental data was achieved. Later, a test methodology was defined, similar to the one proposed by the CZone [3] documentation, in order to verify this parameter and to be able to predict this property in the future, without a full-model experimental testing.

The tube was modelled using four node explicit shell elements, element S4R in Abaqus [8]. The weight was modelled as a rigid plate by four node rigid elements, R3D4 in Abaqus [8], with a mass of 300 kg. A contact pair was established between these two parts following the CZone [3] methodology. In figure 4.23(a), one can see the tube and plate meshed in Abaqus [8], where the red line represents the fixed boundary condition applied.

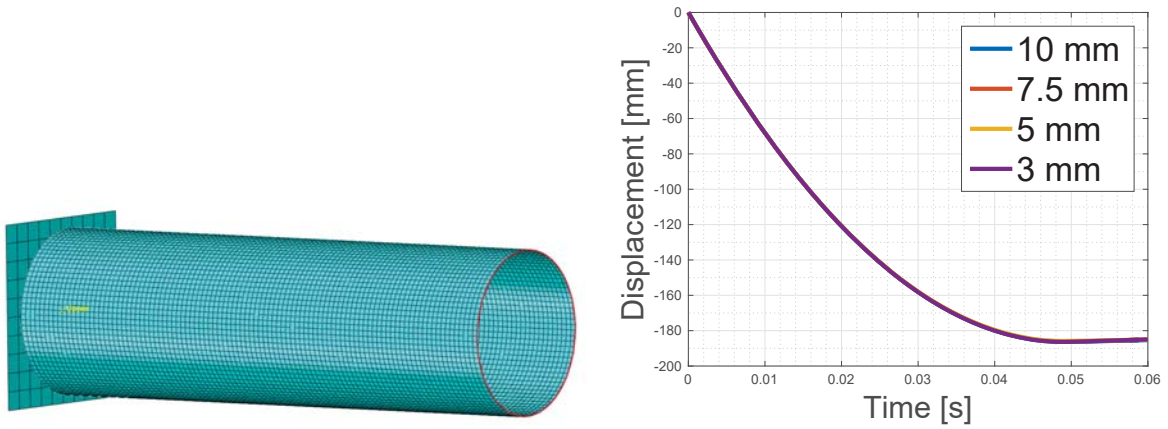

(a) Numerical model in Abaqus [8].

(b) Displacement versus time plot using several mesh sizes.

Figure 4.23: Numerical model and mesh sensitivity analysis.

A mesh sensitivity analysis was performed. In figure 4.23(b), the displacement versus time plot may be observed for meshes ranging from 10 mm to 3 mm. As one can see, the four curves are overlapping. The tested tubes present a constant cross-section and the direction of impact may also be considered constant relatively to each layer. This means that an isotropic Crush Stress can be considered and also that, if the tube doesn't fail catastrophically outside the crush front, the numerical analysis is expected

to be almost mesh-size independent, as observed. The displacement and acceleration were measured in the reference point of the impacting rigid wall.

As already explained at the beginning of this section, the Crush Stress was iterated until the simulation results fitted the experimental values. Figure 4.24(a) compares two different values of Crush Stress with the experimental data. While the second test was found to have a fitted Crush Stress of 68 MPa, the third test was fitted with a Crush Stress of 66 MPa, with 4 % and 2 % error, respectively. Figure 4.24(b) shows a similar comparison but with the acceleration data. As expected, the experimental curve is much more chaotic than the simulation. This is fundamentally related to how the Crush Stress is defined and the fact that it was considered to be an isotropic constant property. However, even considering these assumptions, the simulation can still provide an approximation for the displacement curve of both tests with an error under 5 %.

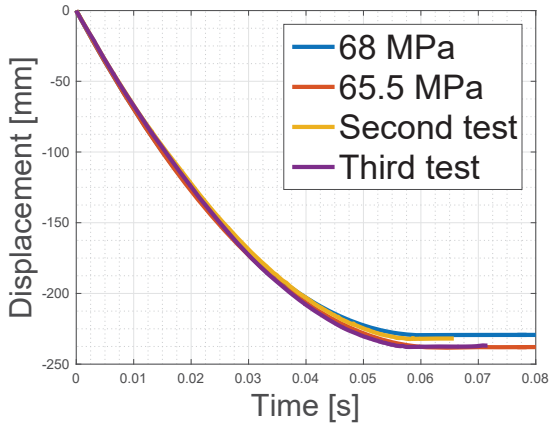

(a) Comparison between the fitted simulation and the experimental displacement results.

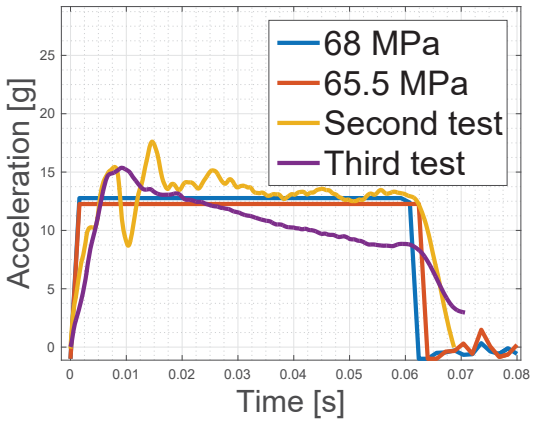

(b) Comparison between the fitted simulation and the experimental acceleration results.

Figure 4.24: Numerical model and experimental comparison.

Considering the results above, one can conclude that the Crush Stress of this particular lay-up, when subjected to this particular direction of impact, is between 65.5 MPa and 68 MPa. On figure 4.25, the frame results from the simulation are presented. Like in the experimental setup, a stable crush front was achieved with no catastrophic failure.

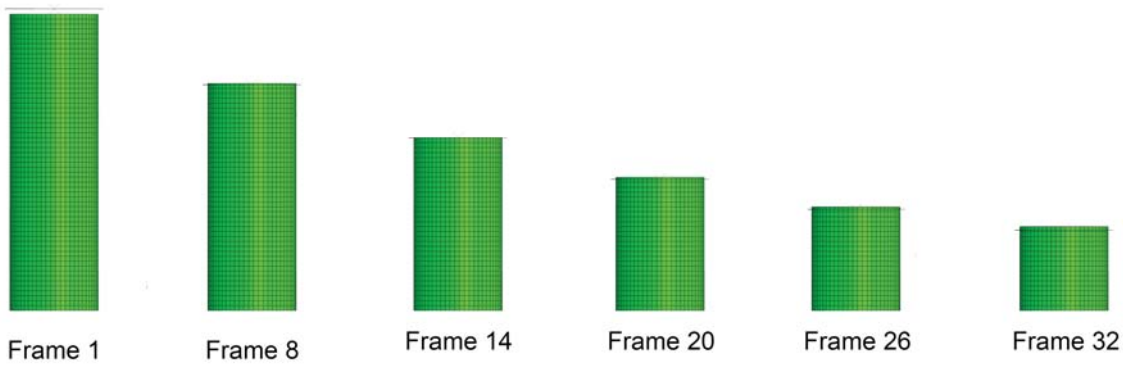

Figure 4.25: Frame results from the Abaqus [8] simulation.

4.2.3 Carbon Fibre tubes - Crush Stress Validation

In section 4.2.2, the Crush Stress was fitted to the experimental data. However, it is not feasible to continually test full scale components in order to achieve a crash-worthy lay-up design. A different, simpler, method to compute the Crush Stress is needed. Abaqus CZone [3] provides documentation where it proposes a compression crush test.

Firstly, a carbon fibre plate with a similar lay-up to the one used on the tubes was manufactured. After the plate was cured, several test pieces were cut. Four specimens were cut at 0°, meaning the orientation of the specimens was the same as the fibre. Small indentations were left at the top in order to induce high stress points meant to initiate a stable crush front (figure 4.26(a)).

A die was produced with an horizontal surface meant to crush the specimen and a lateral wall prevented buckling. A steel matrix was also manufactured with two gaps designed to let the die pass-through while supporting the base of the test piece. The setup used can be seen in figure 4.26(b), where the test specimen was placed between the die and the matrix. A quasi-static velocity of 10mm/min was used. The two gaps on either side of the die, near the top, allowed the test specimen to exit freely through the lateral. The same mode of failure was observed during the test of the carbon fibre tubes.

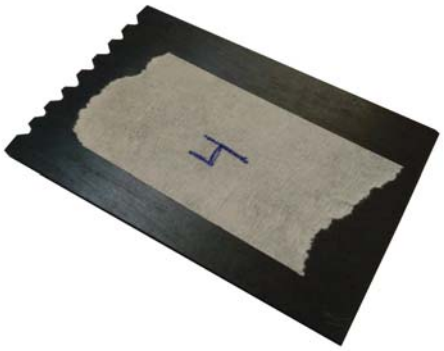

(a) Test specimens cut at 0° with small indentations on the top.

(b) Setup used for specimen crushing.

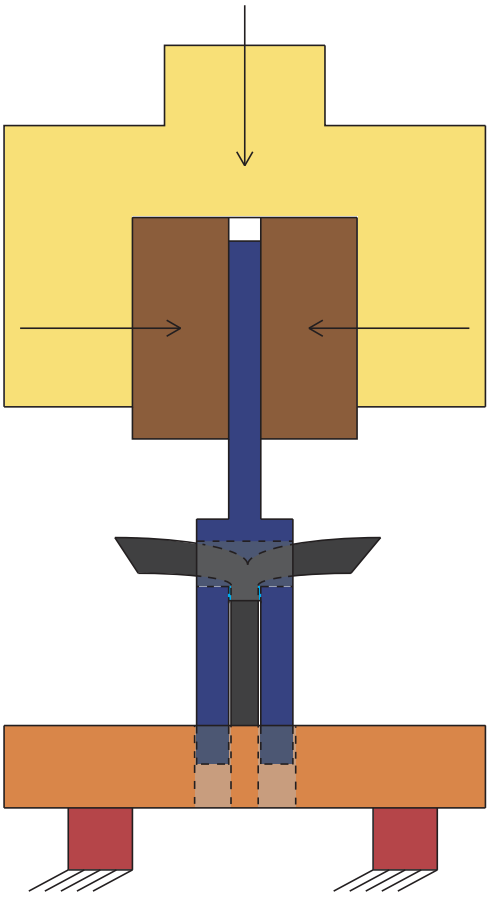

(c) Setup schematic.

Figure 4.26: Crush stress setup and specimens.

To further clarify the test performed, a schematic is presented in figure 4.26(c), where the red and

orange components represent the fixed steel base seen on figure 4.26(b). The die is represented in blue and the downward momentum of the upper clamp forces it to pass through the steel plate while crushing the specimen.

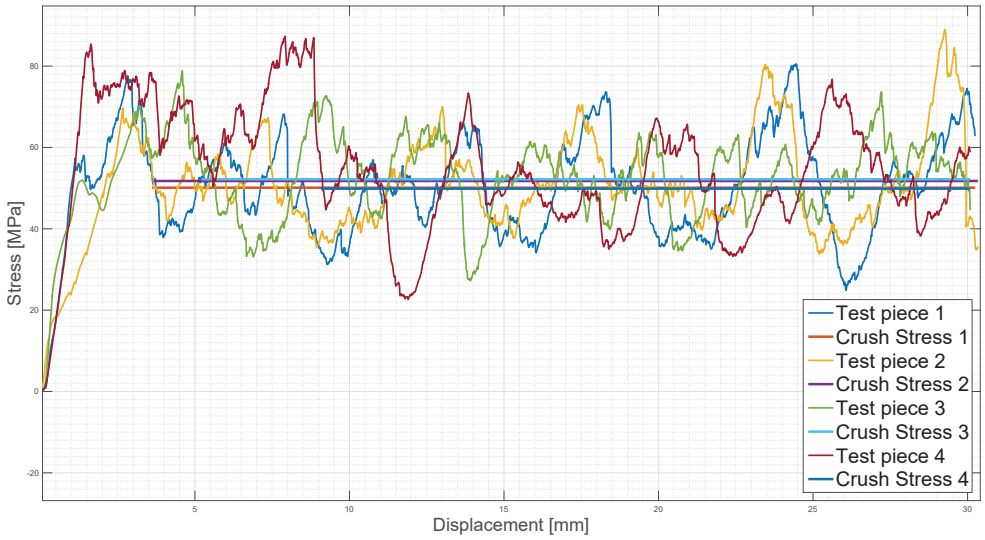

Figure 4.27: Stress versus displacement plot results.

The stress versus displacement plots are presented in figure 4.27. After the initial peak, the stress results fluctuate around a constant value. By computing the average of the four tests one can achieve the Crush Stress value.

The mean Crush Stress of the four specimens is 51MPa with a maximum variation of 2%.

In section 4.2.2, the fitted Crush Stress value was in average of 66.75MPa. The value obtained using the test specimens is 23.6% lower than the one obtained through simulation fitting.

This lower value may be justified by dynamic effects which aren't considered in a quasi-static setup. Mamalis et al. [43] showed that the SEA increased during dynamic loads, when compared to static loads, which may explain the lower Crush Stress obtained.

Nevertheless, this method proved to be a very simple and quick way of assessing the Crush Stress value, even though additional tests have to be made, with identical conditions between full model and test specimens, in order to achieve a better crash behaviour prediction.

Chapter 5

IA Simulations and Optimization

5.1 Crush Stress Prediction

In section 4.2.3, the Crush Stress was obtained through experimental tests of small rectangular specimens and compared with the fitted numerical value in section 4.2.2. Even though the error obtained was of 23,6%, it remains a simple, quick and very cost-effective way of obtaining a Crush Stress reference value. It must be noted, however, that this value must be used with caution as it may not accurately represent reality. With this in mind, a set of tests to the carbon fibre available to use in the impact attenuator was planned and executed.

A different carbon fibre than the one used in section 4.2 was supplied by the team. The new material differs from the previous as it is bi-directional prepreg, twill woven, high strength, carbon fibre.

A carbon fibre plate with ten layers was manufactured (figure 5.1(a)), where each layer had 0.23 mm of thickness, which accounts to 2.3mm of thickness. The plate was then cut by a water-jet machine following the lay-out presented on figure 5.1(b) (notice the top indentations). As opposed to section 4.2.3, the objective of this test is to obtain an orthotropic Crush Stress. To accomplish that, the specimens were cut with different inclinations in intervals of 15° .

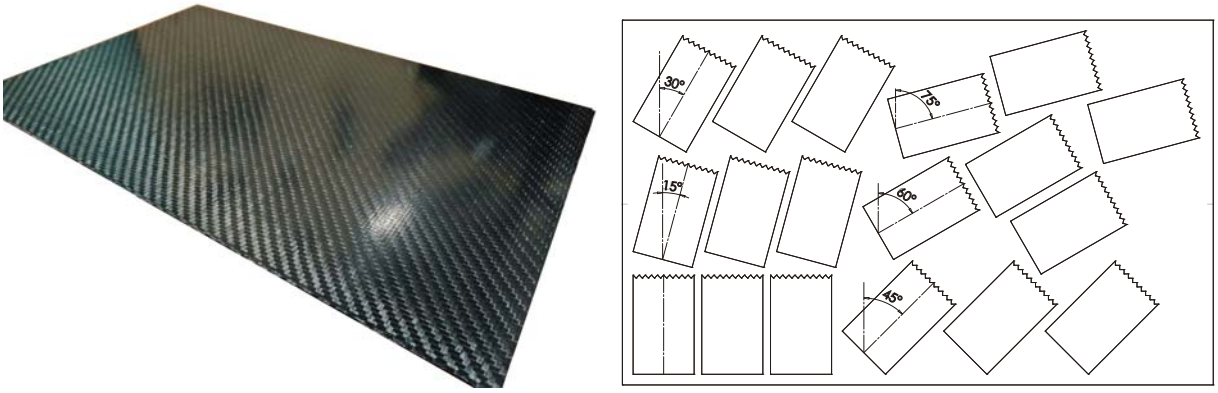

(a) Manufactured carbon fibre plate.

(b) Cutting lay-out.

Figure 5.1: Manufactured plate and cutting lay-out.

The same method, as used in section 4.2.3, was used to test the specimens. The die was fixed to

the upper clamp of an electromechanical compression test machine and the specimens were effectively crushed between the die and a bottom steel plate, as observed in figure 5.2. A similar crush behaviour was observed with delamination occurring through either side.

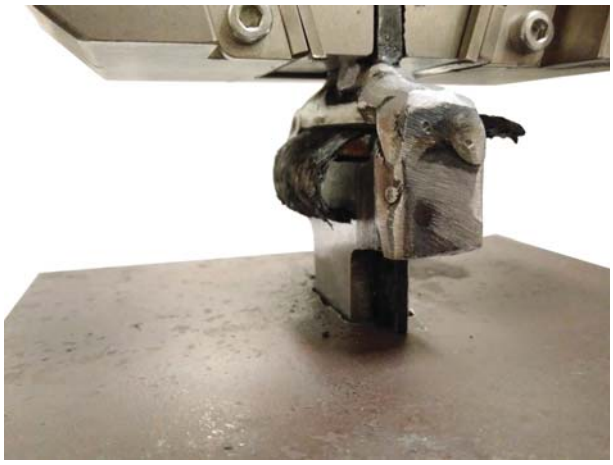

Figure 5.2: Crush Stress setup and specimen behaviour.

The stress versus displacement plots for each fibre orientation are presented in figure 5.3. Due to the high strength nature of this fibre, in contrast with the high modulus nature of the previous tests (section 4.2.3), some specimens had to be discarded due to problems such as cracks outside the crush front.

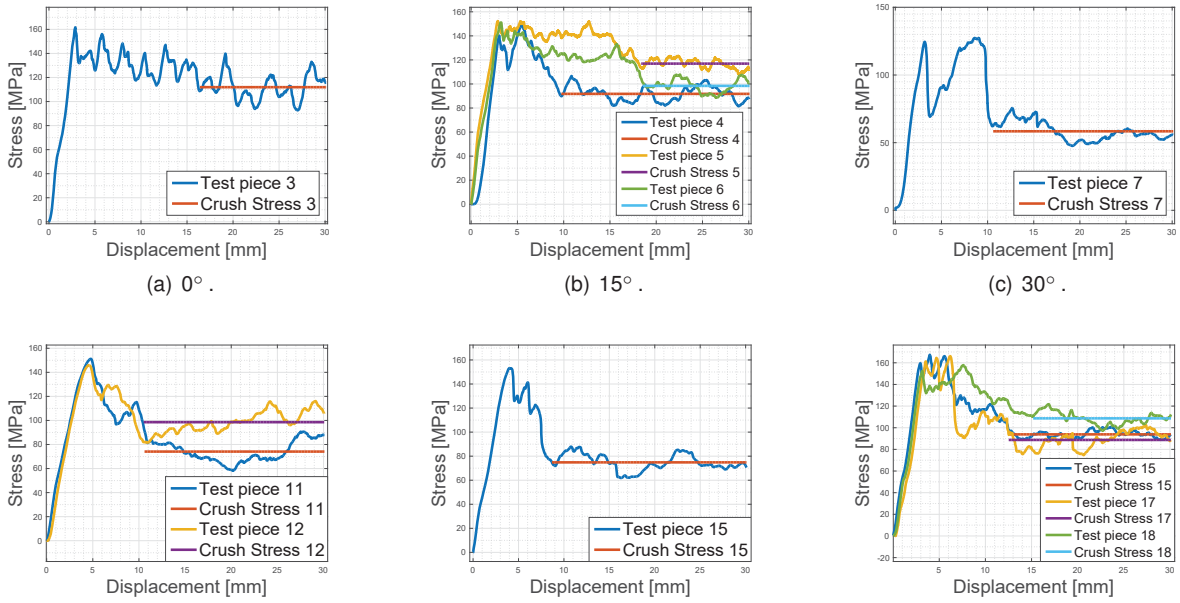

(a) 0° . (b) 15° . (c) 30° .

(d) 45° . (e) 60° . (f) 75° .

Figure 5.3: Final Crush Stress results.

For each orientation an average value was assumed. Also, it was presumed the 90° direction presented the same value as the 0° direction (due to the bi-directional pattern) and that each direction in the range 105° to 165° would have a correspondent direction in the range 15° to 75° . A similar procedure was followed for the third and fourth quadrant. In figure 5.4, a representation of the Crush Stress in each direction is presented, where the distance to the origin is the Crush Stress value for that particular direc-

tion and where the angle is between the direction of impact and the fibre direction. The lines correspond to the linear interpolation that Abaqus CZone [3] performs, if the angle between the direction of impact and the fibre direction is in-between two of the represented points.

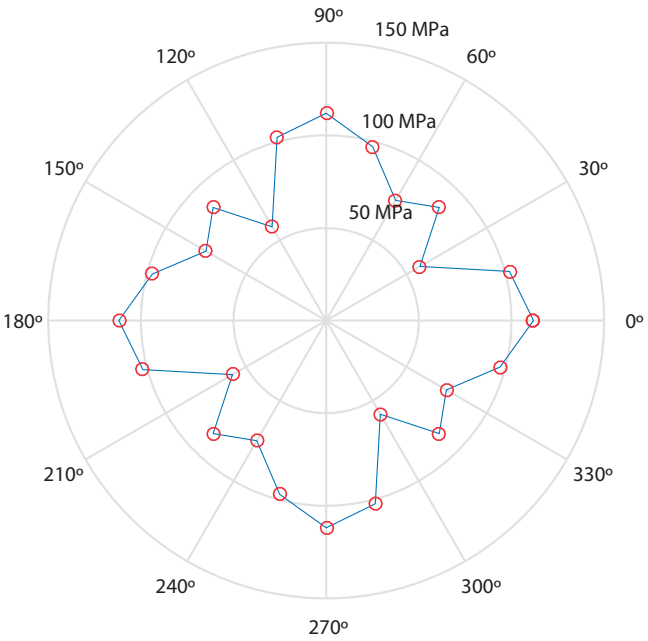

Figure 5.4: Crush Stress results summary.

5.2 Structural Nose

5.2.1 Numerical Model

In this section, a structural nose option will be studied and optimized. The main advantage of a structural nose is that it replaces the IA, meaning the nose itself must be able to absorb all the energy. However, as already stated in section 3.2 this completely changes the design process of the AIP as the loads short-cut directly to the FBH, which, in theory, would allow for a paper-thin AIP. The rules impose different experimental tests in these situations. Abaqus Explicit with the CZone [3] algorithm was used, similarly to what was done in section 4.2.2, with the big difference that the simulation will act as a prediction, instead of a validation.

In section 5.1, the Crush Stress values were predicted by experimental testing of small specimens. In table 5.1 further mechanical properties are presented. These were supplied by the Formula Student team - Projecto FST Novabase.

Table 5.1: Twill carbon fibre mechanical properties used.

Ex [GPa]	71.0	νxy	0.07
Ey [GPa]	71.0	Thickness [mm]	0.23
Gxy [GPa]	3.6		

The first challenge was to mesh the nose, which has a more complicated geometry than a simple tube. A structured mesh was possible only after multiple area divisions and not on the entire geometry (figure 5.5(a)). In figure 5.5(b), a 3mm mesh is created (details regarding this mesh can be found in table 5.2). Similarly to section 4.2.2, a rigid plate was created using four node rigid elements with a mass of 300 kg and assigned an initial velocity of $7m/s$. A contact pair was also established between these two parts, following the CZone [3] methodology. A fixed boundary condition was applied at lines at the bottom of the nose and at the bolt holes. These are meant to represent the rigid connection to the anti-intrusion plate. In order to reduce the computational effort, and allow for a later optimization, a symmetry condition was applied on the middle lines.

(a) The green areas correspond to structured mesh zones.

(b) A 3mm mesh example.

Figure 5.5: Structured mesh on the structural nose.

Table 5.2: Mesh details

Mesh Size	Type of element	Number of elements	Average aspect ratio	Maximum aspect ratio
3mm	4-node	16480	1.46	7.19
	3-node	33	1.25	1.5
5mm	4-node	5857	1.42	9.78
	3-node	27	1.35	1.8

The symmetry condition doesn't exactly represent reality due to possible transversal non-symmetrical motions or even longitudinal rotations of the middle nodes and thus induces error. However, in figure 5.6, an analysis to the influence of this approximation is made. The maximum difference between the two curves is only 3% but the computational time was reduced by 70%. In any case, after the optimization process, but before manufacturing, the final lay-up may be verified by a full analysis, without the symmetry condition, to make sure the final nose still complies with every requirement, despite the approximations made.

Similarly to section 4.2.2, a mesh sensitivity analysis was performed. In figure 5.7, the displacement versus time plot for element sizes ranging from 3mm to 20mm was performed. At 3mm, the displacement over time is identical to the 5mm curve, the mesh converged (details regarding the 5mm mesh can be found in table 5.2). The upper plate was modelled with 253 four node rigid shell elements with an aspect ratio of 1.

In figure 5.8, one can see an example of the frame results from the nose simulation. The crush mechanism is significantly more chaotic than seen in the carbon fibre tubes due to the complex geometry.

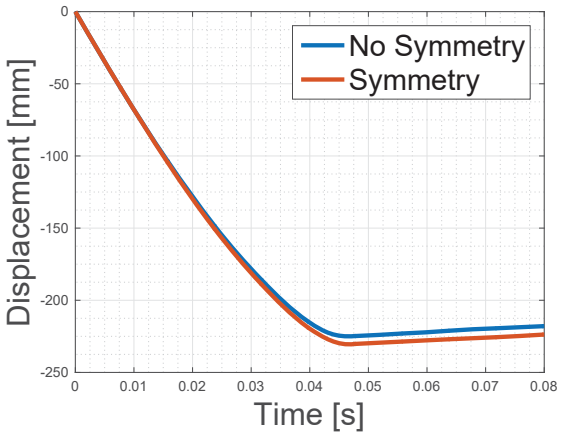

Figure 5.6: Influence of the symmetry condition applied.

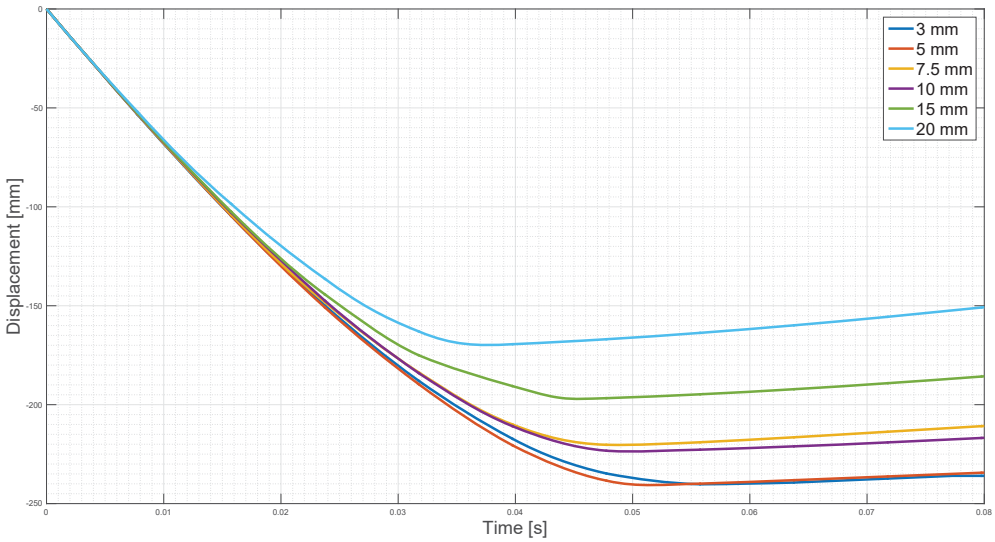

Figure 5.7: Mesh element size analysis.

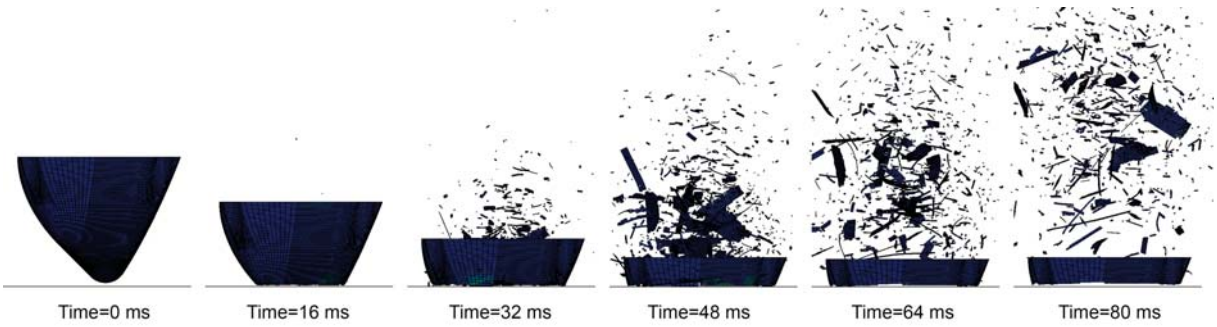

Figure 5.8: Structural nose frame results.

5.2.2 Coreless optimization

In figure 5.9, a representation of the simulation time, according to the mesh element size, is presented. The time was measured by running the simulations on one core, from an *i5 Intel* processor machine, without the symmetry condition applied. The simulation time each evaluation takes is critical for an

optimization process due to the, usually high, number of evaluations required for convergence. Efforts were made in order to reduce the time of each simulation to a feasible value.

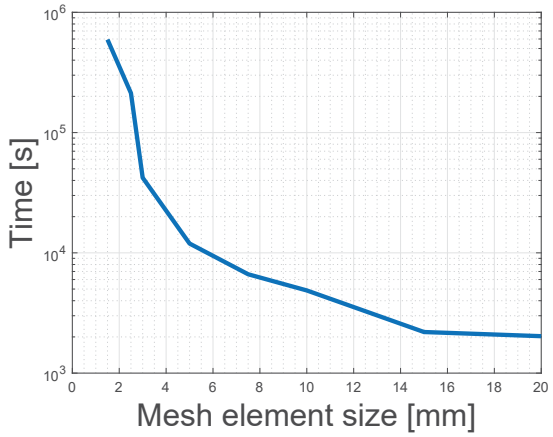

Figure 5.9: Simulation run time versus mesh element size.

Besides the symmetry condition imposed, which reduced the time by 70% (section 5.2.1), a 10 mm mesh was used, which reduced the time by 60%, the optimization was run on a much powerful i7 Intel processor, which reduced the time by 33% and, finally, an algorithm was created in order to reduce the need to run the entire impact time, which, in average, reduced the time by 50%.

A 10 mm mesh was used because, even though it was proven in section 5.2.1 that the mesh only converged at 5 mm, it was considered that the nondominated solutions remain nondominated regardless of the mesh used. This isn't true for solutions near the constraints, as a rough mesh might violate the constraints, and be excluded, and a fine mesh not. However, it isn't feasible to run an optimization process with such long duration evaluations. Still, after the optimization process finishes, the final solutions, if feasible, will be evaluated again with a proper mesh size.

Regarding the algorithm created, a flowchart is presented in figure 5.10 that shows the optimization process. The Abaqus [8] simulation doesn't run for the entire impact time (approximately 60 ms to 80 ms, depending on the lay-up) but for 10 ms periods. The constraints are verified after each 10 ms period and by using the velocity and position at the end of this period, one is capable of estimating an acceleration best-case scenario for the rest of the impact time. The acceleration best-case scenario is the curve that minimizes the maximum acceleration, which means that it must be constant. By being constant, one can use the uniform movement equations (equation (5.1)) to predict that constant value in order for the mass to decelerate before it hits the bottom of the nose. By considering d the distance from the plate to the end of the nose, v_0 the velocity of the plate at a particular instant (as seen in figure 5.11) and v as being zero, one can solve the equations (5.1a) and (5.1b) for a and obtain equation (5.1c). The latter equation is the one used to estimate the acceleration through the remaining time.

As this is a best-case scenario situation, if this acceleration doesn't respect the constraint then, certainly, the simulated acceleration won't and thus the point may be immediately disregarded. On the other hand, if the best-case scenario respects the constraints then it isn't possible to know if the simulated acceleration will or not, thus the simulation continues for another 10 ms. The restart analysis

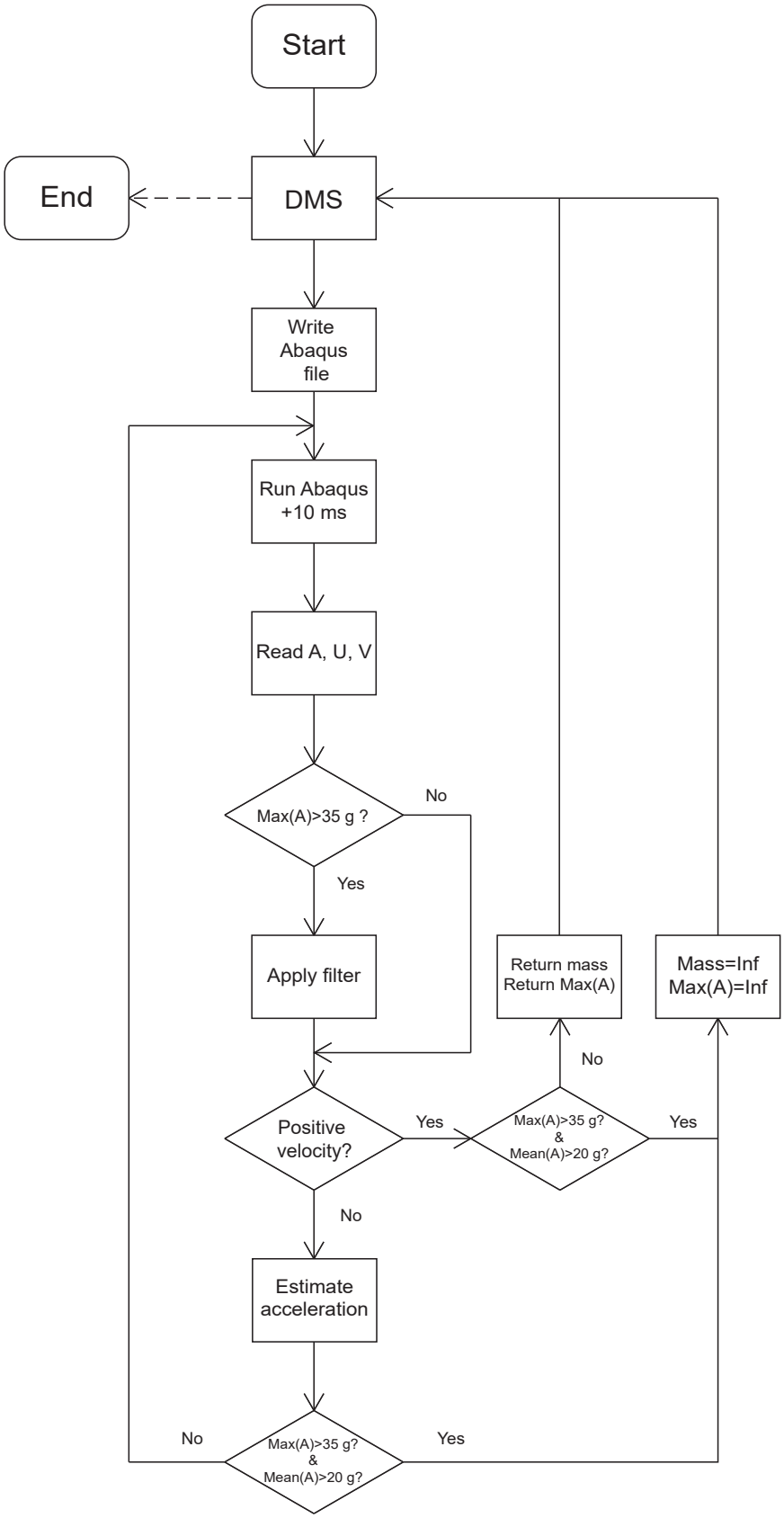

Figure 5.10: Estimation algorithm.

$$d = v_0 t + \frac{1}{2} a t^2 \tag{5.1a}$$

$$v = v_0 + at \tag{5.1b}$$

$$a = \frac{v_0^2}{2d} \tag{5.1c}$$

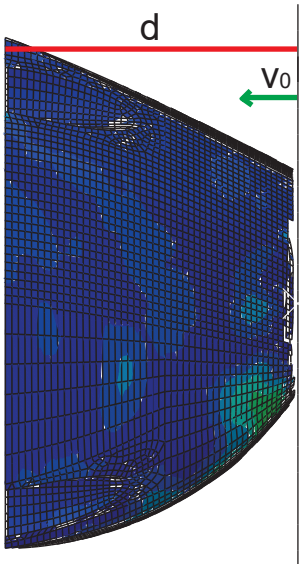

Figure 5.11: Representation of variables.

is made by re-running the simulation with the initial conditions equal to the final conditions of the previous 10 ms period. This method proved to be extremely efficient, reducing the simulation run time, in average, by 50 % and up to 80 % in some cases.

After the implementation of these measures, the optimization problem was defined. The MOO problem consists in finding the nondominated solutions that minimize, simultaneously, the mass of the nose (f_1) and the maximum acceleration (f_2) obtained throughout the impact ((5.2a)). The main objective in this optimization will be to reduce the weight. The minimization of the maximum acceleration will serve as a performance criteria, as a lower acceleration will result in a higher safety coefficient. (5.2c) is used to imposed the required acceleration constraints.

$$\min_{\boldsymbol{x} \in \Omega} \quad F(\boldsymbol{x}) \equiv (f_1(\boldsymbol{x}), f_2(\boldsymbol{x})) \tag{5.2a}$$

$$\begin{aligned} s.t. \quad & x_i \in \{4, 5, ..., 10\} \quad i = 1, ..., 7 \\ & x_i \in \{1024, 1025, ..., 2047\} \quad i = 8, ..., 14 \end{aligned} \tag{5.2b}$$

$$\begin{aligned} & max(A(\boldsymbol{x})) \leqslant 35g \\ & mean(A(\boldsymbol{x})) \leqslant 20g \end{aligned} \tag{5.2c}$$

The topological division of the nose was made considering the manufacturing process. A symmetrical lay-up assumption was made, which means the actual number of layers is twice the variables value. 14 discrete design variables were considered in (5.2b). The first seven variables regard the number of layers of each different zone (figure 5.12).

The remaining seven discrete variables, $x_8, ..., x_{14}$ represent the orientation of each set of layers previously determined by $x_1, ..., x_7$, respectively. The value of the orientation variables represents a vector that has a dimension equal to the corresponding number of layers variable value. The vector is extracted by a series of mathematical operations starting by a remained of the integer division by

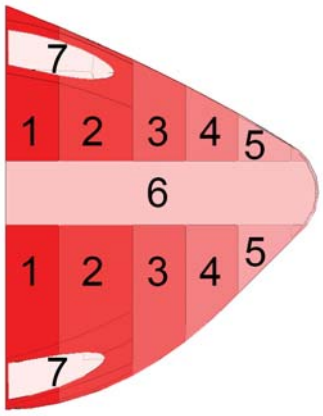

Figure 5.12: Different zones considered.

equation (5.3). Then, a list of permutations with repetitions (PWR) of all the possible orientations is performed, based on the corresponding number of layers variable value. Finaly, the orientations vector is extracted by selecting the corresponding permutation number.

$$PWR\ Number_i = ((x_{i+7}) mod\ (2^{x_i})) + 1, \quad i = 1, ..., 7 \tag{5.3}$$

Structural nose variable decoding example

To further clarify, if, for instance, $x_1 = 4$ and $x_8 = 1450$ the following procedure occurs:

- $x_1 = 4$ then zone 1 will have 4 symmetrical layers. A vector with dimension 4 is required for the orientation of those layers.
- The permutation number is computed. $PWR\ Number_1 = (1450) mod (2^4) + 1 = 11$.
- A list of all the possible orientation vectors for four layers with two possible values of each layer $\{0, 45\}$ is performed in table 5.3.
- The permutation number 11 is chosen, so the orientation vector will be 45, 0, 45, 0 and this will be the orientations of each layer of zone 1.

Table 5.3: Orientation vector permutations

PWR Number	Orientation Vector	PWR Number	Orientation Vector
1	[0,0,0,0]	9	[45,0,0,0]
2	[0,0,0,45]	10	[45,0,0,45]
3	[0,0,45,0]	11	[45,0,45,0]
4	[0,0,45,45]	12	[45,0,45,45]
5	[0,45,0,0]	13	[45,45,0,0]
6	[0,45,0,45]	14	[45,45,0,45]
7	[0,45,45,0]	15	[45,45,45,0]
8	[0,45,45,45]	16	[45,45,45,45]

After the definition, and implementation, of the optimization process described the results will now be analysed. In figure 5.13 all the points that complied with the constraints are represented. The red stars correspond to the nondominated solutions. The lightest option (solution 1), with 1.189 kg has a very high maximum acceleration of $332.8m/s^2$. Due to the proximity with the maximum allowed value of 350m/s^2 it isn't a viable solution, as an error of only 6% would cause the nose to be invalidated. The next solution can be found at 1.191 kg (solution 5), only 2 g heavier, but with a lower maximum acceleration of 296.6m/s^2. Then, at 1.225 kg (solution 4), 34 g heavier, a maximum acceleration of only 163.9m/s^2 is obtained.

Considering the possible errors involved in the simulation, a viable solution would probably be solution 4 (a complete description is presented in table 5.7), since it is only 3% heavier but has a maximum acceleration 50% lower than solution 1 (a complete description is presented in table 5.4) and 5 (a complete description is presented in table 5.8).

None of these solutions is actually lighter than the aluminium honeycomb option. Table 3.3 shows that the added weight from the current nose and IA is 730 g, which is 40% less than the optimized structural nose presented on this section.

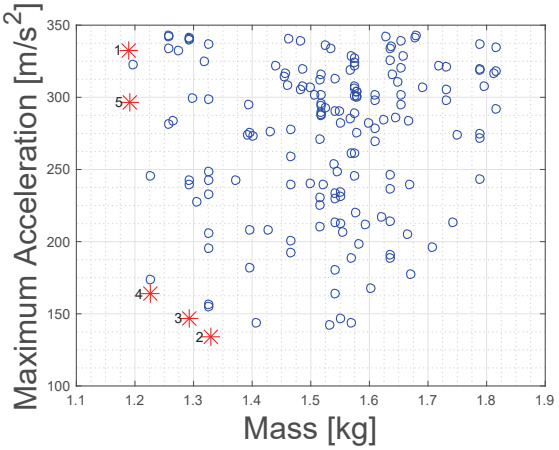

Figure 5.13: The nondominated solutions obtained from the optimization of a coreless structural nose is represented by the red stars.

In tables 5.5 and 5.6, a complete description of solutions 2 and 3 is presented, respectively. The imposed lower-bound value of variables x_1, x_2,...,x_7 was four, meaning the minimum number of layers on the different zones was eight, due to lay-up symmetry. Based on initial iterations, considering uniform thickness across the nose, it was observed that it tended to fail if less than 14 layers were used. In order to minimize the number of failed optimization iterations, and thus the computational effort, it was decided that a reasonable minimum number of layers would be eight per zone. Variables x_1, x_2, x_3, x_4 and x_7 did reach the minimum number imposed on at least one nondominated solution, meaning a lighter nose could eventually be reached by lowering this lower-bound at the cost of higher computational effort.

Table 5.4: Complete description of the solution 1 shown in figure 5.13. Due to lay-up simmetry only half the laminate is presented.

Solution 1 (Mass=1.189 kg; Maximum Acceleration=332.8 m/s^2)		
zone	Number of layers	Orientation vector
1	4	[45,45,45,0]
2	4	[0,45,0,0]
3	4	[45,0,45,0]
4	4	[0,45,45,0]
5	5	[0,0,0,45,0]
6	7	[0,0,0,45,0,45,45]
7	8	[45,0,0,0,45,0,45,45]

Table 5.5: Complete description of the solution 2 shown in figure 5.13. Due to lay-up simmetry only half the laminate is presented.

Solution 2 (Mass=1.329 kg; Maximum Acceleration=133.7 m/s^2)		
Zone	Number of layers	Orientation vector
1	4	[45,45,45,0]
2	4	[0,45,0,0]
3	4	[45,0,45,0]
4	7	[45,0,45,0,45,0,45]
5	9	[45,0,45,0,45,0,45,45,45]
6	5	[45,0,45,0,45]
7	8	[45,0,45,0,45,0,45,45]

Table 5.6: Complete description of the solution 3 shown in figure 5.13. Due to lay-up simmetry only half the laminate is presented.

Solution 3 (Mass=1.292 kg; Maximum Acceleration=146.8 m/s^2)		
Zone	Number of layers	Orientation vector
1	4	[45,0,45,0]
2	4	[45,0,45,0]
3	4	[45,0,45,0]
4	5	[45,0,45,0,45]
5	9	[45,0,45,0,45,0,0,45,45]
6	7	[45,0,45,0,45,0,0]
7	6	[45,0,45,0,45,0]

Table 5.7: Complete description of the solution 4 shown in figure 5.13. Due to lay-up simmetry only half the laminate is presented.

Solution 4 (Mass=1.225 kg; Maximum Acceleration=163.9 m/s^2)		
Zone	Number of layers	Orientation vector
1	4	[45,0,45,0]
2	4	[45,0,45,0]
3	4	[45,0,45,0]
4	5	[45,0,45,0,45]
5	9	[45,0,45,0,45,0,0,45,45]
6	5	[45,0,45,0,45]
7	6	[45,0,45,0,45,0]

Table 5.8: Complete description of the solution 5 shown in figure 5.13. Due to lay-up simmetry only half the laminate is presented.

Solution 5 (Mass=1.191 kg; Maximum Acceleration=296.6 m/s^2)		
Zone	Number of layers	Orientation vector
1	4	[45,0,45,0]
2	4	[45,0,45,0]
3	4	[45,0,45,0]
4	5	[45,0,45,0,45]
5	9	[45,0,45,0,45,0,45,45,45]
6	5	[45,0,45,0,45]
7	4	[45,0,45,0]

5.2.3 Core Optimization

In section 5.2.2, an optimization was performed on the lay-up of the structural nose assuming only carbon fibre was used. This caused the nose to have relatively low transversal stiffness, due to the high ratio between the nose length and its thickness, and thus creating a very high bending moment, causing it to fail catastrophically outside the crush front. This behaviour meant that only heavy solutions would comply with the constraints.

One way to add stiffness, while maintaining a low weight, is to allow the optimization process to include a core material. However, the inclusion of a core may arise problems during manufacturing due to the complex nose geometry.

To minimize this problem, a 3 mm thick core was selected from 3DCore [44]. This kind of closed cell core is composed of a series of connected hexagons (figure 5.14) which allow for adjustment to complex geometries. Besides, the gaps between the hexagons are expected to allow for a stable crush front to develop. It's expected that, when created, internal fractures propagate until an interface is reached. Furthermore, these gaps cause the core to have multiple weak regions that will crush progressively, as opposed to a plain sheet of core material that may fail catastrophically at its weakest point during an impact.

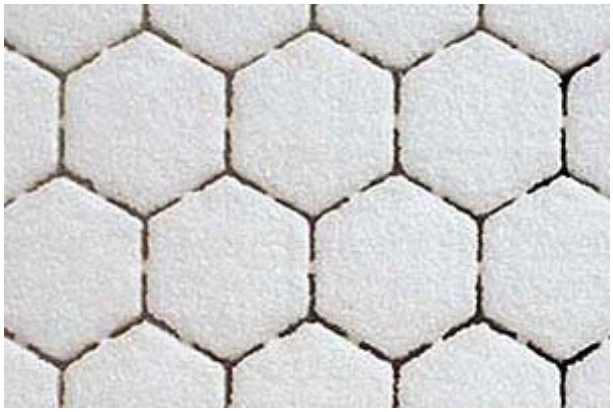

Figure 5.14: 3DCore [44] example. Picture taken from 3DCore website.

Similarly to section 5.2.2, an optimization problem was defined and solutions analysed. The objective functions, f_1 and f_2, and the acceleration constraints remain the same ((5.4a) and (5.4c)). However, the number and location of the zones has changed, as seen in figure 5.15. There are six variables representing the number of layers, ranging from one to seven layers, and six variables representing the orientations of each layer, ranging from 128 to 255. The transformation applied to the orientation variables is the same as in section 5.2.2.

$$\min_{\boldsymbol{x}\in\Omega} \quad F(\boldsymbol{x}) \equiv (f_1(\boldsymbol{x}), f_2(\boldsymbol{x})) \tag{5.4a}$$

$$\begin{aligned} s.t. \quad & x_i \in \{1,2,...,7\} \quad i = 1,...,6 \\ & x_i \in \{128,129,...,255\} \quad i = 7,...,12 \\ & x_i \in \{0,1,...,63\} \quad i = 13 \end{aligned} \tag{5.4b}$$

$$max(A(\boldsymbol{x})) \leqslant 35g$$
$$mean(A(\boldsymbol{x})) \leqslant 20g \tag{5.4c}$$

There's also a new variable to account for the possibility of a core. This new variable can take any integer from 0 to 63 and is then converted to a 6 bit binary base. Each topological zone is connected with a specific vector entry. If that entry has a value of 1 then a core is assumed in that zone, if 0 then no core is included.

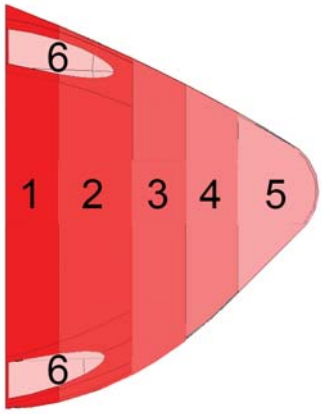

Figure 5.15: Different zones considered on the structural nose with core.

The same assumptions regarding the time saving strategies, explained in section 5.2.2, including the developed algorithm, are used.

In figure 5.16, all points, that complied with the constraints, are represented. The red stars correspond to the nondominated solutions. The lightest, nondominated, solution presented a mass of 392.5g, with a maximum acceleration of 168.4m/s^2, which is considerably lighter than the lightest coreless solution and still complies with the constraints with a reasonable safety margin. These results prove that the inclusion of a core can decrease the overall weight drastically by adding transversal stiffness through the increase of thickness and thus moment of inertia.

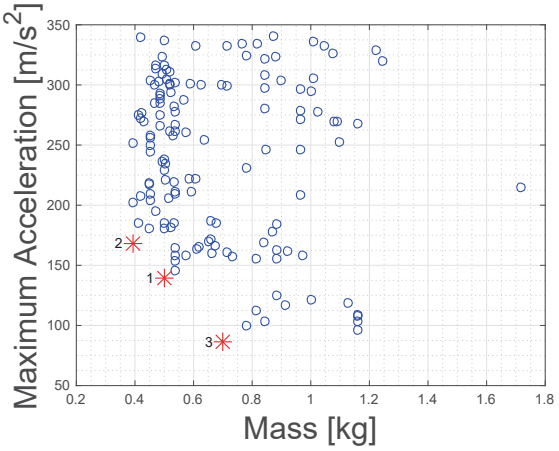

Figure 5.16: The red stars represent the nondominated solutions obtained from the optimization of the structural nose, with core.

In tables 5.9, 5.10 and 5.11 the vectors corresponding to the nondominated solutions are presented.

Table 5.9: Complete description of the solution 1 shown in figure 5.16. Due to lay-up simmetry only half the laminate is presented.

Solution 1 (Mass=0.499 kg; Maximum Acceleration=139.2 m/s^2)			
Zone	Number of layers	Orientation vector	Core
1	2	[0,0]	0
2	2	[0,0]	0
3	2	[0,0]	1
4	1	[0]	0
5	3	[0,0,0]	1
6	2	[0,0]	0

Table 5.10: Complete description of the solution 2 shown in figure 5.16. Due to lay-up simmetry only half the laminate is presented.

Solution 2 (Mass=0.393 kg; Maximum Acceleration=168.4 m/s^2)			
Zone	Number of layers	Orientation vector	Core
1	2	[45,0]	0
2	2	[45,0]	0
3	1	[45]	1
4	1	[45]	1
5	1	[45]	1
6	2	[45,0]	0

Table 5.11: Complete description of the solution 3 shown in figure 5.16. Due to lay-up simmetry only half the laminate is presented.

Solution 3 (Mass=0.701 kg; Maximum Acceleration=86.4 m/s^2)			
Zone	Number of layers	Orientation vector	Core
1	2	[45,45]	0
2	3	[45,45,45]	0
3	5	[45,45,45,0,0]	0
4	2	[45,45]	0
5	3	[45,45,45]	0
6	2	[45,45]	1

5.3 Crashbox

5.3.1 Numerical Model

Although the structural nose analysis and optimization proved that a lighter solution than the current aluminium honeycomb crashbox would be possible, a carbon fibre crashbox must yet be studied, before a final decision is made.

While the structural nose optimization originated from a fixed geometry, defined by the team, the carbon fibre crashbox doesn't have to. By the FSAE rules, inferior bounds to the crashbox size are imposed to the teams, namely 200 mm of length, 100 mm of width and 200 mm of height, and the crashbox must, obviously, fit inside the nose, thus establishing an upper bound to the size. Between

these two limits, the crashbox geometry is completely free to take any shape it can. For this reason, a similar optimization to section 5.2.2 was made, with additional geometric variables.

Due to manufacturing reasons, and because the minimum sized crashbox is a parallelepiped, it is reasonable to build an optimization program on the basis that a near-optimal, feasible, crashbox (less mass) will be an offset of the minimum sized crashbox. Besides, vertical and horizontal cross-section divisions within this offset were also allowed.

Similarly to what was done in section 4.2.2, the bottom nodes were constrained in all directions and an initial velocity of $7m/s$ was applied to the impacting wall. Similar contacts were also created.

5.3.2 Optimization

A Matlab [45] program was developed in order to create the different crashbox geometries according to the geometric design variables. A three dimensional matrix, with the size of a specific iteration's crashbox, was initialized and then populated with nodes at the corresponding sides. The mesh element size for each side was carefully chosen, in order to guarantee connection between the outer shell nodes and the inner division nodes. Four node shell elements were then created in each side. As the geometry was allowed to change, the number of elements changed accordingly and thus it could range from as low as 4800 and up to 5600, with an aspect ratio of one. Element sets were defined and the information wrote on a .inp file in Abaqus [8] format.

The estimation algorithm presented in section 5.2.2 was used again in order to reduce computational time.

An MOO problem was once again defined and the solutions analysed. The objective functions, as well as the acceleration constraints, remain the same ((5.5a) and (5.5c)) as in previous sections. However, the number of variables increased to 16 in order to account for the geometry (bounded as in (5.5b)).

Variables x_1, x_2 and x_3 represent the length, width and height of the crashbox (in millimetres). The variables x_4 and x_5 represent the number of internal cross-section divisions. To better illustrate the internal division possibilities, figure 5.17(a) presents a schematic of all possible combinations.

$$\min_{\boldsymbol{x}\in\Omega} \quad F(\boldsymbol{x}) \equiv (f_1(\boldsymbol{x}), f_2(\boldsymbol{x})) \tag{5.5a}$$

$$
\begin{aligned}
s.t. \quad & x_1 \in \{200, 205, ..., 400\} \\
& x_2 \in \{100, 105, ..., 300\} \\
& x_3 \in \{200, 205, ..., 400\} \\
& x_4 \in \{1, 2, ..., 5\} \\
& x_5 \in \{1, 2\} \\
& x_i \in \{1, 2, ..., 7\} \quad i = 6, ..., 9 \\
& x_j \in \{128, 129, ..., 255\} \quad j = 10, ..., 13 \\
& x_{14} \in \{1, 2, 3, 4\} \\
& x_k \in \{1, 2\} \quad k = 15, 16
\end{aligned} \tag{5.5b}
$$

$$
\begin{aligned}
& max(A(\boldsymbol{x})) \leqslant 35g \\
& mean(A(\boldsymbol{x})) \leqslant 20g
\end{aligned} \tag{5.5c}
$$

Variables x_6 until x_9 represent the number of layers on zones *a*, *b*, *c* and *d* in figure 5.17(b) while variables x_{10} up to x_{13} correspond to the orientation of those layers. The last three variables, x_{14}, x_{15} and x_{16} are core related variables. The first one indicates whether there is core on zones *a* and *b* while the other two relate to zones *c* and *d*, respectively. The core variables were split into three due to the possibility of zones 3 and 4 not existing, in the case either x_5 or x_4 are equal to one.

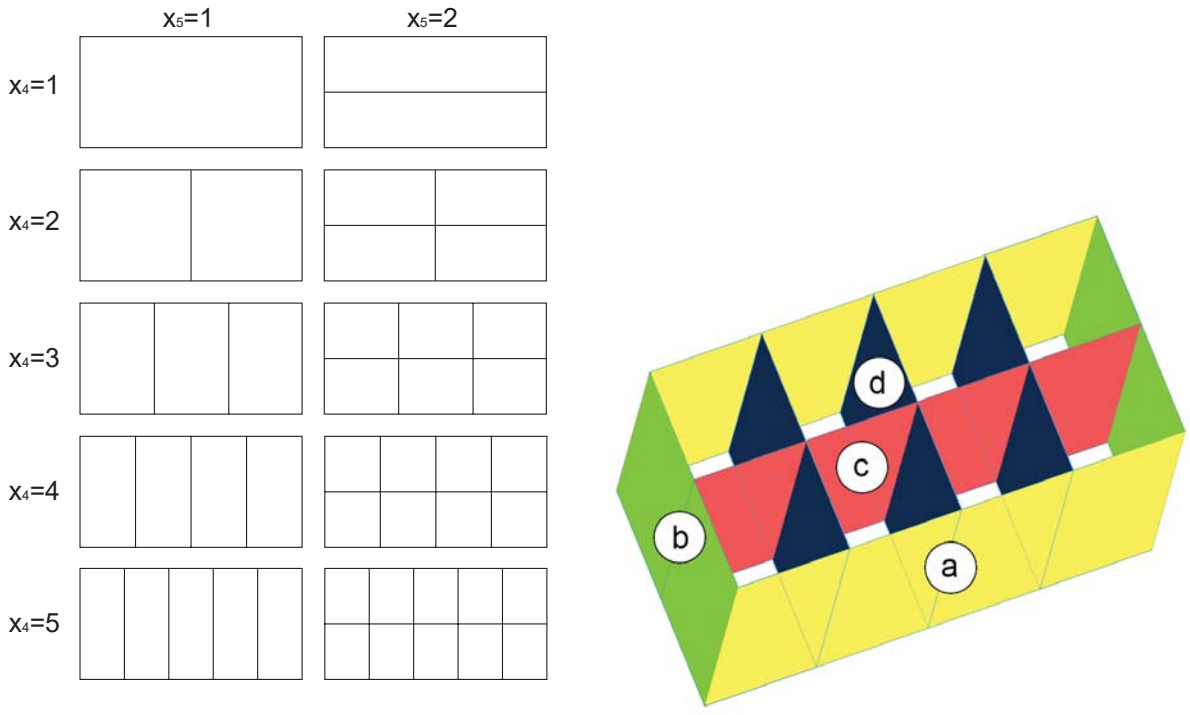

(a) Internal division possibilities.

(b) Carbon Fibre crashbox lay-up scheme.

Figure 5.17: Internal division possibilities and lay-up zones.

In figure 5.18, all the points that complied with the constraints imposed are represented. The non-dominated solutions are represented by the red stars. The lightest solution has 160.1 grams and reached

a maximum acceleration of 165.1m/s^2 (solution 2) while the other (solution 1) presented a weight of 288.1 grams and a maximum acceleration of 126.7m/s^2. Given the fact that the lighter solution still managed to achieve less than half the maximum acceleration imposed by the rules, it was considered to be a feasible solution.

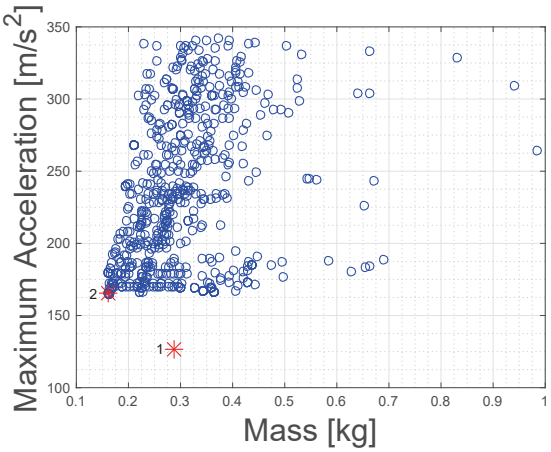

Figure 5.18: Pareto Front obtained from the Carbon Fibre crashbox optimization.

In tables 5.12 and 5.13, the vectors corresponding to the nondominated solutions are presented. Both nondominated solutions have an identical vector except for variables x_1, x_2 and x_3, meaning that the only difference between the two is the geometry.

Table 5.12: Complete description of the solution 1 shown in figure 5.18. Due to lay-up simmetry only half the laminate is presented.

Solution 1 (Mass=0.288 kg; Maximum Acceleration=126.7 m/s^2)			
Zone	Number of layers	Orientation vector	Core
a	1	[0]	0
b	2	[0,45]	1
c	-	-	-
d	-	-	-
Length [mm]	Width [mm]	Height [mm]	
395	135	285	

Table 5.13: Complete description of the solution 2 shown in figure 5.18. Due to lay-up simmetry only half the laminate is presented.

Solution 2 (Mass=0.160 kg; Maximum Acceleration=165.1 m/s^2)			
Zone	Number of layers	Orientation vector	Core
a	1	[0]	0
b	2	[0,45]	1
c	-	-	-
d	-	-	-
Length [mm]	Width [mm]	Height [mm]	
210	115	220	

After decoding the variables it is possible to obtain the optimized geometry and lay-up (figure 5.19). Note that, even though internal divisions were allowed, the optimal solution has none. The longitudinal direction is considered to be at 0° .

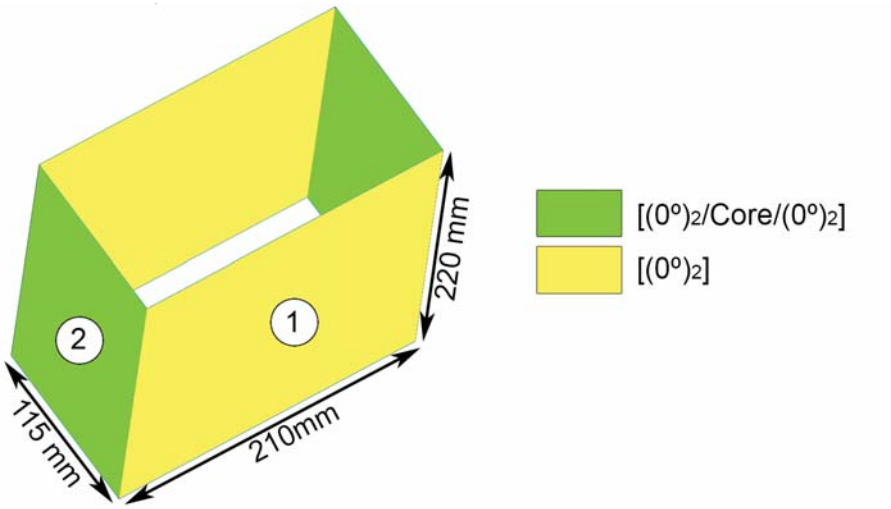

Figure 5.19: Geometry and lay-up of the optimized carbon fibre crashbox.

Through visual analysis of the failure mode presented in the simulation, it was concluded that the lateral walls (number 2 in figure 5.19) absorbed nearly all the energy, while the walls number 1 only held the others vertically. Due to the small thickness of wall number 1, it was feared that this might not happen due to possible manufacturing errors. Analysing again the nondominated solutions obtained (figure 5.18), the lay-up from the second solution was checked and it was verified that only the length, c, of the crashbox increased, not its lay-up. It was thus decided that a second, backup option, would be considered where the lay-up from the second wall was also applied on the first wall, ensuring an uniform energy absorption through the cross-section.

This second option ignores the optimization process in the sense that it isn't a nondominated solution. However, its purpose is to prevent an event where the optimization converged into a non-feasible solution, meaning that the structure would have to be perfect.

The optimization of the crashbox was performed without considering the AIP deformation in order to reduce the analysis complexity. However, a complete assembly analysis must still be made before testing. In figure 5.20, such a model is presented. New contacts were created between the IA and the AIP and between the AIP and the FBH, similarly to chapter 3. A symmetry condition was also imposed. The AIP and IA were meshed with 5921 four node shell elements, with an average aspect ratio of 1.27 out of which 11 had a aspect ratio above 7, with the worst being 13. The FBH was meshed with 2120 elements with an average aspect ratio of 2.55, although 7.5% of the total elements had an aspect ratio worse than 7. The small radius inner fillet of the FBH, that wasn't previously considered, explains the excess of badly shaped elements.

Each simulation run of this analysis took several hours to conclude and thus an optimization wouldn't be feasible. Instead, the AIP lay-up orientation was defined at 0° and the number of layers was iterated until no significant change to the IA behaviour was observed. The AIP lay-up was thus defined as $[(0^\circ)_7/Core/(0^\circ)_7]$. Aluminium inserts were also used due to the bolt's preload.

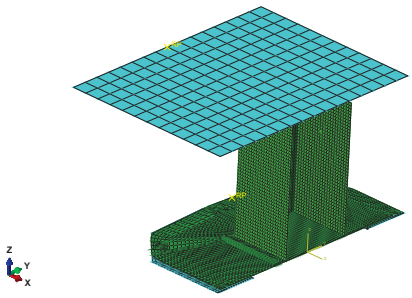

Figure 5.20: Optimized crashbox assembly model.

5.3.3 Alternative crashbox - Numerical Model

An alternative design composed only of carbon fibre, without core, was also carried out. Inspired by the successful tests presented on section 4.2.1, a simple, yet efficient, design was proposed.

In figure 4.22, one can see the maximum and mean accelerations were respected, which means the only reason the tube can't serve as an impact attenuator is due to the minimum dimensions imposed by the rules.

This alternative design stretches the rules by designing a box-shaped structure around the tube (figure 5.21). This way, the tube would still be the primary absorbing energy system but would also be compliant with the minimum dimensions rule. Even though this is a risky design, as it may be disregarded by the competition as going against the intent of the rule, it was investigated nonetheless.

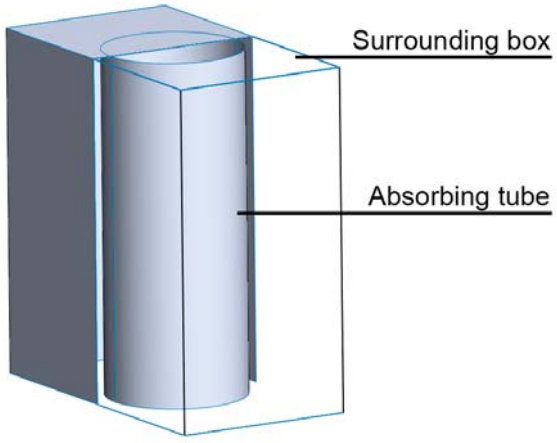

Figure 5.21: Alternative design scheme.

A very similar analysis to section 5.2.1 was performed. The bottom lines were fixed in all directions and a contact between the impacting wall and the crashbox was established. All elements are four node shells.

Due to severe time constraints, no optimization was carried out on this specific design.

A similar lay-up to the tubes tested in section 4.2.1 was defined. The geometry used was also very similar, with 90 mm of diameter and a slightly smaller lenght of 220 mm due to packaging constraints. In figure 5.22, the frame results of the Abaqus CZone [3] simulation are presented. As one can see a stable crush front was once again achieved. As a first approach, only the tube was simulated to allow

for quick lay-up iterations until it could absorb the required energy.

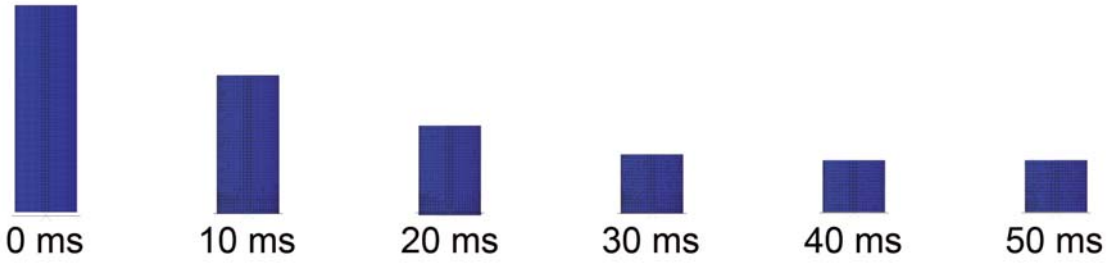

Figure 5.22: Frames results from the alternative design simulation.

This option would allow for a total IA weight of 275 grams (including the surrounding box), a reduction of 36% relatively to the aluminium honeycomb solution.

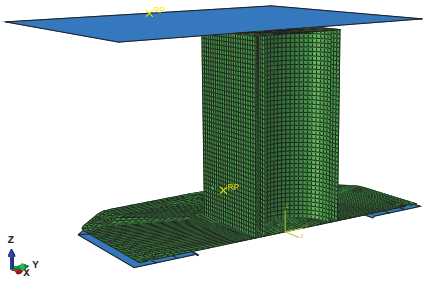

Figure 5.23: Alternative crashbox assembly numerical model.

Once again an assembly analysis was performed (figure 5.23), including the AIP and the surrounding box. In total 10445 linear shell elements were created, out of which 28 were triangles. On the tube, the AIP and the surrounding box there were 9 elements with an aspect ration greater than 7 (0.11%), with the average being 1.27. On the barrier a total of 160 elements presented an aspect ratio greater than 7, explained by the short fillet on the inner edge, and an average aspect ratio of 2.55.

The carbon fibre supplied by the team to produce the AIP designed on this section differs from the previously used material. TeXtreme (commercial name) spread tow dry carbon fibre is used with plain woven dry carbon fibre and a wet-layup epoxy resin, which implies that the manufacturing process changes relatively to the previous sections.

The plain carbon fibre properties used were supplied by the team and were obtained through tension tests equipped, with strain gauges (table 5.14). The TeXtreme properties on the other hand were found on the work of Music and Widroth [46] and weren't tested with the actual epoxy resin used due to its fibre pattern, which complicates the experimental tests.

Table 5.14: Plain woven dry carbon fibre mechanical properties used.

E_x [GPa]	E_y [GPa]	G_{xy} [GPa]	ν_{xy}	Thickness [mm]
55.0	55.0	1.2	0.08	0.2

Similarly to section 5.3.2 the AIP lay-up was iterated until no significant difference to the IA behaviour was observed. The lay-up orientation was defined at 0° and a core was assumed to exist only on the

red zone in figure 5.24, in order to reduce the total displacement, while the green centre was reinforced with more layers of carbon fibre to ensure the AIP didn't fail due to the more concentrated loads (when compared to the solutions presented in section 5.3.2). Due to the tube geometry and uncertainty related with the TeXtreme carbon fibre the AIP designed on this section is 21% heavier than the AIP of section 5.3.2. Aluminium inserts were used once again due to the bolt's preload.

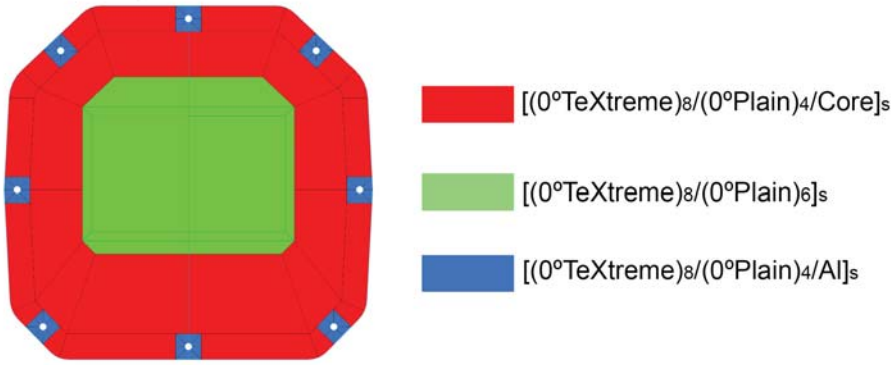

Figure 5.24: CFRP AIP.

5.4 Possible solutions comparison

After the different analysis and optimizations of the previous sections, a decision must be made regarding the components to be manufactured and tested. In table 5.15, the weights are compared with the current solution and a decision table is presented.

The six different options are organized from best (highest score) to worst (lowest score) in three different categories. The material required was considered to be worth 50% more than the other two, due to the team's limitation on supplying high amounts of carbon fibre. Note that, even though the weight of the structural nose with core is lower than the alternative design, the former actually requires more raw material. The layers shape in the nose are not regular, causing much more waste to be created. Besides, the AIP associated with the structural nose would also require much more material, due to the mandatory additional tests, its weight is also an estimative based on the design of Browne [21]. The complexity category refers, not only to the manufacturing difficulty, but also to the numerical model required to predict a correct behaviour, which is mainly associated with its geometric complexity. The third category sorts the different options by the weight saved when compared with the current solution.

Table 5.15: Solutions comparison and decision table. Higher is better.

						Decision Table			
	AIP [g]	IA [g]	Nose [g]	Total [g]	Difference [%]	Material Required (a)	Complexity (b)	Weight (c)	Total $(1.5a+b+c)$
FST06e	1711	430	700	2841	+24.39%	-	-	-	-
FST07e	1554	430	300	2284	-	-	-	-	-
Structural Nose Coreless	800	-	1225	2025	-11.34%	1	2	1	4.5
Structural Nose Core	800	-	393	1193	-47.77%	2	1	5	9
Crashbox 1	800	151	300	1251	-45.23%	5	5	4	16.5
Crashbox 2	800	262	300	1362	-40.37%	4	5	3	14
Alternative design	1015	286	300	1601	-29.90%	3	3	2	9.5

The three best solutions found were the two CFRP crashboxes and the alternative design.

Chapter 6

IA Experimental Results

In section 5.3, the crashbox was analysed and optimized. The options were reviewed and a final decision as to which solutions should be manufactured was made in section 5.4.

In figures 6.1(a) and 6.1(b), the manufactured IAs are presented. Every component except for the surrounding box of the alternative design, and its AIP, were manufactured using pre-impregnated fibre followed by an autoclave cure. The surrounding box and its AIP were manufactured through a wet-layup process.

(a) Manufactured crashboxes while being glued to the AIP.

(b) Alternative design ready to be glued to the AIP.

Figure 6.1: Crashboxes and alternative design manufacturing.

6.1 CFRP Crashbox

The first crashbox to be tested was the optimal result retrieved from the Pareto Front on section 5.3. The experimental setup used was similar to the tubes tested in section 4.2.1. However, a problem related with the camera trigger caused the impact frame images to be lost. Nevertheless, the accelerometers were able to register the event.

In figure 6.2(a), the raw data from the three accelerometers used is presented. Similarly to section 4.2.1, data above 40g is present so a low-pass filter may be applied (figure 6.2(b)). In figure 6.2(c), the

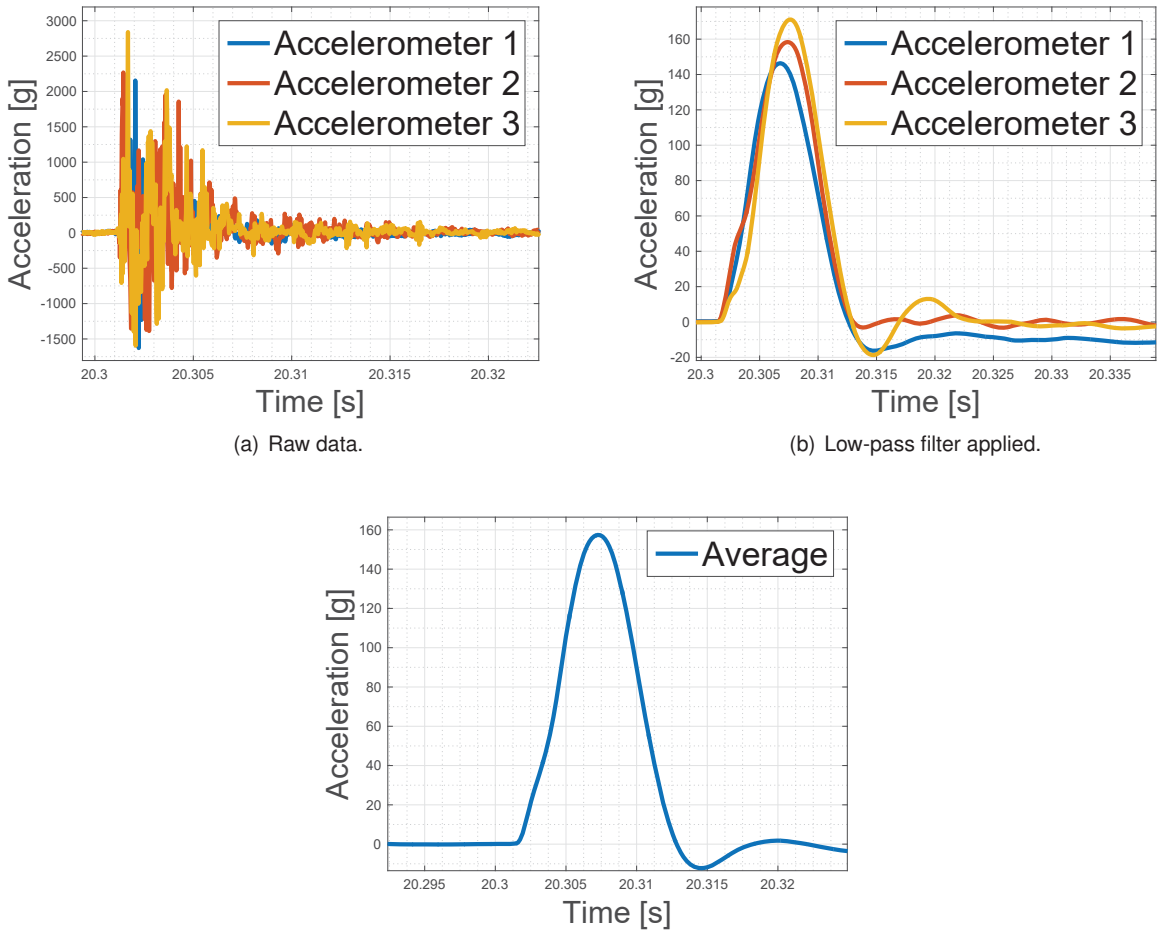

(a) Raw data.

(b) Low-pass filter applied.

(c) Average performed to the three accelerometers.

Figure 6.2: Acceleration results from the first CFRP crashbox tested.

average of the accelerometers is performed. However, peaks above the 40*g* limit are still visible, which means the design has failed.

The impact test of the second crashbox followed. As mentioned in section 5.3.2, the geometry of the second crashbox is identical to the first but with a different lay-up. The high-speed camera was once again used and set at 8000 fps. During the test a problem with the data acquisition system caused the acceleration curves to be lost. However, it was clear that, similarly to the previous test, this design would also fail. From the camera's frames (figure 6.3), it was possible to calculate the impact duration as 271 frames at 8000 fps meant an impact time of 33.9 ms. The initial velocity of the weight was 7m/s, which means that the mean acceleration during the impact was 21*g*, which is higher than the 20*g* allowed.

By looking at the high-speed frames and the debris left by the impact, an explanation to these two failures is proposed. The first milliseconds of impact caused the core to be sheared all the way from top to bottom, splitting both carbon fibre layers apart. This effect in turn caused the walls to loose their transversal stiffnes and thus bend and fail into large chunks without absorbing energy.

This failure mode wasn't predicted by the numerical model developed on the previous sections. In fact, this failure mode can't be predicted by shell elements, as it isn't possible for a shell to split into two. The only way to mimic this behaviour through a numerical model would be to model the inner

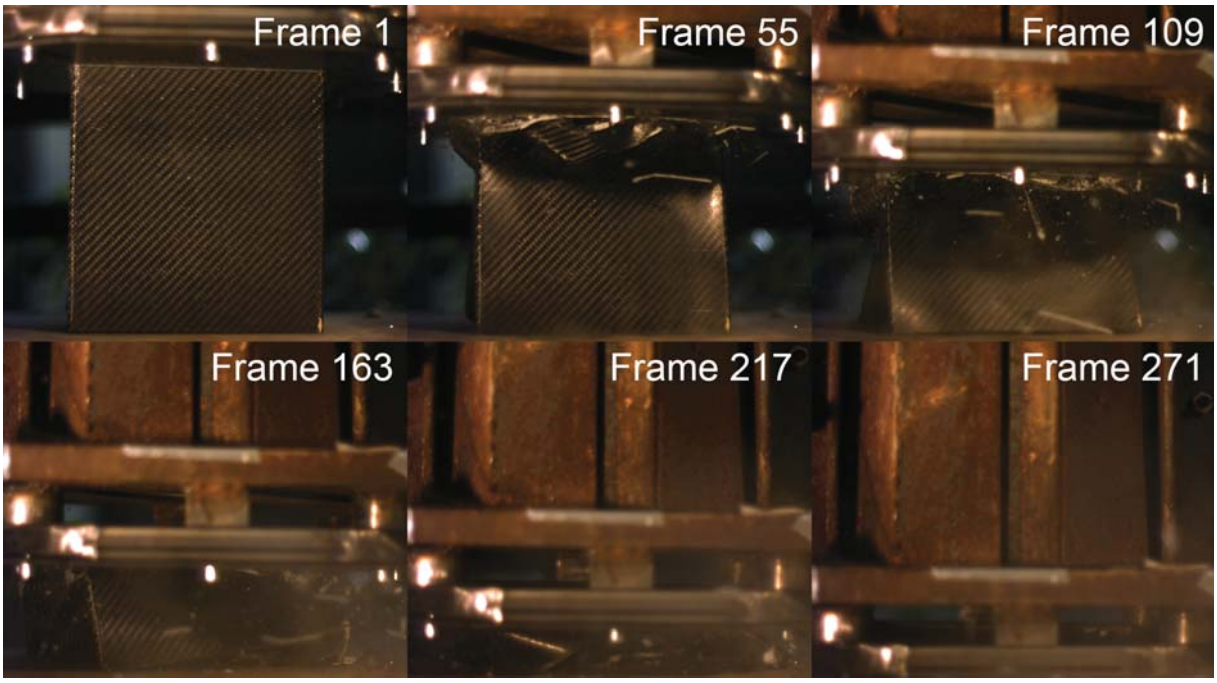

Figure 6.3: Frame results from the high-speed camera.

layer using a shell element, the core with a solid element and another shell element for the outer layer. The problem in doing so, besides the triple increase in elements, are the contacts definition between the shell elements and the solid elements. This connection couldn't be modelled using a rigid contact, because it wouldn't be able to represent interface failure, even though it would be able to represent elastic behaviour correctly. The problem of this explicit approach is the difficulty in experimentally finding the interface properties.

Note also that, even with an accurate numerical model, the added stiffness the core provided was what made this kind of solution work in the first place. Otherwise it would have been heavier than the aluminium honeycomb solution.

This kind of catastrophic failure (as opposed to a progressive failure) was feared from the moment a core was allowed on the layup. The selection of the 3DCore [44] was primarily based on the fact that the core is discontinuous, in the hope that this internal structure would be enough to promote a stable crush front, as explained in section 5.2.3. The use of positive pressure during the autoclave cure also caused the core thickness to permanently decrease by 0.72 mm, which added to the homogenization of the core, which might have contributed to the failure observed.

6.2 CFRP Alternative Design

The alternative design was also tested with a similar setup to the previous tests (figure 6.4), except for the high-speed camera which wasn't available.

Once again, the accelerometers were able to capture the impact and register its accelerations. In figure 6.5(a), the raw data presents peaks higher than the 40g limit so a low-pass filter is applied (figure 6.5(b)). A different offset is verified between the three curves, so a high-pass filter must also be applied

Figure 6.4: Alternative design test setup.

(figure 6.5(c)). Finally, an average is performed to the three curves achieving the acceleration of the CG (figure 6.5(d)).

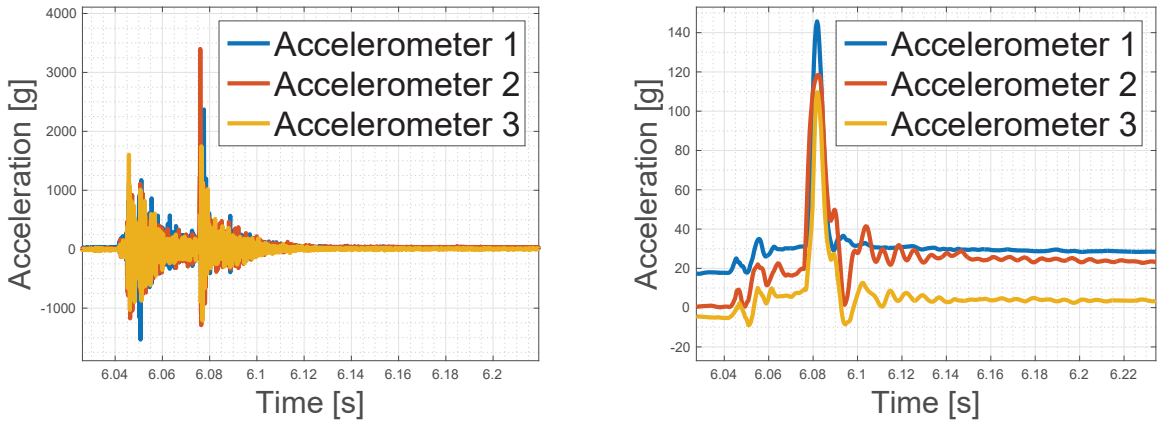

(a) Raw data.

(b) Low-pass filter applied.

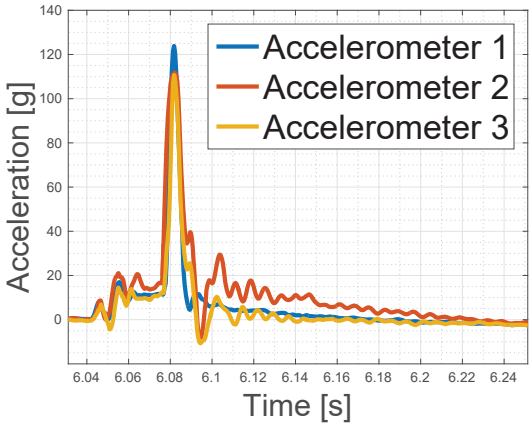

(c) High-pass filter applied.

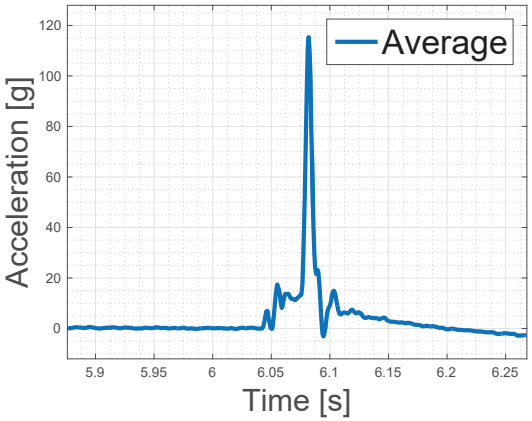

(d) Average performed to the three accelerometers.

Figure 6.5: Acceleration results from the alternative crashbox test.

However, it is clear that a peak over the 40 *g* limit is present on the data. This means the alternative design also failed to comply with the rules. By analysing the debris (figure 6.6(a)), it was concluded that

the tube was able to cut through the AIP. Figure 6.5(d) also shows that for the first 25 ms a controlled failure was achieved. However, as soon as the AIP failed a high peak was observed from the impact of the weight on the steel barrier. In figure 6.6(b) a detailed view of the failed AIP centre is presented, its shape indicates the shear forces developed were high enough to cause an almost perfect circle to be punctured. Signs of delamination on the FBH side were also identified.

(a) View from behind the FBH.

(b) Detail of the failed AIP centre.

Figure 6.6: Alternative design post impact.

The reason for this particular failure wasn't fully understood. Neither the numerical model presented in section 5.3.3 nor simple analytical calculations were able to predict such a failure. Even if one considers the force applied only in the inner diameter of 90 mm, the total resistive area is of 1555mm^2 due to the 5.5 mm of carbon fibre in that section. Calculating the load, by multiplying the 300kg per the 20*g*, seen on the accelerometer curve before failure, one gets 58860N which corresponds to a stress of 38MPa, which is a considerable low value when compared with the maximum shear stress properties.

One factor that must not be overlooked is the manufacturing process itself, since this component was made by a wet-layup process, which is highly dependant upon the workman. If interior portions of the AIP were already weakened due to a manufacturing error then the failure observed might be its result.

Another factor that was not considered during the design phase is the possibility of an off-axis impact, which might have caused an overload on a smaller section causing a local failure that then propagated through the AIP. This possibility was previously neglected due to the gap between the steel weight and the vertical beam guide. This gap could, theoretically, straighten the weight, even when it hit the barrier at a small off-axis inclination, as soon as the first impact occurs due to the moment created around the CG.

Chapter 7

Enhanced Solution

7.1 CFRP AIP - Numerical Model

In section 3.2, it was stated that the optimization of the AIP is strongly related to the IA, as different IA geometries and materials would result in distinct loads. This was the main reason behind the developments of chapters 4 and 5, to optimize the IA with the AIP, or at least the IA and then the AIP (accordingly to the computational power available).

However, chapter 6 proved that a lighter IA would not be possible, at least with the assumptions made regarding geometry and material. Thus, and considering the severe time constraints, and resources limitations, that formula student teams face, the only viable option left would be to maintain the IA and to design a carbon fibre AIP capable of reducing the overall weight.

Altair software with the Radioss [40] explicit solver was used once again to model the honeycomb crashbox, similarly to chapter 3.

A four node orthotropic shell, with a sandwich property, was used to model the AIP. It was verified that a lay-up similar to the one used in the AIP of section 5.3.3 would be sufficient to withstand the load. Moreover, with the aluminium honeycomb crashbox the AIP provides a resistive shear cross-section area of 3300 mm^2, which considerably reduces the risk of another failure by punching.

In figure 7.1, the frame results of the impact are presented. Similarly to chapter 3, the aluminium honeycomb crashbox fails in a progressive and stable mode. Its also observed that the AIP does not fail and that its maximum permanent displacement is rules compliant.

This solution could be further improved by a lay-up optimization process similar to chapter 5, this was not done due to the high computational effort required and the tight schedule that the team faced.

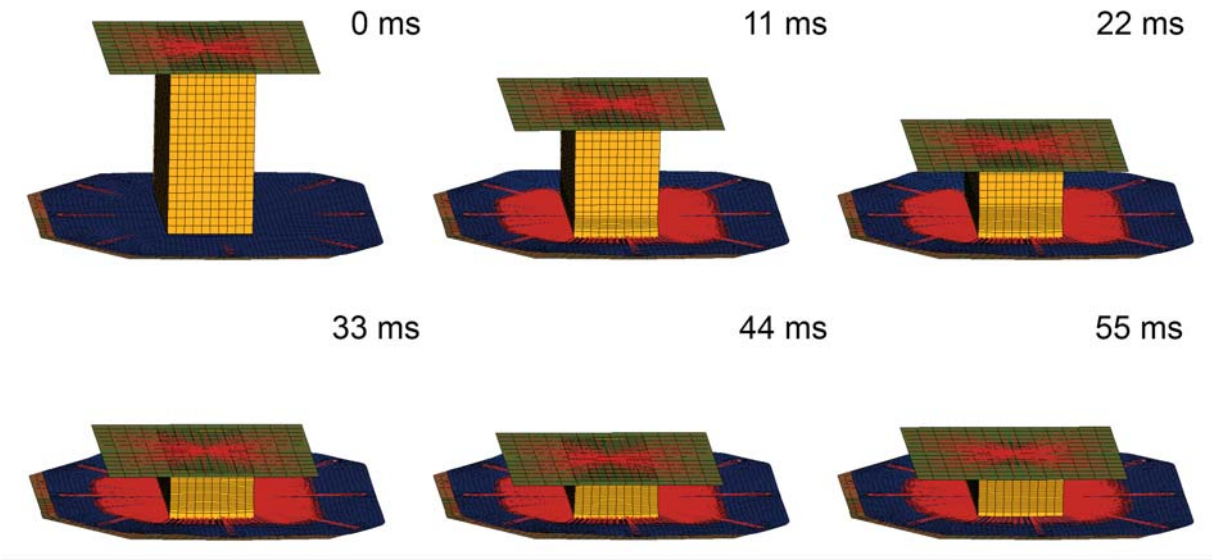

Figure 7.1: Frame results of the CFRP AIP with the aluminium honeycomb crashbox.

7.2 CFRP AIP - Experimental Results

The AIP studied in section 7.1 was manufactured through a wet-layup process and the honeycomb crashbox was glued to it using an epoxy structural glue. The test setup used was similar to previous sections with the accelerometer glued to the steel weight in order to register the impact.

In figure 7.2(a), one can see the raw data obtained from the accelerometers through the data acquisition system. As one can easily see, peaks over the 40*g* limit are present. A low-pass filter had to be employed.

In figure 7.2(b), a third order low-pass Butterworth filter with a cut-off frequency of 100Hz was applied. The maximum acceleration variation is now inferior to the 40*g* limit, however the DC component must be removed.

In figure 7.2(c), a second order high-pass Butterworth filter with a cut-off frequency of 0.75Hz was applied.

Finally, a detailed view of the first impact is presented in figure 7.2(d). As one can see, the maximum acceleration is less than the 40*g* limit (21.2*g*) and the average acceleration is also less than 20*g* (14.6*g*).

In order to compute the total energy absorbed, one must first obtain the velocity and force acting on the 300 kg weight. Then, by multiplying them one achieves the power being dissipated over time which can be integrated to obtain the energy absorbed over time.

Thus, the final filtered data was integrated to obtain the velocity over time (figure 7.3(a)). Then, the acceleration (in m/s^2) was multiplied by 300 to obtain force. By multiplying the velocity and force, the power over time was achieved (figure 7.3(b)). Finally, the power was integrated to obtain energy (figure 7.3(c)).

From the energy plot analysis it's possible to conclude that the energy absorbed is 7779J, which is higher than required.

According to the rules the AIP maximum permanent deflection is of 25.4mm. In figure 7.4(a), it's

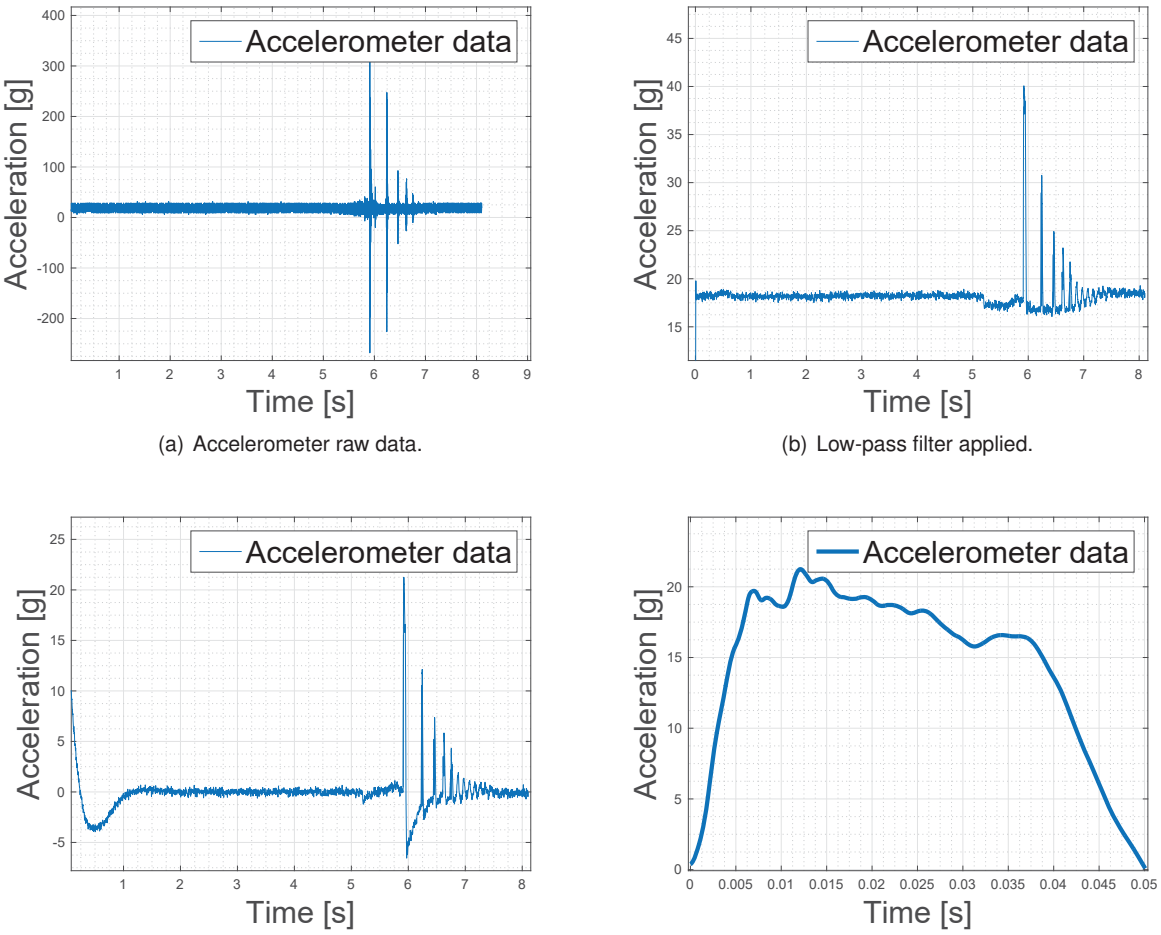

(a) Accelerometer raw data.

(b) Low-pass filter applied.

(c) High-pass filter applied.

(d) Detail of the first impact.

Figure 7.2: Accelerometer data analysis.

possible to see the AIP and IA assembly before the test. In figure 7.4(b), a picture of the same assembly after the test is presented. Here it's possible to see that the maximum permanent deflection is only 6mm.

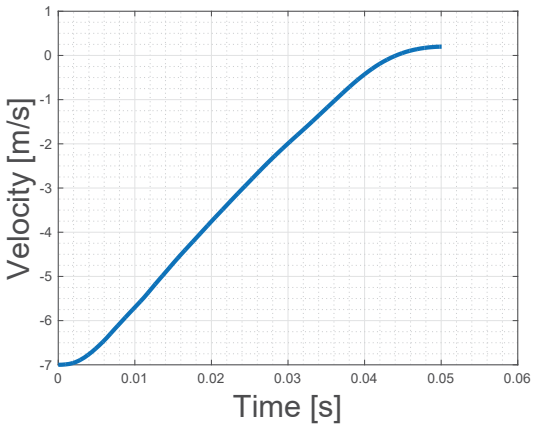

(a) Velocity over time.

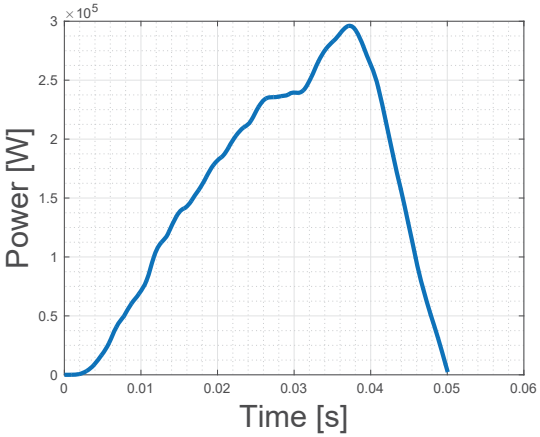

(b) Power over time.

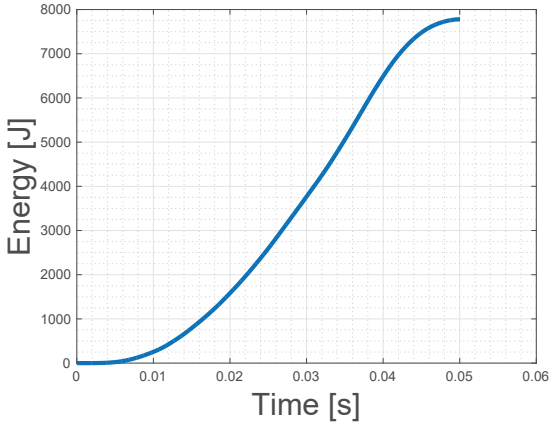

(c) Energy over time.

Figure 7.3: Calculations to obtain energy absorbed.

(a) Before the test.

(b) After the test.

Figure 7.4: Before and after test comparison.

Chapter 8

Conclusions

8.1 Achievements

The current solution used by the Formula Student team of the University of Lisbon was analysed for the first time and the obtained numerical results, using a finite element commercial software, of acceleration, displacement and crush mechanism were compared with the experimental data. An error of 10 % regarding the maximum acceleration and 3 % regarding the mean acceleration was achieved. The same model was successfully used to ensure a similar solution would still comply with the rules on the new car, the FST07e.

Preliminary tests were done using aluminium and carbon fibre tubes. Numerical models for both materials were developed and correlated with experimental data. A maximum error of 3.5% and 5% was obtained for the two aluminium tubes tested while, for the carbon fibre tubes, the unknown crush stress parameter was iterated until a fit to the experimental data was achieved. Material characterisation tests were performed on aluminium rods. A simple image tracking algorithm was developed and implemented, successfully retrieving displacement over time plots using the frames of an high-speed camera.

Quasi-static physical tests were developed in order to determine the crush stress property of the laminate used, where a 23.6% lower value was achieved when compared with the experimental data fit. Unaccounted dynamic effects might explain the error obtained. Nevertheless this method proved to be a very simple and quick way of assessing the crush stress value of carbon fibre laminates.

Based on the carbon fibre numerical model developed, several IA solutions were proposed and analysed. Multiple optimization problems were defined and a very efficient time-saving algorithm was implemented in order to reduce the overall run time to a feasible scale. Even after an optimization process, a coreless structural nose proved to be too heavy (when compared with the current solution). A core was thus allowed to exist and a new optimization process began, effectively reducing the nose weight by 68%. A carbon fibre crashbox was also optimized with respect to its lay-up and geometry which resulted in an IAA weight close to the structural nose (58 grams more). Later, an alternative design was also proposed based on the performance of the previously tested carbon fibre tubes.

The different options were compared and selected through a decision table that included the mate-

rial required, the complexity of the solution and its weight. Two different crashboxes and the alternative crashbox design were thus selected, manufactured and tested. The IA tests showed flaws in the model regarding the modelling of the core used, namely the single-shell simplification, in impact events. Manufacturing errors related to highly user-dependant processes weren't excluded as they might have caused premature failure.

It was concluded that a single-shell (through thickness) numerical model wasn't able to correctly represent the behaviour observed due to the impossibility for a shell to split into two. Only by adding several shell, or solid, elements through the thickness may this mode of failure be predicted. However, this implies that extensive experimental tests and model tuning needs to be performed in order to extract non-trivial contact properties between the elements. Besides, the inclusion of a core was allowed due to the excessive weight of the solutions being found, which means that a lighter solution than the current IA might not even exist, when considering the geometries studied through this work.

Nevertheless, a lighter, rules-compliant, solution was proposed, manufactured and tested. By changing the AIP material to a composite sandwich a weight reduction of 500g (22%), when compared with the current solution, was achieved.

8.2 Future Work

This work established a basis on which many future improvements may be applied, such as the following:

- A better test method to obtain the crush stress property of different laminates may be achieved by, for instance, developing a stiffer, more adjustable and higher speed test jig. This improvement may be able to more accurately predict the crush stress at different angles and different strain rates.
- A more complex numerical model, by representing the sandwich laminate with multiple shell and solid elements through the thickness would definitely result in a more accurate prediction. Even though the optimization process would probably have to be changed due to the much higher computational effort.
- Exploring different geometries though some sort of topological optimization could vastly improve the solutions obtained.

Bibliography

[1] N. Jones and T. Wierzbicki. *Structural Crashworthiness and Failure*. CRC Press, 1993. ISBN 9781851669691.

[2] a.G Mamalis, M. Robinson, D. Manolakos, G. Demosthenous, M. Ioannidis, and J. Carruthers. Crashworthy capability of composite material structures. *Composite Structures*, 37(2):109–134, 1997. ISSN 02638223. doi: 10.1016/S0263-8223(97)80005-0.

[3] CZone. Engenuity Ltd., West Sussex, UK, 2016, 2016.

[4] J. D. Reid. Crashworthiness of automotive steel midrails: Thickness and material sensitivity. *Thin-Walled Structures*, 26(2):83–103, 1996. ISSN 02638231. doi: 10.1016/0263-8231(96)00010-9.

[5] H. Yoshida, A. Uenishi, Y. Kuriyama, and M. Takahashi. Crashworthiness Improvement of The Side Crash By The Work Hardening Effect of Pre-Strained High Strength Steel. *SAE Technical Paper 2001-01-3112*, 2001. doi: 10.4271/2001-01-3112.

[6] D. Mohr and T. Wierzbicki. Crashworthiness of Thin Ultra-light Stainless Steel Sandwich Sheets: From the Design of Core Materials to Structural Applications. *SAE Technical Papers 2004-01-0886*, 2004. doi: 10.4271/2004-01-0886. URL `http://www.scopus.com/inward/record.url?eid=2-s2.0-84877231442{&}partnerID=tZOtx3y1`.

[7] S. Bogomolov, M. Spaniel, and V. Kulisek. Different approaches to simulation of composite tube crush under impact loading. In *VKMKP 2013 Conference*, pages 1–10, 2013.

[8] Abaqus. Dassault Systèmes, Vélizy-Villacoublay, France, 2016, 2016.

[9] LS-DYNA. LSTC,Livermore, CA, USA, 2016.

[10] F. Deleo and P. Feraboli. Crashworthiness Energy Absorption of Carbon Fiber Composites: Experiment and Simulation. *SPE Automotive Composites Conference*, (January):32, 2011. ISSN 00036900. URL `http://www.speautomotive.com/SPEA{_}CD/SPEA2011/pdf/VPT/VPT3.pdf`.

[11] S. H. Hesse, D. H. J. A. Lukaszewicz, and F. Duddeck. A method to reduce design complexity of automotive composite structures with respect to crashworthiness. *Composite Structures*, 129: 236–249, 2015. ISSN 02638223. doi: 10.1016/j.compstruct.2015.02.086. URL `http://dx.doi.org/10.1016/j.compstruct.2015.02.086`.

[12] D. Ramos and B. D. Melo. Composite structures impact simulation behavior. (November), 2014.

[13] Hypercrash. Altair, Troy, Michigan, USA, 2016.

[14] FSAE. FSAE Online. URL http://www.fsaeonline.com.

[15] J. Obradovic, S. Boria, and G. Belingardi. Lightweight design and crash analysis of composite frontal impact energy absorbing structures. *Composite Structures*, 94(2):423–430, 2012. ISSN 02638223. doi: 10.1016/j.compstruct.2011.08.005.

[16] S. Boria and G. Belingardi. Numerical investigation of energy absorbers in composite materials for automotive applications. *International Journal of Crashworthiness*, 17(4):345–356, 2012. ISSN 1358-8265. doi: 10.1080/13588265.2011.648516.

[17] R. D. Hussein, D. Ruan, G. Lu, and I. Sbarski. Axial crushing behaviour of honeycomb-filled square carbon fibre reinforced plastic (CFRP) tubes. *Composite Structures*, 140:166–179, 2016. ISSN 02638223. doi: 10.1016/j.compstruct.2015.12.064. URL http://dx.doi.org/10.1016/j.compstruct.2015.12.064.

[18] S. Heimbs and F. Strobl. Crash Simulation of an F1 Racing Car Front Impact Structure. *7th European LS-DYNA Conference*, (MAY):1–8, 2009. URL http://www.heimbs-online.de/Heimbs{_}2009{_}Formula1Crash.pdf.

[19] D. Kumar, S. Kumar, G. Singh, and N. Khanna. Drop Test Analysis of Impact Attenuator for Formula SAE Car. *International Journal of Scientific and Research Publications*, 2(10):5–8, 2012.

[20] R. Munusamy and D. C. Barton. Lightweight impact crash attenuators for a small Formula SAE race car. *International Journal of Crashworthiness*, 15(772815469):223–234, 2010. ISSN 1358-8265. doi: 10.1080/13588260903122680.

[21] E. M. Browne. Optimalisert karbonfiber krasjnese for høyytelses Formula Student racerbil. 2016.

[22] D. H.-J. Lukaszewicz. Automotive Composite Structures for Crashworthiness. In *Advanced Composite Materials for Automotive Applications*, pages 99–127. 2013. ISBN 9781118535288. doi: 10.1002/9781118535288.ch5. URL http://dx.doi.org/10.1002/9781118535288.ch5.

[23] H. Y. Ko, K. B. Shin, K. W. Jeon, and S. H. Cho. A study on the crashworthiness and rollover characteristics of low-floor bus made of sandwich composites. *Journal of Mechanical Science and Technology*, 23(10):2686–2693, 2009. ISSN 1738494X. doi: 10.1007/s12206-009-0731-7.

[24] J. Verbeke and R. Cools. The Newton-Raphson method. *International Journal of Mathematical Education in Science and Technology*, 26(2):177–193, 1995. ISSN 0020-739X. doi: 10.1080/0020739950260202.

[25] M. F. de Moura, A. B. de Morais, and A. G. de Magalhães. *Materiais Compósitos - Materiais, Fabrico e Comportamento Mecânico*. Publindústria, Edições Técnicas, second edition, 2011. ISBN 978-972-8953-00-3.

[26] B. H. Jiang and R. Q. Zhang. Strain rate-dependent Tsai-Hill strength criteria for a carbon fiber woven reinforced composite. *Baozha Yu Chongji/Explosion and Shock Waves*, 26(4):333–338, 2006. ISSN 10011455. URL http://www.scopus.com/inward/record.url?eid=2-s2.0-33749461894{&}partnerID=40{&}md5=76428042a7efb3519fab1a196928d758.

[27] M. Suhairil and H. Husain. Investigation of The Amount of Energy Absorption of Aluminium Tube : Inversion and Concertina Collapse Mode. *International Journal on Advanced Science Engineering Information Technology*, 2(3):69–73, 2012. ISSN 2088-5334.

[28] O. Hoffman. The Brittle Strength of Orthotropic Materials. *Journal of Composite Materials*, 1(2): 200–206, 1967. ISSN 0021-9983. doi: 10.1177/002199836700100210.

[29] S. W. Tsai and E. M. Wu. A General Theory of Strength for Anisotropic Materials. *Journal of Composite Materials*, 5(1):58–80, 1971. ISSN 0021-9983. doi: 10.1177/002199837100500106. URL http://jcm.sagepub.com/cgi/doi/10.1177/002199837100500106{%}5Cnhttp://jcm.sagepub.com/content/5/1/58.

[30] K. Miettinem. *Non Linear Multiobjective Optimization*. Kluwer Academic Publishers, New York, 1999.

[31] V. M. Franco Correia, J. Madeira, A. Araújo, and C. Mota Soares. Multiobjective design optimization of laminated composite plates with piezoelectric layers. *Composite Structures*, 169:10–20, 2016. ISSN 02638223. doi: 10.1016/j.compstruct.2016.09.052. URL http://dx.doi.org/10.1016/j.compstruct.2016.09.052.

[32] J. F. A. Madeira, A. L. Araújo, and C. M. M. Soares. Multiobjective optimization of constrained layer damping treatments in composite plate structures. *Mechanics of Advanced Materials and Structures*, 6494(February):0–0, 2016. ISSN 1537-6494. doi: 10.1080/15376494.2016.1190427. URL https://www.tandfonline.com/doi/full/10.1080/15376494.2016.1190427.

[33] V. M. Franco Correia, J. Aguilar Madeira, A. L. Araújo, and C. M. Mota Soares. Multiobjective optimization of ceramic-metal functionally graded plates using a higher order model. *Composite Structures*, 2017. ISSN 02638223. doi: 10.1016/j.compstruct.2017.02.013. URL http://linkinghub.elsevier.com/retrieve/pii/S0263822317303367.

[34] a. L. Custódio, J. F. a. Madeira, a. I. F. Vaz, and L. N. Vicente. Direct Multisearch for Multiobjective Optimization. *SIAM Journal on Optimization*, 21:1109–1140, 2011. ISSN 1052-6234. doi: 10.1137/10079731X.

[35] FSAE. Formula Student competition rules. http://www.fsaeonline.com, 2016. URL http://www.fsaeonline.com/page.aspx?pageid=e179e647-cb8c-4ab0-860c-ec69aae080a3.

[36] B. &. Kjaer. Accelerometers and charge amplifiers, 2017. URL https://www.bksv.com/en.

[37] N. Instruments. PXI equipment, 2017. URL http://www.ni.com/en-gb/shop.html.

[38] Solidworks. Dassault Systèmes, Vélizy-Villacoublay, France, 2016, 2016.

[39] Hypermesh. Altair,Troy, Michigan, USA, 2016.

[40] Radioss. Altair,Troy, Michigan, USA, 2016.

[41] R. Ramsdale. Engineers Handbook, 2017. URL http://www.engineershandbook.com/Tables/frictioncoefficients.htm.

[42] Tracker. Douglas Brown, http://physlets.org/tracker/, 2016.

[43] A. G. Mamalis, D. E. Manolakos, G. A. Demosthenous, and M. B. Ioannidis. The static and dynamic axial collapse of fibreglass composite automotive frame rails. *Composite Structures*, 34(1):77–90, 1996. ISSN 02638223. doi: 10.1016/0263-8223(95)00134-4.

[44] 3DCore. http://www.3d-core.com,Oststrasse, Herford, Germany, 2016.

[45] Matlab. Mathworks,Natick, Massachusetts, USA, 2016.

[46] E. Music and A. Widroth. Modelling of Spread Tow Carbon Fabric Composites for Advanced Lightweight Products. page 70, 2013. URL http://publications.lib.chalmers.se/records/fulltext/185791/185791.pdf.